To G. Mitchell:
Prof. Gary. Thank
for everything
Hanan

Octupole Correlations In Heavy Nuclei: Vibrations in Superdeformed ^{190}Hg and Search for the Double-Octupole Multiplet in ^{208}Pb

by

Hanan Amro

A dissertation submitted to the graduate Faculty of
North Carolina State University
in Partial Fulfillment of the
requirements for the Degree of
Doctor of Philosophy

Department of Physics

Raleigh
1999

APPROVED BY:

_____ _____

_____ _____

_____

Chair of Advisory Committee

ABSTRACT

Hanan Amro. Octupole Correlations In Heavy Nuclei: Vibrations in Superdeformed ^{190}Hg and Search for the Double-Octupole Multiplet in ^{208}Pb. (Under the direction of Dr. E. F. Moore and Dr. R.V.F. Janssens)

The work described in this thesis addresses two different manifestations of the octupole degree of freedom in nuclei: the coupling of rotation and vibration at very large deformation and the search for $3^- \otimes 3^-$ double-phonon states. A series of measurements using the world's most sensitive γ-ray spectrometer, i.e. the Gammasphere array, were performed to address these two issues.

The Doppler-shift attenuation method was used to measure lifetimes of superdeformed (SD) states in both the yrast and the first excited SD band of ^{190}Hg. Intrinsic quadrupole moments Q_0 were extracted for each SD band. More importantly, the dipole transition rates were determined for the inter-band transitions which connect the excited SD band to the yrast states in the second minimum. It was shown for the first time that the lowest excitation in the SD well corresponds to a collective one-phonon octupole vibration rather than to a quasiparticle excitation as had been previously conjectured.

A series of Coulomb excitation measurements was performed to search for the double-phonon octupole vibrational multiplet in ^{208}Pb. None of the anticipated multiplet members was found and stringent upper limits were derived for the population of such states. These limits are so low that, on the one hand, the suitability of a simple vibrational picture can be ruled out, and on the other, strong evidence is now available favoring an interpretation in terms of a sizable fragmentation of the collective $E3$ strength.

Dedication

To my little angel

Dania

Biography

Hanan Amro

Graduate Studies: Argonne National Laboratory, Argonne, IL
North Carolina State University, Raleigh, NC

Conferred Degree: Ph.D., Nuclear Physics, (Summer 1999)

Honors: ASAI fellowship (1992-1995)
The Outstanding Teaching Assistant Award, North Carolina State University (1994)

Experience: Research Assistant: Laboratory Graduate Assistant at ANL (1995-present)

- Thesis research focusing on octupole correlations in heavy (superdeformed ^{190}Hg, and doubly-magic ^{208}Pb) nuclei.
- Active collaborator in experiments carried out using Gammasphere at LBNL and the Argonne-Notre Dame BGO array at ANL.
- Involved in the reliable operation of the BGO array.
- Involved in the assembly and operation of the AYE-ball array at ANL.

Teaching Assistant: North Carolina State University (1992-1994)

- Introductory physics laboratory course (1992-1994)

Selected Publications:

Lifetime Measurements and dipole Transition Rates for Superdeformed states in ^{190}Hg.

H. Amro, E. F. Moore, R. V. F. Janssens, G. Hackman, S. M. Fischer, I. Ahmad, M. P. Carpenter, B. Crowell, T. L. Khoo, T. Lauritsen, D. Nisius, J. Timar, and A. N. Wilson, Phys. Lett. **B 413**, 17 (1997)

Octupole Correlations in ^{190}Hg.

H. Amro, R. V. F. Janssens, E. F. Moore, G. Hackman, S. M. Fischer, I. Ahmad, M. P. Carpenter, B. Crowell, T. L. Khoo, T. Lauritsen, D. Nisius, J. Timar, A. N. Wilson

Proceedings of the International Conference "The Nucleus: New Physics for the New Millennium", National Accelerator Center, January 18-22, Faure, South Africa, (1999)

Acknowledgments

Many people have contributed in many ways to the work described in this thesis, I thank them all.

In particular, I would like to start by expressing my deep gratitude to my supervisors, Dr. Robert V. F. Janssens and Dr. E. Frank Moore. To Robert: you showed me at every turn that physics can be exciting! Your enthusiasm and knowledge is one I aspire to achieve. It is your patience (which I tested at every opportunity) with my inability to write that taught me in the end a bit about scientific writing.

To Frank: your enthusiasm and support throughout my graduate years made it real fun. I am, indeed, grateful for the valuable discussions and the computer codes that you provided to carry out the data analysis described in this thesis.

Big thanks to Dr. Mike Carpenter and Dr. Greg Hackman to whom I am deeply indebted for their insights and their help. I thank both of you for providing many of the analysis codes needed to carry out this work. Many thanks are due to Dr. Torben Lauritsen especially for his patience with my incapacity to communicate with computers. To Prof. Steve Yates from the University of Kentucky: thanks for your insightful advice, help and support. Thanks to Dr. Kai Vetter from LBNL for the many helpful discussions on the "lead stuff" and for the many contributions to this thesis. To Dr. Dave Nisius, my office mate in the early years, I want to say that I truly appreciate the help and support given to me throughout these years.

I would like to express my gratitude to the rest of my collaborators who took part in running all the experiments described in this thesis: T. L. Khoo, W. Henning, S. Fischer, C.J. Lister, I. Ahmad, B. Crowell, J. Timar, A. N. Wilson, A. O. Macchiavelli, D.J.

Blumenthal, and S.I. Sanders.

To my friends, thanks for providing me with escape routes. I am indeed grateful for your constant love and support.

Finally, I would like to express my gratitude to the Physics division at ANL for the financial support it has provided me throughout the entire course of this work and for the pleasant working enviroment.

Contents

List of Tables

List of Figures

Introduction

Octupole correlations play an important, yet often subtle, role in the structure of many nuclei. These correlations often manifest themselves through the presence at low excitation energy of states with odd spin and negative parity. The interest in octupole correlations comes, at least in part, from the fact that they are associated with the breaking of a symmetry of the nuclear Hamiltonian. In nuclei with a quadrupole deformed, axially symmetric shape, band structures of states with positive parity are the norm because such shapes are symmetric under space inversion. The same property applies to spherical nuclei in which quadrupole vibrations occur. However, as soon as octupole degrees of freedom are involved, the potential becomes reflection asymmetric. This is easily visible for the most common octupole shape, the "pear-like" shape, where the nuclear potentials prior and after a rotation by 180° can be distinguished from one another.

The shell structure of the nucleus is responsible for the presence of octupole correlations as it is for many other nuclear phenomena. The correlations find their origin in the long-range octupole-octupole interaction between nucleons. Microscopically, they can be described as the result of the coupling between orbitals with $\Delta j = \Delta l = 3$. Octupole effects are expected to be strong when both protons and neutrons occupy orbitals fulfilling this condition, provided that these orbitals are located close to the Fermi surface. Thus, nuclei with specific proton and neutron numbers will be particularly susceptible to octupole effects. The numbers of interest are: 34 (coupling between the $g_{9/2}$ and $p_{3/2}$ orbitals), 56 (overlap between the $h_{11/2}$ and $d_{5/2}$ states), 88 (the $i_{13/2}$ and $f_{7/2}$ orbitals are involved), and 134 (coupling of the $j_{15/2}$ and $g_{9/2}$ levels). It is noteworthy that these numbers are close to the magic numbers associated with closed shells.

It is important to realize that octupole correlations remain relatively small in magnitude. For example, in deformed nuclei, the gain in binding energy coming from quadrupole degrees of freedom is often of the order of 10 MeV or more while the additional binding due to octupole correlations is at most 1-2 MeV. Similarly, in spherical nuclei, states associated with octupole vibrations are often visible in doubly-magic nuclei because the associated excitation energies are smaller than the typical pairing gaps, i.e. than the energies required for particle-hole excitations. It should then come as no surprise that these correlations are often treated as a perturbation to the nuclear mean field.

The work presented in this thesis addresses two of the most pressing issues in contemporary nuclear structure physics associated with octupole correlations. With the discovery of the phenomenon of superdeformation in the mid-eighties, the prediction was verified that shell effects in nuclei can be sufficiently strong to generate a deep second minimum in the nuclear potential at very large quadrupole deformation (ellipsoidal shape with 2:1 axis ratio). It was soon realized that some of the orbitals located in the vicinity of the Fermi surface in the superdeformed well are precisely those involved in octupole coupling. Hence, the issue of the stiffness of the superdeformed potential against octupole vibrations needed investigation. The problem is far from trivial, be it only because the pairing properties at large deformation were calculated and later found to be quite different from those measured at normal deformation. Furthermore, the stress induced by rotation is very large for superdeformed states, i.e. the associated rotational frequencies are often among the largest ones known, and the impact of this feature on the spectrum of possible excitations needed to be quantified. The role of octupole degrees of freedom at large deformation is investigated in the present work in the case of the superdeformed ^{190}Hg nucleus.

The second issue studied in the present work can be viewed as a re-visit of a problem that has been lacking a satisfactory experimental answer for most of the second half of the century: the validity and the range of applicability of the octupole vibrational picture in the doubly-magic ^{208}Pb nucleus. The first excited state in ^{208}Pb is a 3^- level. All its properties, i.e. the quantum numbers, the excitation energy, the $B(E3)$ transition rate, etc.. agree with an interpretation of this state in terms of a one-phonon octupole vibra-

tion. Yet, despite years of effort, no conclusive evidence has thus far been found for the existence of levels to be associated with the double-octupole phonon, i.e. for levels corresponding to the $3^- \otimes 3^-$ coupling. The discovery of these states would not only validate the vibrational picture, but would also address related issues such as the possible presence and relative importance of anharmonicities or the degree of mixing of the octupole states with other levels. Such a mixing should be expected since the relevant excitation energies lie well above the pairing gap. This thesis describes a new attempt at the identification of the double-octupole phonon multiplet by taking advantage of the world's most sensitive gamma-ray spectrometer, i.e. the Gammasphere array.

For clarity and easiness of reading, this thesis is divided in three distinct parts. In the first of these, the theoretical concepts relevant to the problems under discussion are being briefly described. They provide the basis for understanding and interpreting the experimental results. In addition, a chapter is devoted to the various experimental techniques and analysis methods used during the course of this project. The second part of the thesis discusses the studies of octupole vibrations in the superdeformed well of ^{190}Hg. The importance of the problem is discussed in an introduction, which is followed by a presentation of the experimental approach, a discussion of the analysis, and an in-depth review of the results. This part concludes with the interpretation chapter where the data are compared with the available calculations. Part three of the thesis discusses the search for the double-octupole phonon states in ^{208}Pb. The presentation follows the same general outline described above for part two. Finally, this thesis ends with a brief summary of the most important results and a short presentation of possible follow-up measurements.

Part I

General Considerations

Chapter 1

Theoretical Concepts

In this thesis the main focus is on a study of octupole correlations in heavy nuclei. Collective excitations in the spherically symmetric nucleus ^{208}Pb and in the deformed nucleus ^{190}Hg will be examined. In the following sections a brief overview of the basic theoretical terms and concepts which provide the basis for the interpretation of the experimental results will be presented.

1.1 The Nuclear Shell Model

The presence of shells inside the nucleus is evident from a number of experimental facts. One of the most obvious indications is obtained from the comparison with the analogous picture of electrons moving in the atom. The neutron (proton) separation energy, like the atomic ionization energy, increases gradually with N or Z except for a few sharp jumps that occur at the same proton and neutron numbers, the so-called "magic numbers"; i.e. Z and/or N=2, 8, 20, 28, 50, 82, 126. The sharp discontinuities in the separation energy correspond to the filling of major shells. Another indicator is obtained by investigating the variations of the excitation energy of the first excited state with Z and N in all even-even nuclei: the extra stability at 8, 20, 28, 50, 82, and 126 is evident from the high excitation energy of the first excited state of the nuclei of interest. The Nuclear Shell Model [May49, Hax49] was proposed over fifty years ago and has been quite

successful in describing the nuclear structure properties of nuclei with very few nucleons outside closed shells. This model does not, however, describe with equal success nuclei further away from closed shells. The nucleons in this model are assumed to be independent particles moving in an average potential which they themselves have generated. The three dimensional harmonic oscillator potential, equation 1.1, with an added spin-orbit (**l.s**) and a centrifugal ($\mathbf{l^2}$) terms, is employed in order to reproduce the observed magic numbers.

$$V(r) = \frac{1}{2}m(\omega r)^2 + f(r)\mathbf{l^2} + \alpha(\mathrm{r})\ \mathbf{l.s} \tag{1.1}$$

where l is the orbital angular momentum and **s** is its intrinsic spin. The inclusion of the term **l.s** gives a splitting of the otherwise degenerate levels with j=l$\pm\frac{1}{2}$.

The Wood-Saxon potential in equation 1.2, with a strong spin-orbit term, is a more realistic central potential when compared to the harmonic oscillator potential (since it has a finite well-depth) with which all the magic numbers are reproduced accurately.

$$V(r) = -V_0[1 + \exp^{(\frac{r-R_0}{a})}]^{-1} + \alpha(r)\ \mathbf{l.s} \tag{1.2}$$

with R_0=$r_0A^{1/3}$, $V_0 \approx 50$ MeV, a $\approx$ 0.5 fm and $r_0 \approx 1.2$ fm. The inclusion of the spin-orbit coupling will also allow the highest j orbital, for shells with $N > 3$, to be brought down in energy to the next lower shell. This orbital then becomes a so-called intruder orbital. For the potential described in equation 1.2, the total angular momentum, **j** =**l** +**s** , and the parity, $\pi = (-1)^l$, are the only good quantum numbers [May55].

1.2 The Deformed Shell Model

The nuclear potentials described above assume spherical symmetry in the nucleus. However, since nuclei can be deformed (as is discussed below) modifications to these potentials are necessary for the description of deformed nuclei. In the following sections, the elements of the deformed shell model are described.

1.2.1 Nuclear Shapes

Many of the nuclear properties involve the motion of many nucleons "collectively". The allowed modes of collective motion depend on the nuclear shape which varies depending on the number of protons and neutrons involved. In general, nuclei with a magic number of neutrons and a magic number of protons, the so-called doubly-magic nuclei such as ^{208}Pb for example, are very stable and are spherical in their ground state. When a sufficient number of nucleons is added beyond the magic numbers, the long-range effective forces between valence nucleons distort the shape from spherical symmetry and the nucleus is deformed.

Spherical nuclei do not have rotational degrees of freedom and, as a result, vibrational motion stands out more clearly. On the other hand, deformed nuclei do have rotational degrees of freedom, therefore, rotational motion is dominant. Finally, vibrational motion built upon deformed shapes is also a commonly observed feature in nuclei.

It is appropriate to describe these modes of collective motion using a Hamiltonian expressed in terms of the macroscopic coordinates of the system such as mass, radius, and volume. Departures from spherical shapes (due to deformation or to small oscillations in the shape of spherical nuclei) may be described in terms of a set of shape parameters $\alpha_{\lambda\mu}$ defined in the following way:

$$R(\theta,\phi) = R_0\left(1+\alpha_{00}+\sum_{\lambda=1}^{\infty}\sum_{\mu=-\lambda}^{\lambda}\alpha_{\lambda\mu}Y_{\lambda\mu}(\theta,\phi)\right) \tag{1.3}$$

where $R(\theta,\phi)$ is the distance from the center of the nucleus to the surface at angles (θ,ϕ), R_0 is the radius of an equivalent sphere, and α_{00} is chosen to insure that the nuclear volume is constant (i.e. no density change). Each mode of order λ has $(2\lambda+1)$ parameters corresponding to $\mu = -\lambda, -\lambda+1, ..., \lambda$. However, because of rotational invariance, these parameters are not independent of each other.

Terms associated with λ=1 describe a shift in the position of the center of mass. In the case of collective rotation, these terms are usually fixed by requiring that the coordinate origin coincides with the center of mass. In the case of collective vibrations, the λ=1 mode corresponds to a dipole oscillation of protons and neutrons in opposite direction.

Giant dipole resonances observed in many nuclei are a good example of this mode. The λ=2 mode describes quadrupole deformation. In such a case, the nuclear shapes are either spheroidal, having two equal semi-major axes (oblate deformed nuclei), or spheroid having two equal semi-minor axes (prolate deformed nuclei). A quadrupole vibration, then, corresponds to the situation where the nucleus changes its shape continuously from spherical to prolate, back to spherical and then to oblate, and then back to spherical. The λ=3 term introduces octupole deformation in which the nucleus has a pear shape, which is axially symmetric but reflection asymmetric. A similar situation in which the nucleus changes its shape continuously from spherical to a pear shape, and then back to spherical corresponds to octupole vibration.

1.2.2 The Deformed Mean Field Potentials

Once again, the nuclear potentials presented earlier can describe spherical and near spherical nuclei successfully. Unfortunately, they can not successfully describe deformed nuclei. Therefore, the deformed shell model was introduced which takes into consideration how a deformed shape (and thus the average field) influences the nuclear single-particle motion. In this model, it is possible to evaluate the total energy of a static, deformed nucleus (i.e. the single-particle level spectrum as a function of deformation). The minimization of this total energy expression gives rise to stable, deformed minima. A deformed mean field Wood-Saxon potential is employed in order to describe deformed nuclei. This potential can be expressed as:

$$V_{WS} = V_c(\mathbf{r},\beta) + \mathrm{V_{so}}(\mathbf{r},\beta) + \frac{1}{2}(1+\tau_3)\mathrm{V_{coul}}(\mathbf{r},\beta), \tag{1.4}$$

where V_c is the central potential which can be expressed as:

$$V_c(\mathbf{r},\beta) = \frac{\mathrm{V_0}}{1+\mathrm{e}^{\left(\frac{\mathrm{r-R}(\theta)}{\mathrm{a}}\right)}} \tag{1.5}$$

where the distance from the point r to the nuclear surface $(r - R(\theta))$ is defined as positive outside the nucleus and negative inside, τ_3 is the isospin quantum number. V_0 is the depth of the potential at $\mathrm{r} = 0$ and a is the diffuseness parameter which describes the decrease

in the strength of the nuclear potential as one moves outward in the radial direction. V_{so} is the spin-orbit term which has been shown to be of the form $\mathbf{s.p} \times \nabla \mathbf{V}$ [Boh69], V_{coul} is the known Coulomb potential, and $R_0 = r_0 A^{1/3}$. Such a deformed potential can be employed to solve the time-independent Schrödinger equation and, as a result, the single-particle energies (i.e. the so-called Nilsson diagram) can be determined as a function of the quadrupole deformation parameter β_2. At zero deformation, i.e. spherical nuclei, the shell gaps of the spherical Shell Model are reproduced at the well known magic numbers. At other deformations, corresponding to prolate and oblate shapes, new energy gaps occur. This indicates that nuclei with proton and/or neutron numbers corresponding to these new magic numbers should have stable non-spherical shapes. Obviously, in a deformed potential, the spherical symmetry of the nucleus is lost and, thus, the total angular momentum J is no longer a good quantum number. The energy levels can be labeled by the so-called Nilsson quantum numbers $[\mathrm{Nn}_z\Lambda]\Omega^\pi$, where N is the principle quantum number, n_z is the number of nodes in the wavefunction along the symmetry axis, Λ is the projection of the orbital angular momentum along the symmetry axis, $\Omega = \lambda \pm \frac{1}{2}$ (The introduction of deformation destroys the degeneracy in Ω, i.e. there are always two orbitals with the same Ω because of time-reversal symmetry) is the projection of the single particle angular momentum along the symmetry axis, and $\pi = (-1)^N$ is the parity. Except for π and Ω, these quantum numbers are not real quantum numbers and one has to keep in mind that they are used merely as labels for the single-particle energy levels. They can only be good in the limit of infinite deformation (i.e. asymptotic quantum numbers) [Boh69].

1.2.3 Electric Quadrupole Moments

The nuclear quadrupole moment can be defined in terms of the charge density of the nucleus, ρ_{ch}, as:

$$eQ(\mathbf{r}) = \int \rho_{\mathbf{ch}}(\mathbf{r})\mathrm{r}^2(3\cos^2\theta - 1)\mathrm{dV} \tag{1.6}$$

where $\mathbf{r}$ is the radius and θ is the angle it subtends. The nuclear quadrupole moment tells

us whether nuclei are spherical (for which Q=0 since the integral over the volume, as is described in equation 1.6, will vanish) or non spherical. If Q >0, the nucleus is prolate deformed while a nucleus is oblate deformed if it has a negative quadrupole moment. The intrinsic quadrupole moment Q_o (since it is related to the shape of the intrinsic state) for a non-rotating axially-deformed nucleus with only quadrupole deformation is defined in terms of the deformation of the nucleus as follows:

$$eQ_o = \frac{3}{\sqrt{5\pi}} ZeR_o^2\beta_2. \tag{1.7}$$

This relationship becomes much more complex in the superdeformed case discussed in this thesis as higher order terms of β_2 become important. The correct expression can be found in reference [Naz89]. In principle, direct measurements of quadrupole moments are possible only for the ground state of nuclei. For excited states, the quadrupole moment can sometimes be deduced indirectly through reactions such as Coulomb excitation. Due to the fact that it is not trivial to experimentally examine the charge distribution of a deformed nucleus and deduce its quadrupole moment, in the work described in the present thesis, a model-dependent electric quadrupole moment for a deformed nucleus is extracted from lifetime measurements of states in a rotational cascade.

1.3 Collective Rotation and the Cranked Shell Model

1.3.1 Nuclear Rotation

In the case of collective rotation of a strongly quadrupole-deformed nucleus, the λ >2 terms in equation 1.3 are often neglected. In this case the nuclear shape can be described in the body-fixed coordinate system with the three axes defined by the principle axes of the nuclear mass distribution. Thus, for a pure quadrupole deformation, where only Y_{00} and Y_{20} harmonics are involved and where $\alpha_{22} = \alpha_{2-2}$, equation 1.3 reduces to:

$$R(\theta) = R_0(1 + \alpha_{00}Y_{00} + \alpha_{20}Y_{20}) \tag{1.8}$$

where α_{20} can be defined as:

$$\alpha_{20} = \beta_2 = \frac{4}{3}\sqrt{\frac{\pi}{5}} \quad \frac{\Delta R}{R_0} \tag{1.9}$$

where ΔR is the difference between the major and minor axes of the ellipsoid. One still has to take into account the possibility of non axially-symmetric (i.e. triaxial) shapes. According to the Lund convention, as is illustrated in Figure 1.1, triaxial shapes occur whenever the triaxiality parameter γ is not a multiple of 60°. In this convention, α_{20} and α_{22} can be expressed as,

$$\alpha_{20} = \beta_2 cos\gamma \tag{1.10}$$

$$\alpha_{22} = \beta_2 sin\gamma \tag{1.11}$$

with β_2 representing the degree of quadrupole deformation. In the Lund convention, $\gamma = 0°$ and $\gamma = -60°$ correspond to a prolate and a oblate shape, respectively, undergoing a collective rotation about an axis perpendicular to the symmetry axis. Intermediate values of γ describe various degrees of triaxiality. So-called non-collective rotations about the symmetry axis are associated with $\gamma = 60°$ and $\gamma = -120°$ for oblate and prolate shapes, respectively. In the case of non-collective rotation, the nuclear angular momentum is built by aligning individual single-particle angular momenta along the symmetry axis.

1.3.2 Rotational Bands

Collective rotation of a nucleus results in a sequence of states (generally called bands) built upon one of the following intrinsic excitations; (i) the ground state configuration, (ii) various collective modes of vibrational excitation, (iii) single-particle or quasi-particle excitations. In an axially symmetric system, the rotational energy is given by:

$$E_{rot} = \frac{\hbar^2}{2\Im} I(I+1), \tag{1.12}$$

where $\Im$ is the moment of inertia. The total nuclear angular momentum of the nucleus $\mathbf{I}$ is the sum of the angular momentum associated with the collective rotation $\mathbf{R}$ and the single

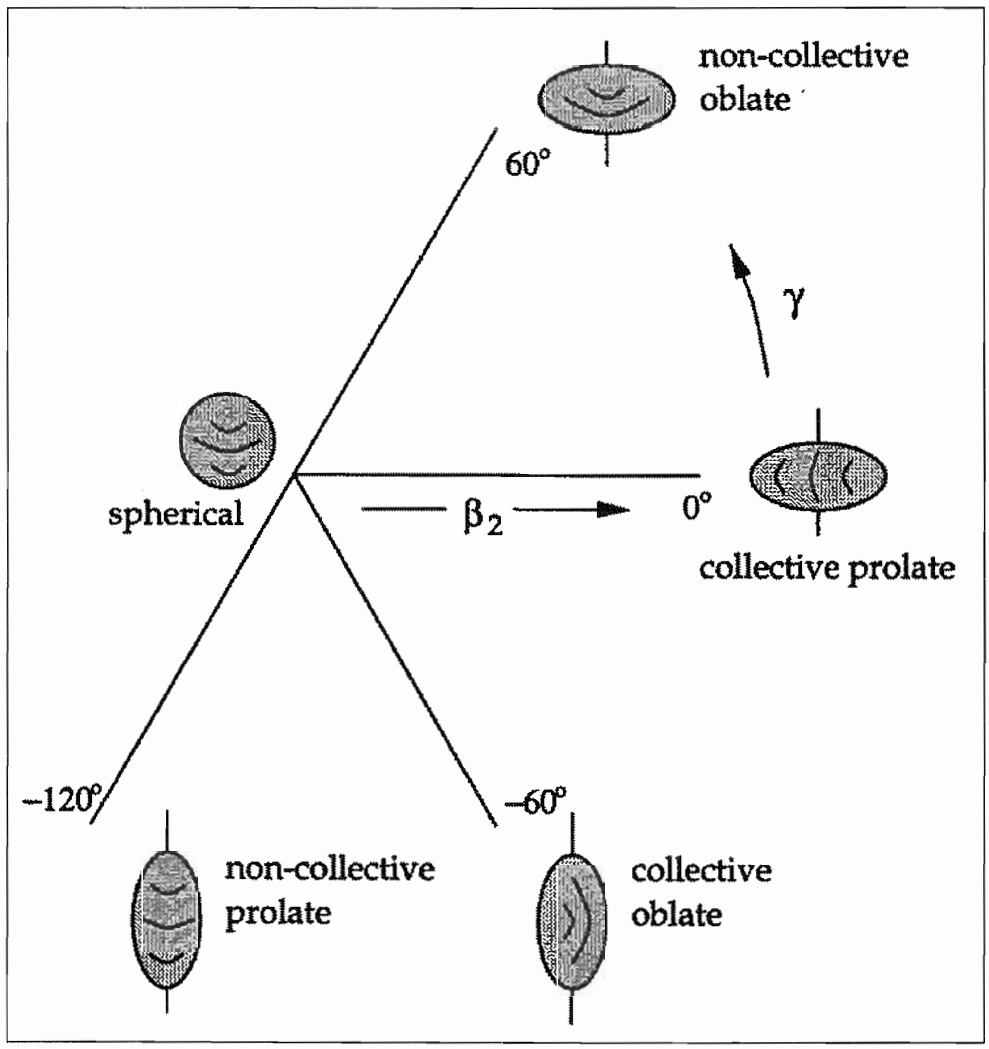

Figure 1.1 Nuclear shapes in the Lund convention.

particle angular momentum, $\mathbf{j}$. The levels in a rotational band are connected by highly collective quadrupole transitions with energies E_γ, $E_\gamma = \Delta E_{rot}$. The coor5inate system and the relevant quantities to describe nuclear rotation (as is described in the present work) are illustrated in Figure 1.2. In this body-fixed coor5inate system, the z-axis is chosen to lie along the symmetry axis of the nucleus while the x-axis is the collective rotation axis.

The rotational frequency of the collectively rotating nucleus is defined as:

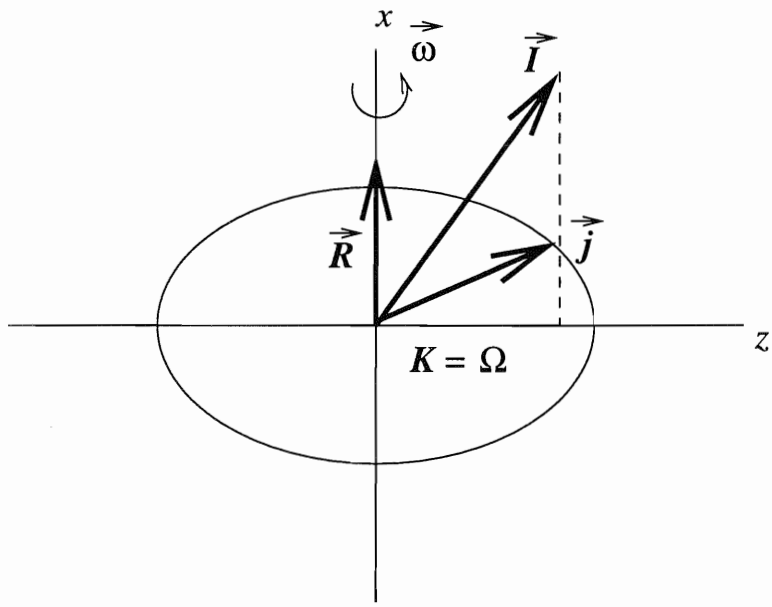

Figure 1.2 The angular momentum components for a nucleus rotating about an axis perpendicular to its symmetry axis.

$$\omega = \frac{dE_{rot}}{dI} \approx \frac{\Delta E_{rot}}{\Delta I} = \frac{E_\gamma}{2\hbar}. \tag{1.13}$$

This approximation acknowledges the fact that the spin is quantized. The "kinematic moment of inertia", $J^{(1)}$ is defined as:

$$J^{(1)} = I(\frac{dE_{rot}}{dI})^{-1} \approx I(\frac{\Delta E_{rot}}{\Delta I})^{-1} = \frac{2I\hbar}{E_\gamma}. \tag{1.14}$$

Due to the fact that in most cases the spins of the superdeformed states are not known, the $J^{(2)}$ inertia parameter (which is usually called "the dynamic moment of inertia") is introduced as a characteristic feature of superdeformed bands and is defined as:

$$J^{(2)} = (\frac{d^2E_{rot}}{dI^2})^{-1} \approx \frac{4\hbar^2}{\Delta E_\gamma} \tag{1.15}$$

The $J^{(2)}$ moment represents the nucleus response to a force and is independent of the spins of the rotational band.

1.3.3 The Cranked Shell Model

Microscopically, the rotation alters the energy distribution of the single particle levels, in particular those with large angular momentum components along the symmetry axis (the so-called high-j states). For a particular deformation, collective rotation along with the shell effects can give rise to gaps in the single particle spectrum which do not exist in the ground state. Therefore, as the nucleus rotates, new magic numbers are often generated. To study the behavior of the rotating nucleus (particularly at high spins), the Cranked Shell Model (CSM) is introduced. The CSM provides a fully microscopic description of nuclear rotation; it handles collective and single-particle excitations on an equal footing and it extends even to very high-spin states. In this model, the nucleons can be viewed as independent particles moving in an average potential which is rotating about an axis perpendicular to the symmetry axis with a constant rotational frequency ω. The so-called total cranking Hamiltonian, H^{ω}, of such a system in the rotational frame of reference is written as:

$$H^{\omega} = H^{lab} - \omega J_x \tag{1.16}$$

where H^{lab} is the total cranking Hamiltonian in the lab frame of reference, and J_x is the sum over all nucleons of the angular momentum j_x due to the rotation about the x-axis (the z-axis is defined as the symmetry axis). The rotating operator can be written in terms of j_x as:

$$\Re(\omega t) = e^{-i\omega t j_x/\hbar} \tag{1.17}$$

The single-particle wavefunction Ψ and single-particle Hamiltonian h can be transformed into the rotating coordinate system by the rotating operator (given in equation 1.17) as follows:

$$\Psi = \Re\Psi' \tag{1.18}$$

and

$$h' = \Re h \Re^{-1} \tag{1.19}$$

respectively. By substituting equations 1.18 and 1.19 into the time-dependent Schrödinger equation one obtains the following for the single-particle cranking Hamiltonian or Routhian h^{ω}:

$$i\hbar \frac{\partial}{\partial t} \Psi' = (h' - \omega j_x)\Psi' = h^{\omega}\Psi'. \tag{1.20}$$

The Schrödinger equation (equation 1.20) can be understood as the equation of motion in the rotating frame of reference and the solution to the eigenvalue problem

$$h^{\omega}\Psi' = \epsilon'\Psi' \tag{1.21}$$

yields the single-particle energy in the rotating frame (i.e $\epsilon' = \epsilon_{s.p.} - \omega j_x$). The component of the single particle angular momentum along the rotation axis is called the alignment and is the expectation value of j_x. The alignment can also be determined from the slope of the Routhian (i.e. $j_x = -\frac{d\epsilon'}{d\omega}$). Summing h^{ω} over all independent particles yields the total cranking Hamiltonian H^{ω}. Similarly, the addition of the single particle energies and of the individual alignments of all the independent particles yields the total Routhian E' and total alignment J_x, respectively.

The drawback of the CSM is that in the rotating frame time-reversal symmetry is lost (the angular momentum is not conserved), therefore, the only good quantum numbers remaining are the parity π and the signature α. The signature of a level (i.e. its invariance with respect to rotation of a 180° perpendicular to the symmetry axis of an axially symmetric potential) is introduced to distinguish levels whose two-fold degeneracy with respect to Ω has been broken by the rotation of the nuclear system. The energy levels calculated by CSM are labeled by their signature and parity quantum numbers. In addition, the Nilsson quantum numbers can be used in labeling these single-particle orbitals but only at $\omega = 0$.

1.4 The Strutinsky Method and the Nuclear Shapes

Up till now, it was not possible to produce the correct total ground-state energy with the shell models described earlier due to two factors. First, residual interactions are not treated well in these models. Second, the total ground-state energy is a bulk property and even a small shift in the single-particle energies can give rise to large errors in the binding energy. The Strutinsky total energy calculations are introduced in order to study ground-state properties (i.e. binding energy, deformation at equilibrium shape) in many regions of the nuclear chart. In this method, a shell correction δE_{shell} is added to the liquid-drop model (LDM) energy and the total energy can then be written as:

$$E_{total} = E_{liquid\ drop} + \delta E_{shell} \tag{1.22}$$

where the δE_{shell} term includes the shell correction terms for both the protons and neutrons. In the liquid drop model, the total energy of a rotating nucleus is the sum of Coulomb, surface and rotational energies (i.e. $E_{liquid\ drop} = E_{Coul} + E_{surface} + E_{rot}$). These three terms are all a function of deformation. Clearly, the surface energy term favors compact shapes (spherical shapes) in order to minimize surface area, however, the rotational energy term will lead to the development of deformed shapes and the Coulomb force (being a repulsive force) will enhance this deformation once it is acquired. The introduction of the shell corrections improves the predictions for the nuclear shape. The total energy as expressed in equation 1.22 can be calculated as a function of deformation for a particular nucleus to determine the most energetically efficient deformation available. A similar type of calculation can be performed in the rotating frame. In such calculations, the level energies are replaced by the Routhians (the energy eigen-states in the rotating frame) and the density function is replaced by a spin density function. The results of such calculations are called Total Routhian Surfaces (TRS) [Dud87, Naz87].

1.5 Nuclear Pairing Correlations

Due to the fact that the nucleon-nucleon force is short ranged and strongly attractive, some residual two-body interactions are expected in addition to the interactions with the mean field generated by all other nucleons in the nucleus. Residual interactions can have a major impact on the ordering and spacing of the single-particle energy levels of the deformed nucleus in a similar way that they impact the energy levels in the spherical nuclei. The presence of a residual pairing force is suggested by several experimental results such as:(i) the fact that the binding energy of an odd-even nucleus is found to be smaller than the average value of the binding energies of the two neighboring even-even nuclei, and (ii) the fact that the even-even nuclei always have 0^+ spin and parity in their ground state. The short-range attractive force between nucleons in the nucleus favors maximum overlap between the nucleonic wave functions. On the other hand, the Pauli exclusion principle prohibits identical wavefunctions. Therefore, the greatest overlap between the wavefunctions, and thus the minimum energy, occurs when the nucleons arrange themselves into pairs in time-reversed orbitals.

The pairing gap Δ is related to the energy difference between the ground-state and the first excited state. Due to the fact that the first excited state in even-even nuclei must be constructed of at least two quasiparticles (i.e. a mixture of both particle and hole), this difference is at least 2Δ.

Octupole correlations as well as the presence of rotation impact pairing correlations. In the presence of rotation, one expects the pairing correlations to become reduced, due to the Coriolis force. Microscopic calculations [Mey95] show that octupole deformation reduces pairing correlations because the level densities for the octupole deformed shapes are lower than those of reflection-symmetric shapes.

1.6 Shape Vibrations

A commonly observed type of vibration (that is of interest in the work described in this thesis) is an oscillation in the shape of the nucleus. When a spherical nucleus absorbs

small amounts of energy (too small to change its density), it starts to vibrate. These vibrations simply involve a change in the shape of the nucleus, as is described below:

$$R(\theta,\phi) = R_0\left(1+\alpha_{00}+\sum_{\lambda=1}^{\infty}\sum_{\mu=-\lambda}^{\lambda}\alpha_{\lambda\mu}Y_{\lambda\mu}(\theta,\phi)\right) \tag{1.23}$$

For small amplitude vibrations, the Hamiltonian for vibrational excitation of order λ may be written in the form:

$$H_\lambda = \frac{1}{2}C_\lambda\sum_\mu \mid \alpha_{\lambda\mu} \mid^2 + \frac{1}{2}D_\lambda\sum_\mu\left|\frac{d\alpha_{\lambda\mu}}{dt}\right|^2 \tag{1.24}$$

with,

$$D_\lambda = \frac{\rho R_0^5}{\lambda} \tag{1.25}$$

and

$$C_\lambda = \frac{1}{4\pi}(\lambda-1)(\lambda+2)\alpha_2 A^{2/3} - \frac{5}{2\pi}\frac{\lambda-1}{2\lambda+1}\alpha_3\frac{Z(Z-1)}{A^{1/3}} \tag{1.26}$$

where ρ is the mass density of the nucleus. If different modes of excitation are decoupled from each other and from any other degree of freedom, a nucleus may have, H_λ, C_λ, and D_λ as constants of motion. Under such conditions, the equation of motion can be derived from equation 1.24 and is of the form:

$$D_\lambda\frac{d^2\alpha_{\lambda\mu}}{dt^2} + C_\lambda\alpha_{\lambda\mu} = 0 \tag{1.27}$$

comparing equation 1.27 with that for a harmonic oscillator,

$$\frac{d^2x}{dt^2} + \omega^2 x = 0 \tag{1.28}$$

one can conclude that, for small oscillations, the amplitude $\alpha_{\lambda\mu}$ undergoes harmonic oscillations with frequency

$$\omega_\lambda = \left(\frac{C_\lambda}{D_\lambda}\right)^{1/2} \tag{1.29}$$

and $\hbar\omega_\lambda$ is a quantum of vibrational energy for the multipole λ. This quantity is called a *phonon* since it is a form of "mechanical" energy. Each phonon is a boson carrying $\lambda\hbar$ units of angular momentum and having a parity $\pi = (-1)^\lambda$. As explained earlier, there are several different modes of vibrational motion that a nucleus can undergo, depending on the multipole moment involved. These possible modes of vibrational motion are illustrated in Figure 1.3. In general, the $\lambda^\pi = 2^+, 3^-$ excitations systematically occur in even-even nuclei. The positive parity modes of vibrations, λ=2, are fairly common in near-spherical nuclei. β- and γ-vibrations are two forms of the $\lambda = 2$ mode. β-vibrations involve the oscillation of the nucleus along its major axis. γ-vibrations, on the other hand, involve the oscillation of the nucleus along its minor axis.

Octupole modes of vibration are seen in doubly-magic nuclei, where the ground state ($I^\pi = 0^+$) may be regarded as the zero-phonon state. The lowest vibrational state (corresponding to one-phonon vibrations) built upon this state has $I^\pi = \lambda^\pi = 3^-$ because of angular momentum coupling (i.e. $0^+ \bigotimes 3^-$). Examples of one-phonon octupole excitations are found in the form of a low-lying 3^- state in all the closed shell nuclei. Because octupole modes are negative parity modes, the expected energy ($41A^{1/3}$ MeV) for particle excitations across one major shell is about 16 MeV in ^{16}O and 7 MeV in ^{208}Pb. But the excitation energies for the observed 3^- vibrational states in these nuclei are $\sim$ 2.6 and 6.0 MeV for ^{208}Pb and ^{16}O, respectively, i.e. much less than the expected value. This is evidence that many nucleons are acting in a collective manner to lower the energy required to excite the octupole state. The observed electromagnetic transition rates between states consisting of different numbers of excitation phonons are much larger than the Weisskopf single-particle estimates. Strong $E3$-transition strength is observed in states excited by octupole vibrations (e.g. $B(E3_{3^-\rightarrow 0^+}) \simeq 34$ *W.u.* in the ^{208}Pb nucleus).

Multipole excitations such as two- quadrupole and octupole phonons occur in many nuclei. When two quadrupole ($\lambda = 2$) phonons couple together in a two-phonon quadrupole excitation, the possible angular momenta range from 0-4 ($= 2\lambda$). However, the symmetry requirements between the two identical phonons eliminate the possibilities 1^+, 3^+ and only states with 0^+, 2^+, 4^+ are left. The coupling of two octupole ($\lambda = 3$) phonons in a

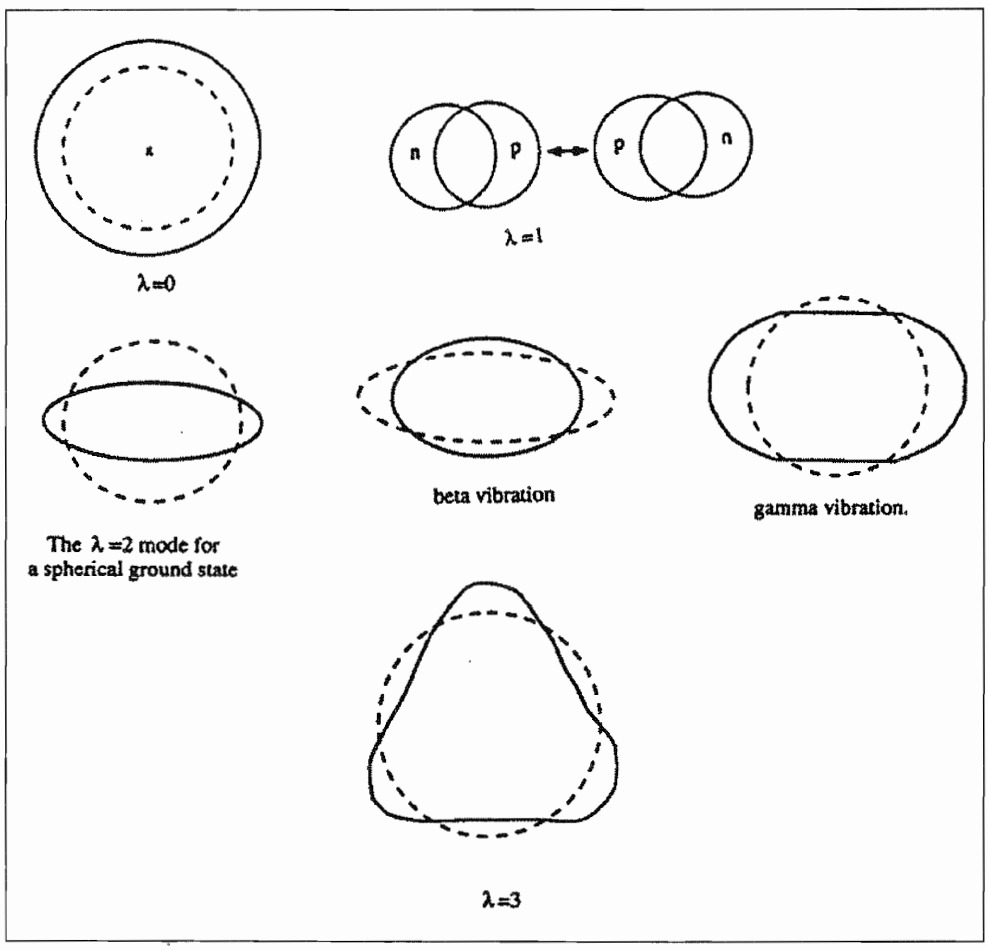

Figure 1.3 A schematic illustration of the different modes of vibration a nucleus can undergo.

two-phonon excitation, on the other hand, results in a quartet of states with $I^{\pi}=0^{+}$, 2^{+}, 4^{+}, and 6^{+}. For purely harmonic nuclear vibrations, the excitation energy for a double-phonon vibration will be twice the excitation energy of the one-phonon excitation of the same vibrational mode (i.e. same λ). In addition to purely harmonic vibrational motion, anharmonic terms may be present in a nucleus. Furthermore, vibrations may also be coupled to other modes of excitation.

1.7 Octupole Correlations

Strong octupole correlations between valence nucleons are anticipated in different mass regions of the nuclear chart. In deformed nuclei, these correlations may induce stable octupole deformation, either in the nuclear ground state or in excited states when rotation increases. In spherical nuclei, on the other hand, these correlations may induce octupole modes of vibration. Such correlations (i.e. octupole vibrations or octupole deformation) are produced by the long-range octupole-octupole interaction between nucleons. These correlations depend on the matrix elements between single-particle states with $\delta l = \delta j$=3 (where l and j are the single-particle orbital and angular momentum quantum numbers) and the energy spacing between them. Therefore, the strongest octupole correlations arise from the occurrence, near the Fermi surface, of closely spaced, opposite parity single-particle orbits with $\delta l = \delta j$=3 for both protons and neutrons. Such orbitals, with N, Z=34, 56, 90 and 136, occur near closed shells where nuclei have spherical or near spherical shapes (i.e. nuclei with β_2 close to zero). In the ^{222}Th nucleus, for example, octupole correlations arise from the interaction of the N=7 $j_{15/2}$ and N=6 $g_{9/2}$ neutrons and the N=6 $i_{13/2}$ and the N=5 $f_{7/2}$ protons. All these orbitals are lowered close to the Fermi surface in this nucleus. For nuclei with larger β_2 (i.e. having significant quadrupole deformation), these pairs of octupole-driving orbitals coincide at different nucleon numbers than the ones listed above. Regions where those states with $\delta l = \delta j$=3 come close together and octupole correlations dominate are illustrated in Figure 1.4.

Unlike quadrupole deformation, which can be deduced from measured quadrupole moments, the magnitude of the octupole deformation is difficult to determine from direct

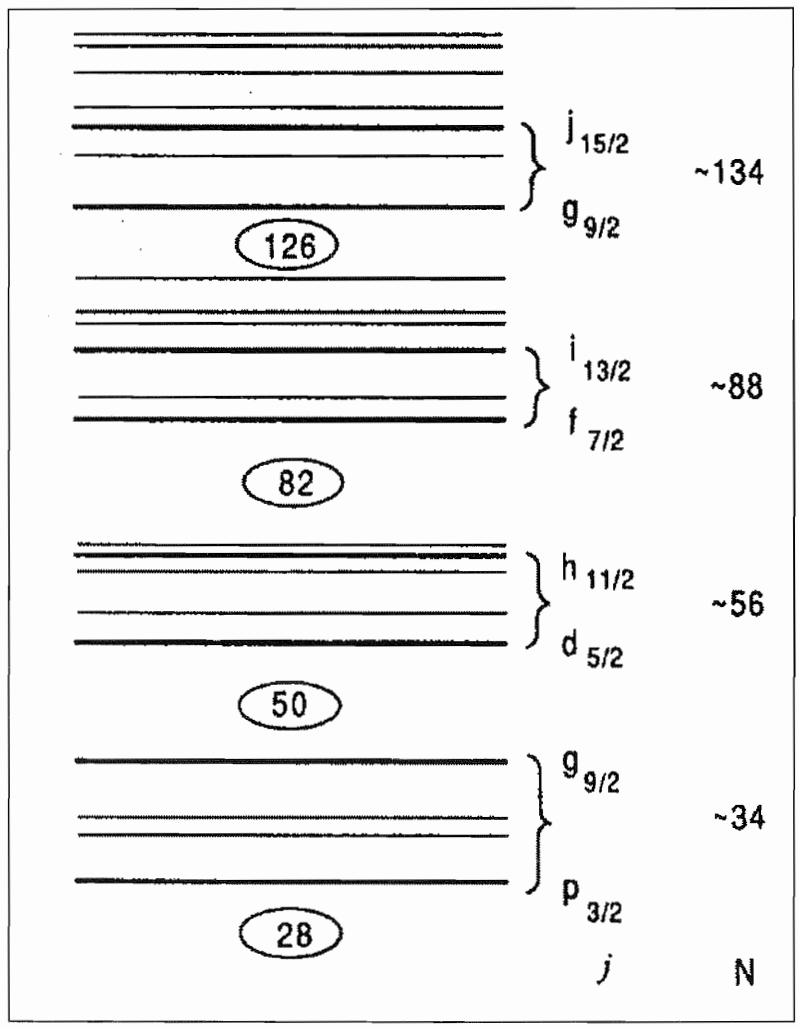

Figure 1.4 Relative energies of the shell model states for neutrons showing the locations where states with $\delta l = \delta j$=3 come close together near the Fermi surface. The numbers on the right show the neutron numbers for which octupole shape is favored. The proton single-particle states are quite similar to those shown in this Figure for the neutrons. Taken from reference [Ahm93]

measurements. Whether the nucleus is an octupole vibrator, or is octupole deformed, or has correlations of intermediate strength has to be deduced from the experimental level spectra.

1.8 Non-Collective Modes of Excitations

It is worth to mention that non-collective excitations are also available for the nucleus. In its ground state, the nucleus fills orbitals up to the Fermi level. In the case where pairing correlations are weak, if the nucleus is given an amount of energy equal to or greater than the pairing gap, it is possible for a nucleon to be excited from its original filled orbital (e.g. L_1) into an otherwise empty level with higher excitation energy (e.g. L_2). The overall properties of this excited nucleus will then be affected by the properties of the orbital (L_2). When pairing correlations, on the other hand, are not weak, the nucleus is treated using the quasiparticle formalism. In this case, the ground state for an even-even nucleus is called the *vacuum state* and the lowest quasiparticle excitation possible will be a two-quasiparticle excitation. An odd-A nucleus, in its ground state, has one unpaired particle in an orbit near Fermi surface that is not affected by the pairing force. Such nucleus is then considered as being a one-quasiparticle excitation above the vacuum. Therefore, its first possible excited state will involve higher one-quasiparticle excitations until eventually it is more favorable to form three-quasiparticle excitations. Finally, the odd-odd nucleus is treated as a two-quasiparticle excitation in its ground state.

Chapter 2

Experimental Techniques

2.1 Reactions Populating Superdeformed States

Heavy-ion induced fusion-evaporation, (HI,xn), reactions are used as a means to supply large amounts of angular momentum to the nucleus at relatively low excitation energies in order to study high spin phenomena in nuclei. In such reactions, an isotopically enriched target is bombarded by an heavy-ion beam at an energy sufficient to overcome their mutual Coulomb repulsion. The beam and target nuclei can then approach close enough to fuse. Since the compound nucleus can only accommodate a limited amount of angular momentum and excitation energy, when the beam energy is too high, the system will fission. The maximum amount of angular momentum a nucleus can accommodate and remain stable against fission is illustrated qualitatively in Figure 2.1. The calculations for Figure 2.1 were done within the liquid drop model [Coh74].

In the ^{190}Hg measurement discussed in this thesis, the beam energy utilized was approximately 10% above the Coulomb barrier at which the beam and target nuclei can fuse together forming a compound system. An estimate can be made for the maximum angular momentum of the compound nucleus by assuming that there is a sharp boundary between the elastic and inelastic reaction channels (i.e. the sharp cutoff model) [Bla54]. This is expressed as:

$$l_{max} = 0.219 R_{CB} [\mu (E_{CM} - E_{CB}]^{\frac{1}{2}} \tag{2.1}$$

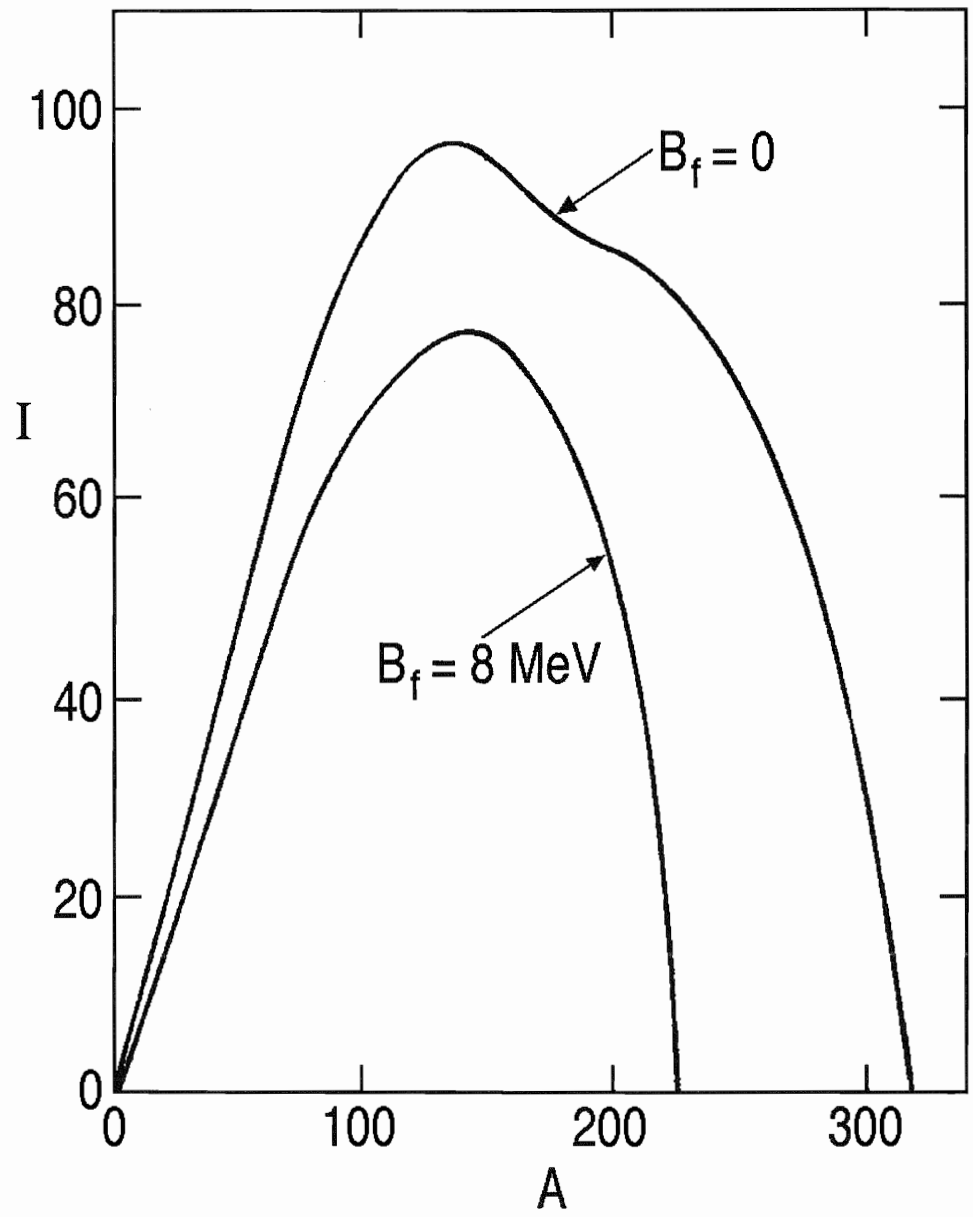

Figure 2.1 The maximum amount of angular momentum that a nucleus can acquire before fissioning in the liquid drop model. The upper curve represents the angular momentum at which the fission barrier vanishes, while the lower curve represents the angular momentum for which the fission barrier is 8 MeV, i.e. a condition where fission does not compete effectively with neutron evaporation.

where E_{CM} is the energy in the center of mass frame and μ is the reduced mass. The maximum excitation energy of the compound nucleus is:

$$E^*_{max} = E_{CM} + Q \tag{2.2}$$

where Q is the difference in rest mass energy for the system before and after fusion.

Since Q values and R_{CB} vary for different target–projectile combinations leading to the same compound system, it is possible to produce the compound nucleus with a wide range of excitation energy and angular momentum. Since superdeformation is a high spin phenomenon, the need to produce the nucleus in a state of high angular momentum is obvious. On the other hand, the superdeformed (SD) states are expected to be the states of lowest excitation energy at the highest angular momenta and, thus, a reaction leaving the least amount of excitation energy is also desirable.

To produce the ^{190}Hg compound nucleus, the choice of a 159 MeV ^{34}S beam on a ^{160}Gd target is ideal as the nucleus is produced via a (^{34}S,4n) reaction with $l_{max} \simeq 45\ \hbar$ and E^*_{max}=38 MeV. Furthermore, this beam and target combination had already proven successful in populating SD bands in ^{190}Hg in earlier experiments [Cro94, Cro95].

The compound nucleus can only exists for $\sim 10^{-20}$ s [Bla52] before it starts to get rid of its excess angular momentum and excitation energy. At first particle evaporation is the most efficient means to rid the nucleus of its excitation energy. Charged-particle evaporation (protons and alpha particles) is hindered by the Coulomb barrier and neutron emission is usually the dominant process. Neutrons, on average, carry away 8–10 MeV of excitation energy (i.e. the approximate neutron binding energy and at most 1-2 MeV of kinetic energy). The centrifugal barrier inhibits neutrons with sizable orbital angular momentum from escaping, thus most neutrons are evaporated in l=0 or l=1 states. After particle emission, the remaining excitation energy and angular momentum of the fusion evaporation product are carried away by the emission of γ rays. Following particle evaporation, the nucleus is still at a rather high excitation energy and the level density is correspondingly large. Statistical γ rays are then emitted to cool the nucleus towards the yrast line (i.e. the line which connects the lowest energy states for a given angular mo-

mentum). These transitions have been shown to be fast dipole transitions [New78, Fee77] which carry away energy, but little angular momentum. As the yrast line is approached, the decay proceeds mostly through stretched electric quadrupole transitions (though other multipolarities contribute) that remove the bulk of the angular momentum. At first, because the level density is still high, these transitions form an unresolved continuum of γ rays. Finally, when the level density is low enough, the γ cascade continues through discrete transitions until the ground state of the nucleus is reached.

2.2 Gamma-ray Detection

A photon interacts with a radiation detector (whether it be a scintillator or semiconductor device or any other material) through three main processes: the photoelectric effect, Compton scattering and pair production. In photoelectric absorption a photon incident on an atom is absorbed by one of the atomic electrons, and as a result, the electron is released from the atom with a kinetic energy equal to that of the photon minus the binding energy of the electron. In this way the full energy of the photon is deposited into the crystal. Compton scattering occurs when the photon scatters off an electron. After scattering, the photon continues at a lesser energy and can either escape from the detector or undergo further interactions. Therefore, Compton scattering can lead to the partial or full deposit of the original photon energy into the detector. Pair production corresponds to the annihilation of a photon into an (e^+,e^-) pair and, thus, only plays a role for γ rays with an energy greater than 1.022 MeV (i.e. the sum of the rest mass energies for the two resulting particles).

2.2.1 Germanium Detectors

A semiconductor detector, such as Si and Ge, is operated as a reverse biased diode [Leo87]. An energetic electron produced from one of the three processes above is promoted into the conduction band of the semiconductor and through multiple collisions produces many electron-hole pairs. The electrons are then swept toward the positive electrode with the holes collected at the negative electrode. The number of pairs collected is correlated to

the amount of energy deposited into the crystal by the photon. Ge detectors are operated at liquid nitrogen temperatures (77 K) in order to reduce the contribution of thermal electrons to the signal (the band gap in the Ge crystal is of the order of 1 eV). The bias is elevated to very near the breakdown voltage of the diode. This voltage allows for full depletion of the active detector area, and the higher field also improves charge collection efficiency.

High Purity Germanium (HPGe) detectors have several advantages over scintillators and other semiconductor devices. Semiconductor devices in general have a much better energy resolution than scintillators. In a Ge crystal it takes only 3.0 eV to produce an electron-hole pair while in a Si crystal this value is 3.7 eV. Compared to other semiconductor devices, such as a similar size Si crystal, HPGe detectors have a much better photopeak efficiency. The cross section for photoelectric absorption is approximately proportional to Z^5. Thus a γ ray incident on a Ge crystal is $(32/14)^5$ times more likely to undergo a photoelectric event than one incident on a Si crystal. A typical Gammasphere HPGe detector is a coaxial 7×7 cm^2 n–type crystal with an effective efficiency of $\sim$ 80%. This effective efficiency is defined as the ratio of γ rays registered in the detector to the number of γ rays detected in a 3" x 3" NaI crystal positioned at the same distance from the source. A typical operating voltage for these detectors is $\sim$4000 volts.

2.2.2 Compton Suppression

γ rays do not always deposit all their energy in a finite size detector. For example, Compton scattered γ rays can escape from the detector. In this case, the fraction of energy deposited in the crystal contributes to a large background underneath the photopeaks. This is not a small effect: for 1.3 MeV γ rays, for example, only 25-30% of all events are photopeaks (i.e. $\sim$ 70% of the time background events are generated) in a large Ge detector. This background can be significantly reduced by surrounding the Ge crystal with a scintillator. When a γ ray is simultaneously detected in both the scintillator and the Ge detector, the event is rejected. This process is called Compton suppression.

2.3 Gamma-Ray Arrays

A typical SD band has an intensity of less than 1% of the total γ-ray flux produced in a fusion reaction. To study such a weak structure, a highly efficient, highly sensitive γ-ray array must be used. The quality of an array depends on a number of factors such as (i) the ability to detect the full energy (i.e. the peak-to-total ratio, P/T), (ii) the efficiency of the detector (ε), (iii) the energy resolution ($\triangle\ E$), and (iv) the granularity, i.e. the number of detectors in the array. Historically, the first coincidence experiments were performed with arrays of bare Ge detectors (i.e. no suppression). Thus, these arrays of typically 5-10 Ge detectors had rather poor efficiency and P/T and the granularity was modest as well. With the advent of Bismuth Germanate as a scintillator, Compton suppression shields became available. A second generation of arrays came in use with 10-20 Compton suppressed Ge detectors surrounding an inner array of BGO scintillators. The inner array was usually used as a sum-energy, γ-ray multiplicity filter. The Argonne-Notre Dame BGO Gamma-ray Facility belongs to this second generation of arrays. More recently, the third generation of arrays has gone into operation. In these new arrays, the detection efficiency has increased because of the availability of large volume Ge detectors. The granularity has increased as well. There are more than 100 Compton suppressed Ge detectors in Gammasphere, one of these new arrays.

2.3.1 The Gammasphere Array

As stated above, Gammasphere is a powerful spectrometer due to its high resolving power (i.e. the combination of resolution, granularity, and efficiency). It consists of 110 large volume, HPGe detectors, each enclosed in a bismuth-germanate Compton-suppression shield. The detectors are arranged in a sphere around the target. Detectors that have the same latitude with respect to the beam direction are grouped in one of the 17 rings of the Gammasphere array. Each ring is at a different angle with respect to the beam direction. The entire array (i.e. 110 Ge detectors) covers approximately 2π sr. The rest of the total solid angle is covered by the BGO shielding surrounding each detector. For a Gammasphere Ge detector, the efficiency for measuring the full energy of a γ ray with

E_γ=1.332 MeV is $\sim$ 80% relative to a 3"$\times$3" NaI(Tl) detector (i.e. $0.8 \times 1.2 \times 10^{-3}$. The intrinsic energy resolution at E_γ=1.332 MeV is 2.2-2.4 keV. With such large solid angle coverage, the probability of detecting 3 or more coincident γ rays from a high multiplicity cascade is large. It has been shown that the Gammasphere array has a detection sensitivity which is $\sim$ three orders of magnitude higher than that of the old generation of γ-ray arrays such as the Argonne-Notre Dame BGO γ-ray facility. A view of Gammasphere will be presented later.

2.3.2 The Argonne-Notre Dame BGO Gamma-ray Facility

This array consists of an inner array of 50 hexagonal BGO scintillator crystals surrounded by 12 Compton-suppressed Ge detectors (CSS). The Ge crystals are 5-6 cm long and 5.5 cm in diameter. The Ge crystal of each CSS is placed inside an active shield made of BGO scintillators (for Compton suppression). The 12 CSS are arranged in two rings around the target position, these rings are positioned 14.5° above and below the beam axis, respectively. Each ring contains 6 CSS, placed at angles of $\pm$34.5°, $\pm$90°, and $\pm$145.5° with respect to the beam direction. Each of the Ge detectors has an efficiency of 25%(relative to that of a 3"$\times$3" NaI(Tl) detector) and covers a solid angle of about 1.5% of the 4π. The resolution of each CSS detector is typically $\leq$ 2.0 keV measured for the 1332 keV γ ray from a ^{60}Co source.

The BGO array is used to measure the sum-energy and multiplicity, and subtends 78% of the 4π solid angle around the target. Each of the 50 BGO element has an energy resolution of about 17% measured for the 661 keV line of ^{137}Cs. A side view of the Argonne-Notre Dame BGO Gamma-ray array is illustrated in Figure 2.2.

2.4 The Compact Heavy Ion Counter (CHICO)

The Rochester University Compact Heavy Ion Counter system (CHICO) was developed specifically to exploit the many advantages of detecting associated heavy-ion reaction products in coincidence with deexcitation γ rays using Gammasphere [Sim98]. For example, in binary reactions, detection of correlated reaction products allows the measurement

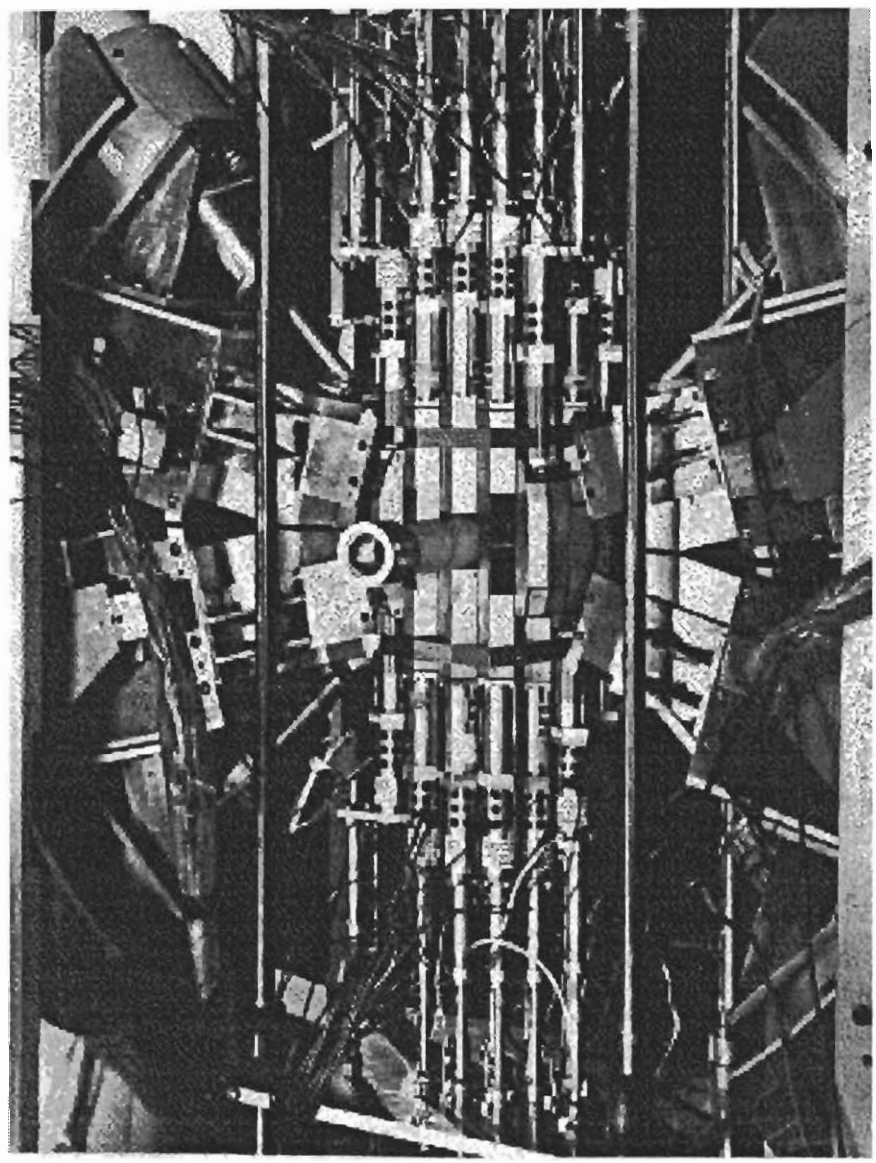

Figure 2.2 Side view of the Argonne-Notre Dame BGO Gamma-ray Array as seen from the beam direction.

Table 2.1 A brief comparison of some of the major features of the two γ-ray arrays used in the work described in the present thesis.

Array	Efficiency/detector relative to a 3"×3" NaI(Tl)	Total Ge efficiency	Resolution for 1.332 MeV γ ray	n-fold events expected
GS	$\sim$ 80%	10%	2.2-2.4 keV	3 or more
BGO	$\sim$ 25%	0.5%	2-2.2 keV	2

of scattering angle, mass and Q-value, and enables correction for the Doppler shift of the gamma rays emitted in-flight as well as the identification of the deexciting recoiling reaction products. CHICO consists of two conical arrays each containing 10 position-sensitive parallel-plate avalanche detectors (PPAC) covering a total solid angle of 68 % of 4π sr. It comprises two identical 35.6 cm hemispherical target chambers, one at forward angles and the other at backward angles. Figure 2.3 illustrates a view of half the detection system; Gammasphere and CHICO.

2.5 Electronics

A brief description of the electronics used in the measurements described in this thesis is presented in this section. In order to detect two or more coincident γ rays, electronic circuitry must be employed to determine whether the detected γ rays fall within a chosen time window. Usually, the γ rays are required to be in coincidence not only with one another but also with the beam burst (identified via the "RF signal" from the accelerator). The electronic circuitry must then insure that all relevant information (e.g. energies, times) are recorded and identify any uncorrelated random events that need to be subtracted in the subsequent analysis. Events are recorded only when these coincidence requirements are fulfilled

The logic in measuring, for example, three coincident γ rays using Gammasphere is

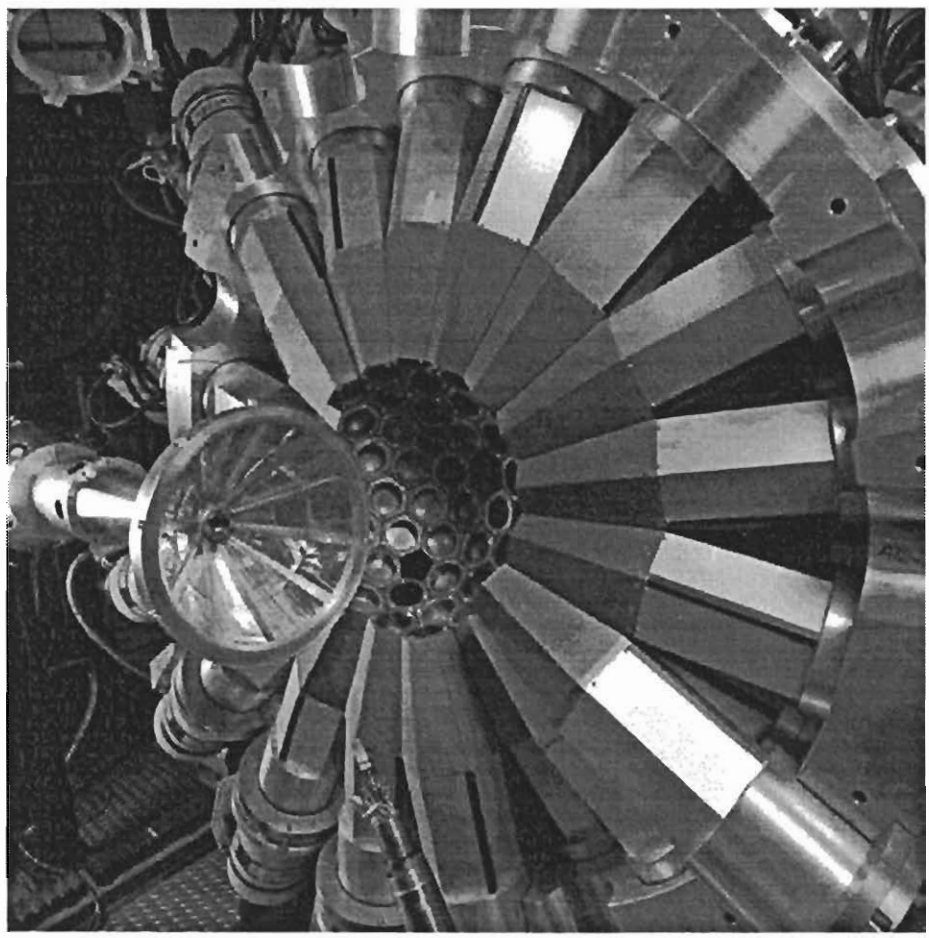

Figure 2.3 A view of one of the two hemispheres of the Gammasphere Array with a clear view of the BGO shields. In the center is one of the two identical semi-hemispheres of (CHICO). Both CHICO hemispheres comprise two identical 35.6 cm hemispherical target champers.

that three Compton suppressed Ge detectors should each detect a γ ray within a time window of 600 ns. If this requirement is met after the 600 ns, acquisition of any further detector signals is blocked. Then after 6 μs, a final inspection is done by the master trigger module. During this period, the recorded signals from the Ge detectors will be inspected for Compton scattered and pile-up signals which will be removed from the total event. After that inspection, if the original requirement is still met, the event is cleared for read out. Gammasphere electronics modules are home built based on VXI boards and crates. More details can be found in reference [Nis96].

Similar logic is followed in the case of the Argonne-Notre Dame BGO Facility. A detailed description of the electronics used at the Argonne Notre Dame BGO Facility is given in reference [Bea93]. It is worth mentioning that all electronics modules used at this facility are either standard NIM based or ECL line type modules.

2.6 Data Analysis

Different analysis techniques have been applied to the experiments described in this work. A description of the tools that have been used to analyze the high-fold coincidence data sets will be given in this chapter. The techniques employed to obtain lifetime information are discussed as well.

2.6.1 Analysis of Coincidence Measurements with the Argonne-Notre Dame BGO γ-ray Facility

$\gamma - \gamma$ Coincidence Matrices

A $\gamma - \gamma$ coincidence matrix is a convenient method to store double and higher fold events. In such a two dimensional array, the x and y axes represent the transition energies of the γ rays measured in coincidence. The coincidence matrix is constructed by incrementing the elements ($E_{\gamma 1}, E_{\gamma 2}$) and ($E_{\gamma 2}, E_{\gamma 1}$) by one each time an event occurs with γ rays of energies E1 and E2 in coincidence. Higher multiplicity events are decomposed into doubles combinations which are then used to increment the matrix.

Background Subtraction

Not all events in the coincidence matrix are photopeak events. Some events correspond to unwanted background contributions that need to be removed. One of the contributions to the background is random events, i.e. events where the γ rays have no actual time correlation. In a random event, the probability that γ_1 and γ_2 will be detected in coincidence within the prompt time interval of a beam burst is the same as the probability that γ_1 is detected in a time interval corresponding to one beam burst and γ_2 is observed in a subsequent beam burst. The available time information allows for the proper subtraction of random events by placing gates on the time parameter.

The continuum γ rays, i.e. weak γ rays that remain unresolved by the detection system, and the unsuppressed Compton events represent another source of background. Among the different possible combinations of coincidence events involving background and photopeaks in the γ-γ matrix, only the photopeak-photopeak relationships are of interest for the analysis. Therefore, a reliable background subtraction method is needed to remove all the unwanted events. The method used in this work [Pal85] assumes that a "universal" background can be used for all the channels of the matrix and that an approximation to this background is obtained by gating on a group of channels which do not contain prominent discrete lines. Let the total projection of the symmetric coincidence matrix, C(i,j), onto one axis be:

$$P(i) = P(j) = \sum_{j=1}^{N} C(i,j), \tag{2.3}$$

where N is the order of the matrix. The continuous background under the peaks of P(i) can be fit with a smooth function, f(i), which is used to normalize the background. Then the set k of background channels consists of those channels i where P(i)-f(i) is zero within statistical errors. A universal coincidence background spectrum, b(i), is then obtained by summing a large number of coincidence spectra created with gates positioned only on the background channels (k),

$$b(i) = \sum_{j \in k} C(i,j), \tag{2.4}$$

A fraction of this spectrum can be subtracted from each row of the matrix by forming

$$C'(i,j) = C(i,j) - \frac{f(i)b(i)}{\sum_j f(j)} \tag{2.5}$$

This subtraction does not remove coincidence events coming from background located beneath the peak on which the gate is placed. This contribution is subtracted in a second step. To generate the coincidence matrix that contains discrete lines only, the following step must be taken:

$$C''(i,j) = C'(i,j) - \frac{f(j)d(i)}{\sum_{j\in k} f(j)} \tag{2.6}$$

where

$$d(i) = \sum_{j\in k} C'(i,j) \tag{2.7}$$

On the average, the elements of C''(i,j) will now be zero whenever i or j are part of the background channels k.

2.6.2 Analysis of Data from Gammasphere Experiments

Data Presorting

In presorting the original data tapes obtained at Gammasphere, the data are processed in a simplified format in order to increase sorting speed. Online time alignment for the Ge detectors was done every several million events to correct for any possible shifts in the electronics. In the offline analysis, times from each Ge detector are aligned and processed through 2-dimensional (E_γ versus t) histograms on which two-dimensional gates can be set. In this way, the walk of the constant fraction discriminators caused by the poor charge collection for low-energy γ rays can be taken into account properly; i.e. the detection efficiency is not reduced at lower energies. Since only prompt information is needed in this work, a reduced time, $t_{reduced}$, is generated. This $t_{reduced}$ parameter removes the energy dependence of the Ge times at low energies and is defined as:

$$t_{reduced} = t_{rf-Ge}/HW(E_\gamma) \tag{2.8}$$

where t_{rf-Ge} is the time difference between the relevant rf pulse from the cyclotron and the individual Ge detector and HW(E_γ) is the half width of the time curve at E_γ. Time limits are subsequently set on the reduced times so that random coincidence events are removed. Only the information needed for our application; i.e. Ge reduced time, detector identification number and energy as well as the event multiplicity for prompt $\gamma-\gamma-\gamma$ and higher-fold coincidence events was extracted and written onto the presorted data tapes.

$\gamma-\gamma-\gamma$ Coincidence Cubes

A $\gamma-\gamma-\gamma$ coincidence event can be stored in a three dimensional array (so-called coincidence cube). At the location $(E_{\gamma1}, E_{\gamma2}, E_{\gamma3})$ a number is stored and incremented every time an event occurs where three γ rays with energies $E_{\gamma1}$, $E_{\gamma2}$ and $E_{\gamma3}$ are detected in coincidence. All events with multiplicity >3 are unfolded into all possible triple combinations. Software packages are available to build the histogrammed cube. The technique that has been used in this work is the Hackman-Kuehner cube which is available at Argonne [Kue92]. Once the data are sorted into such a cube, the software Levit8r written by David Radford can be used to analyze the data [Rad92]. Using Levit8r, the data can be accessed and it is possible to generate spectra gated on two γ rays. In addition, Levit8r includes programs that can fit the peaks in the spectra.

Double Gating and Background Subtraction

As mentioned above, storing the data in a coincidences cube allows for double gating where one gate is placed on γ_1 and the second on γ_2 and the resulting one-dimensional coincidence spectrum is obtained. Once again, only events that correspond to (photopeak-photopeak-photopeak) coincidences are of interest. Consequently, an appropriate method to eliminate the background, due to continuum transitions and Compton scattering is needed. The FUL (Flat Upper Limit) method was used in this work. It is a fully automated method of background subtraction which can be applied to any fold coincidence data sets [Cro95]. This method is based on the assumption that the spectrum in coincidence with the background is essentially the same for all background channels and is

appropriately represented by the one-dimensional projection. In a two-dimensional projection of the coincidence cube, P_1, B_1 are the photopeak and the flat background in one dimension while P_2, B_2 are the photopeak and the flat background in the other. The background-subtracted coincidence spectra, P, is obtained from the following expression

P=(spectrum in coincidence with P_1+B_1 and P_2+B_2)
-c_1x(one-dimensional projection in coincidence with P_1+B_1)
-c_2x(one-dimensional projection in coincidence with P_2+B_2)
+c_3(total one-dimensional projection).

The second and third terms involve one-dimensional spectra which are obtained by gating on the peaks P_1 and P_2 in the two-dimensional projection, while the last term involves the projection into one dimension of the three-dimensional space. The constants c_1 and c_2 are defined such that the number of counts in the second and third terms is equal to the height of the horizontal and vertical ridges under the peak in the two-dimensional projection. On the other hand, c_3 is determined so that the the number of counts in the final term is equal to the height of the smooth background. Determining these constants is non-trivial, and a detailed description of the FUL method is presented in reference [Cro95]. To create and view the double gated background subtracted spectra and to analyze the peaks, the Levit8r software (which allows the use of the FUL algorithm for the background subtraction) is used.

Higher Fold Coincidence Events

A high fold analysis software package called "Shrug" has also been used to analyze the presorted Gammasphere data when only coincidence events with fold $\geq$4 were of interest. For our application, the data were sorted into sums of triple-gated spectra. These gated spectra were constructed individually for each of the 17 angular rings of Gammasphere. A Doppler-shift was applied to the coincidence gates in order to shift the gate from angle to angle to follow a gating transition (in the event that this transition shifts because it

is emitted before the nucleus is fully stopped). Levit8r software is used to access these spectra.

Triple Gating and Background Subtraction

As in the case where double or triple coincidence events are analyzed, a background subtraction method is needed in a 4-fold coincidence events if meaningful coincidence relationships are to be extracted. The formalism used for the background subtraction for 4-dimensional coincidence histogram is described in details in reference [Hac95]. It is a generalization to 4 dimensions of the formulation described above in the case of $\gamma - \gamma$ coincidence matrices and $\gamma - \gamma - \gamma$ coincidence cubes. Since the formulation is too cumbersome to be described fully here, the reader is referred to reference [Hac95] for details.

2.7 γ-ray Energies and Intensities

To obtain the energy and the relative intensity of each γ ray, proper calibrations were carried out for the detection system. Photoelectric peaks with known energies and intensities from radioactive sources such as ^{56}Co, ^{243}Am, ^{182}Ta and ^{152}Eu were used. Gamma rays provided by those sources cover the region of interest for the present work, i.e. 70 keV-3.5 MeV. The energy calibration was derived from the association of the measured centroids with the known γ-ray energies of the different sources. From the same calibration spectra, the relative photopeak intensity as a function of energy can be determined by comparing the integrated area under the photopeak with the known relative intensity from the source. With the appropriate normalization factor, the relative efficiency can be transformed into an absolute efficiency if the actual activity is known for one of the photopeaks of any of the sources used in the calibration. Figure 2.4 presents the relative efficiency as a function of energy for the Gammasphere detectors.

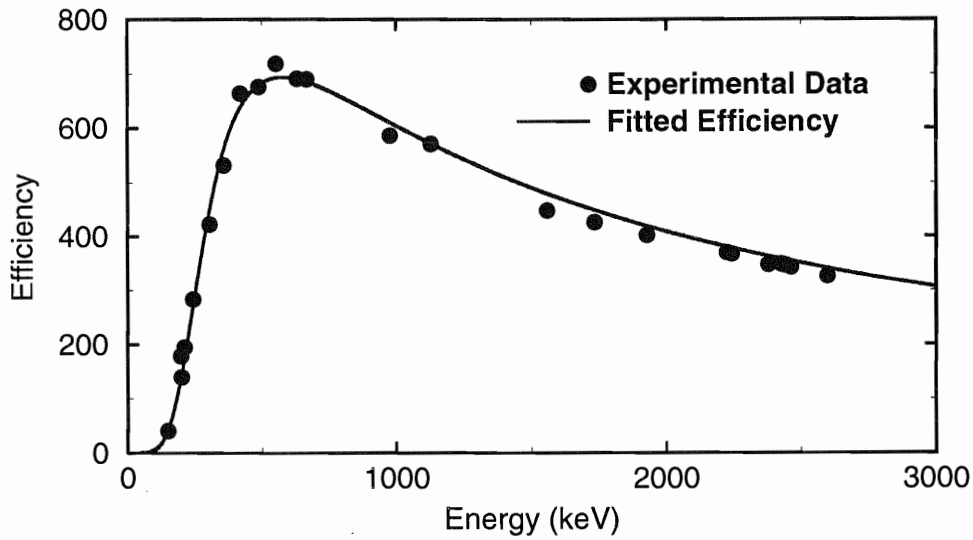

Figure 2.4 Efficiency as a function of energy for GS detectors.

2.8 The Doppler Shift Attenuation Method (DSAM)

The Doppler Shift Attenuation Method (DSAM) can be applied to measure nuclear state lifetimes below 1 psec. This method utilizes the fact that in a stopping material, typically a thin target with backing material thick enough to stop the recoiling fusion evaporation product, the magnitude of the Doppler shift becomes attenuated due to the slowing down of the recoil atoms. When recoil atoms are ejected into a vacuum, the energies of the emitted γ rays will be fully shifted and the energy shift is given by:

$$\Delta E_\gamma(\theta) = E_{\gamma 0}\beta_0 cos(\theta), \tag{2.9}$$

where θ is the angle at which γ rays are detected relative to the recoil direction, β_0 is the initial recoil velocity of the residue formed in the center of the target, E_γ is the shifted energy and $E_{\gamma 0}$ is the nominal (i.e. unshifted) energy. If these recoil atoms are passing through matter, however, they immediately begin to slow down and eventually come to rest. Since the velocity decreases continuously, the emitted γ rays vary continuously in energy from the fully shifted to the unshifted value. The profile of this energy distribution can be used to deduce lifetimes, once the mechanism for energy loss by collisions in the

backing material is understood. The average energy of the γ rays in this case can be given by

$$\overline{E_\gamma(\theta)} - E_{\gamma 0} = E_{\gamma 0} F(\tau) \beta_0 cos(\theta), \tag{2.10}$$

where $F(\tau)$, the Fraction of the full Doppler shift, is the attenuation coefficient which depends on the effective nuclear mean lifetime τ as well as on the stopping process. Thus, for any transition of the appropriate lifetime $F(\tau)$ can be obtained experimentally by measuring $\overline{E_\gamma(\theta)}$ in each of the angle sorted spectra. The unshifted γ-ray energy $E_{\gamma 0}$ can be measured at the angle θ=90°. The value of β_0 is calculated from kinematics. Finally, the lifetime of a state can be deduced from the extracted $F(\tau)$ value. The most accurate lifetime determinations with the DSAM are made when $\tau \sim \alpha$, where α is the characteristic slowing down time of the backing material.

2.8.1 Principles of the Method

When recoils travel in matter, they suffer from both electronic and nuclear stopping powers, i.e. they lose energy by Coulomb interactions with the electrons as well as by collisions with the nuclei of the target and backing material. When $\beta \geq 1\%$, electronic stopping power dominates the energy loss because of the large number of Coulomb collisions with electrons from the target and backing material. If, however, $\beta < 1\%$, the nuclear stopping power will contribute to the slowing down and will alter the recoil direction. Since experimental stopping powers are not always available for all combinations of material, beam and recoil velocities that could be used in nuclear experiments, stopping powers will be calculated from the best models available. Lifetime measurements with the DSAM then become model dependent and rely heavily on the choice of a model to calculate the stopping powers. The stopping powers calculated by the code TRIM, version 1995, by Ziegler [Zie85] were used in the present analysis. This code uses the most recent evaluation of existing stopping-power data and produces tables of both electronic and nuclear stopping powers as a function of recoil energy. In a recent DSAM analysis on Dy nuclei, detailed comparison between stopping powers from TRIM and another approach

were performed [Nis97]. In the latter approach, the tabulated electronic stopping power values of Northcliffe and Schilling [Nor70] scaled to the alpha stopping powers of Sie [Sie77] were used. While the nuclear component of the stopping power was calculated using the parameterization of Winterbon [Win68] and the multiple scattering was treated according to the Blaugrund approximation [Bla66]. The agreement between the two stopping powers was found to be satisfactory. The stopping powers produced by TRIM, the target and backing composition, and the reaction conditions were used as input parameters to a Monte Carlo simulation in order to compute the velocity profile, v(t), of the recoiling nuclei. This provides a means to measure the time from the instant the recoiling atom is formed until it is finally stopped in the backing material. The relation between the stopping power and the velocity of the recoiling nucleus is given by:

$$\frac{dE}{dx} = -M\frac{dv}{dt} \tag{2.11}$$

where M is the mass of the recoiling atom. The experimental values of the fraction of the full Doppler shift, $F(\tau)$, for the states of interest and the calculated v(t) for the recoiling nucleus can be used then to evaluate a state lifetime τ, by performing the following integral,

$$F(\tau) = \frac{1}{N_0 v_0}\int_0^\infty N_k(t)v(t)dt, \tag{2.12}$$

where N_0 is the initial number of nuclei that populate the first state at t=0 and N_k(t) is the population of state k at time t, which is a function of all the lifetimes of all its feeding states. N_k(t) is given by the Bateman equation,

$$N_k(t) = N_0\prod_{i=1}^{k-1}\lambda_i \times \sum_{j=1}^{k}\frac{e^{-\lambda_i t}}{\prod_{l\neq j}^{k}(\lambda_l - \lambda_j)}. \tag{2.13}$$

where $\lambda_i = 1/\tau_i$ and τ_i is the mean lifetime of state i. Sidefeeding cascades, branching ratios and internal conversion are included in DSAM measurements to obtain more precise results. Unfortunately, their contribution to the the uncertainty in DSAM measurements is rather small compared to the uncertainty of $\sim$ 15% that arises from the calculated stopping powers (see below). A χ^2 minimization is usually performed to the measured $F(\tau)$ values with the expression of equation (1.4). Error bars for the lifetimes are determined

by allowing the total χ^2 to change by ± 1 [Bev69]. In the literature, the systematic uncertainties associated with the stopping powers are usually estimated to be 10-15%. They have to be added in quadrature to the errors from the statistical analysis. However, it should be pointed out that these systematic errors may be less than what has been generally assumed. Indeed, recent data from the large detector arrays (Gammasphere and Eurogam) exist where lifetime measurements with the DSAM and the recoil-distance method (e.g. experiments with a plunger device which does not depend on stopping powers) have shown remarkable agreement.

Part II

Lifetime Measurements and Dipole Transition Rates for Superdeformed States in ^{190}Hg

Introduction

The interplay between a shell-correction, i.e. a quantal effect arising from the occupation of non-uniformly distributed energy levels, a liquid-drop contribution and the Coulomb energy results in the rich variety of shapes that the rotating nucleus can adopt. At high angular momentum, just prior to fission, both the liquid-drop moment of inertia and the occupation of specific shape-driving orbitals stabilize the nucleus in a so-called superdeformed shape, e.g. a highly elongated ellipsoidal shape having a major to minor axis ratio of nearly 2:1 [Jan91].

In 1962, Polikanov and co-workers discovered fission isomers while studying the systematics of spontaneous fission half lives [Pol62]. Superdeformation was then proposed for the first time to explain the fission isomers observed in these actinide nuclei as metastable states with a highly-elongated shape [Pol62, Str67]. In these fissioning nuclei, shell effects create a second minimum in the total energy surface at very large deformation. Theory predicted that similar shell effects should exist in other regions of the nuclear chart, but only when both proton and neutron shell corrections are favorable [Dud85, Cha87]. Those predictions were proven correct with the discovery of a band of nineteen discrete transitions corresponding to the rotation of the ^{152}Dy nucleus with a superdeformed shape [Twi86]. In fact, there are four regions of superdeformation known today, the actinides and three mass regions (A$\sim$80, A$\sim$150 and A$\sim$190). Each region has its own characteristics.

In the A$\sim$80 region of superdeformation, superdeformed (SD) bands show higher rotational frequencies than in any other region. As a result, this region provides a test for nuclear structure under the highest stress that can be induced by rotation. SD bands in the A$\sim$150 region extend across the largest rotational frequency range, from moderate spins (I$\sim$ 25 $\hbar$) to high spins (I$\sim$ 65 $\hbar$). This provides the best opportunity to examine the evolution of the nuclear structure with rotational frequency. Furthermore, the spins involved are sufficiently high that pairing is reduced, which provides the possibility to study in detail single particle motion in the rotating mean field (by, for example identifying the contribution of individual orbitals near the Fermi surface). SD bands in the A$\sim$190 region extend to much lower rotational frequencies than in the mass region A$\sim$150. This

region provides the best opportunity to look at pairing correlations at high spins and large deformation. These correlations can be different from those seen at normal deformation since the orbitals at the Fermi surface are different. The actinides with mass A$\sim$240, provide the best test of survival against fission.

Despite these differences, SD bands in all regions share many characteristics. First, they all consist of sequences of quadrupole transitions all in coincidence with one another and equally separated in energy. Lifetime measurements (a few cases are available) show that all SD in-band transitions are associated with the decay of very short-lived states, a characteristic of high collectivity. Finally, the intensity profile of the in-band transitions is rather unusual, i.e. the intensity increases as the transition energy decreases until a plateau is reached. The intensity then remains constant over several transitions until a decay out to normal deformed states of lower energy takes place. This decay is very abrupt, occurring over 1-2 transitions. Furthermore, at the point of decay the excitation energy above the normal deformed states is high and, as a result, the decay is statistical in nature, i.e. it occurs mostly through an unresolved continuum of γ rays.

In addition to the lowest-energy rotational sequences (called yrast SD bands) excited SD bands have also been found in many nuclei in the A$\sim$150 and A$\sim$190 regions [Cro94, Dag94]. These excited bands correspond to either quasiparticle or collective, i.e. vibrational, excitations. It is more plausible that the excited bands in the odd-A nuclei correspond to quasiparticle excitations since an odd particle can easily couple to the collective core, i.e. occupy one of the orbitals near the Fermi surface. On the other hand, because the energy needed to break a pair of particles to create quasiparticle excitations in the even-A nuclei is of the order of 1.5 MeV, collective vibrations are, perhaps, more plausible. In this respect, the situation is not different from that seen in normal deformed nuclei where the lowest excitations are most often associated with beta, gamma and/or octupole vibrations. It has been predicted that octupole vibrational modes should play a more important role in the second minimum (i.e. SD) than in the first [Dud90, Ska93, Nak95]. At these large deformations octupole collectivity is enhanced by the presence near the Fermi surface of pairs of orbitals with opposite parity and differences in angular momentum δl=3 such as

the proton $\pi(i_{13/2}-f_{7/2})$ and the neutron $\nu(j_{15/2}-g_{9/2})$ orbitals. These same orbitals are responsible for strong octupole correlations in light actinide nuclei [Naz90]. Nevertheless, until recently most interpretations of excited SD bands were in terms of quasiparticle excitations, but the latest experimental results and calculations suggest that in the A$\sim$190 and A$\sim$150 regions of superdeformation, octupole correlations could become important.

Those excited SD bands are more likely to be observed in nuclei where the excitation energy of an octupole-vibrational band is low at the spins at which SD bands are fed. Theoretical calculations [NAK96] using the random-phase approximation (RPA) predict that in the A=190 region most, if not, all excited SD bands in even-even nuclei correspond to collective, octupole vibrations. RPA calculations of all the SD, even-even Hg isotopes indicate that it is in ^{190}Hg that the octupole excitation is the lowest in excitation energy. This made ^{190}Hg the best candidate to search for experimental signatures of octupole vibrations.

Four SD bands have been observed in the ^{190}Hg nucleus, and the excited SD bands have a rather unusual behavior, when compared with excited SD bands in other nuclei of the region [Dri91, Cro94, Cro95, Wil96]. In particular, the first excited (band 2) SD band decays entirely into the yrast SD band, instead of adopting the usual decay out path directly towards the normal deformed states. The inter-band transitions, possibly of E1 character, that link this band to the yrast SD band were observed [Cro94, Cro95] and this allowed for the excitation energy, spins and possibly the parity to be determined relative to the yrast SD band [Cro95]. The excitation energy of this band, at the point where it decays into the yrast SD band, is 911 keV, i.e. lower than would be expected for a two quasiparticle excitation. Furthermore, the behavior of the dynamic moment of inertia $J^{(2)}$ for this SD band is also peculiar. Not only is it essentially flat as a function of rotational frequency, but it is also about 20% larger than that of any SD band in the A=190 region of superdeformation [Cro95]. When this excited band and it's decay pattern were observed for the first time [Cro94], it was proposed that this could correspond to a rotational band built on an octupole-vibrational phonon in the SD well. The octupole -vibrational picture became more plausible when the linking transitions were observed

and firmly established (i.e. their energies were measured and their angular distributions were found to be consistent with a dipole character E1) [Cro95]. This octupole-vibrational scenario gained even more support when the properties of the yrast and the first excited SD bands in ^{190}Hg were reproduced in RPA calculations by Nakatsukasa [Nak96]. More recently, an excited band (called bands 3) in ^{194}Hg [Hac97] and two excited bands (called bands 3 and 4) in ^{196}Pb [Bou96] were observed to decay to their respective yrast SD bands via dipole transitions with energies $\leq$1 MeV. This decay pattern, along with the low excitation energies of these bands can also be interpreted as collective, octupole vibrations in the SD well.

In spite of the existing data, the interpretation of the excited SD bands in terms of octupole excitations remains a matter of substantial debate. Further measurements are needed in order to provide answers to some of the remaining questions. In particular, some questions about the first excited SD band in ^{190}Hg need answers. First, the absolute dipole transition rates of the linking dipole transitions should be determined in order to assess the degree of collectivity. Second, the origin of the large value of $J^{(2)}$ moment of inertia needs attention. A possible interpretation would associate this effect with an unusually large quadrupole moment. Calculations using the generator coordinate method [Ska93] have predicted that the lowest octupole vibrational state would have a quadrupole moment $\sim$15 % larger than that of the yrast SD band, due to the coupling between the octupole and the quadrupole degrees of freedom. The RPA calculations [Nak96], however, explain the large $J^{(2)}$ moment as arising from Coriolis mixing among different octupole vibrational bands rather than from a large deformation. The measurement of the transition quadrupole moments Q_0 settles this issue.

In the present work, we attempt to provide answers to those essential questions raised by the existing data by performing lifetime measurements for both the yrast and the first excited SD bands with the Doppler shift attenuation method (DSAM). Using those lifetimes and the measured branching ratios [Wil96], absolute transition rates for the linking dipole transitions are obtained. The transition quadrupole moments Q_0 in both the first excited and the yrast SD bands are also extracted.

The fact that (i) no differences in deformation are found between the two SD bands, and (ii) that the absolute transition rates for the linking dipole transitions are large favor the interpretation of the excited SD band as a rotational band built on an octupole vibration.

Chapter 3

Data Analysis and Results

In this chapter, results from the (DSAM) measurement will be presented; the experimental fractions of the full Doppler shift $F(\tau)$ values for all transitions in both bands, lifetimes of superdeformed states in both bands, the intrinsic quadrupole moments Q_0 for the two bands and the dipole transition rates for the inter-band transitions.

3.1 Experimental Conditions

Superdeformed states in ^{190}Hg were populated with the ^{160}Gd(^{34}S,4n) reaction. The reaction conditions are identical to those in which the first excited SD band and the transitions linking this band to the yrast SD states were discovered [Cro94, Cro95]. The 159 MeV ^{34}S beam, with an average intensity of ~30 enA, was provided by the 88-Inch Cyclotron at the Lawrence Berkeley National Laboratory. The target consisted of 1.17 mg/cm^2 isotropically enriched ($\geq$ 95%) ^{160}Gd material evaporated onto a 12.9 mg/cm^2 Au backing which slows down and stops the recoiling nuclei. In order to prevent the oxidation of the ^{160}Gd, a 80 μg/cm^2 layer of Au was evaporated over the front surface of the target. During the experiment, an on-line monitoring procedure for target deterioration and/or target migration into the Au backing was arranged by continuously comparing the yields of transitions in ^{190}Hg with those of γ rays in ^{189}Hg, ^{191}Hg and Au. The experiment was carried out using the Gammasphere array which, at the time of the experiment, consisted

of 87 Compton-suppressed Ge detectors, 38 of which were located at backward angles, 8 at 90° and 41 at forward angles with respect to the beam direction. The events of interest were selected by requiring that at least three Compton-suppressed Ge detectors fire in prompt coincidence. A total of 2.3×10^9 events with fold $\geq$ 3 and 1.1×10^9 events with fold $\geq$4 were recorded over a three days period.

3.2 The SD Bands in ^{190}Hg

Among the four excited SD bands which have been observed in the ^{190}Hg nucleus, the yrast and the first excited SD bands are of interest in the present work. The primary goal of sorting the data was to construct the gated coincidence spectra corresponding to each of the angular rings of Gammasphere, from which the DSAM analysis could be subsequently performed. As a first attempt to look at the data, a Hackman-Kuehner coincidence cube was constructed covering the γ-ray energy range from 200-900 keV. In this cube, spectra from all detectors are considered, i.e. no angular selection and no Doppler shift correction are applied to the γ-ray energies in this cube. Double coincidence gates were placed on all combinations of transitions belonging to the previously identified yrast SD band (called band1) in ^{190}Hg [Cro94]. The cleanest double gated spectra have then been added together in order to construct a spectrum representative of all the transitions in SD band1: the resulting coincidence spectrum is shown in figure 3.1. Based on previous measurements with backed targets on SD bands in the A=190 region, one can expect sharp (stopped) peaks for the lowest SD transitions and broadened line shapes for the higher energy γ rays. The Doppler broadened shape of the transitions with energy $E_\gamma > 500$ keV is clearly visible in the spectrum of figure 3.1. Due to the fact that the second and the fourth (401 and 482 keV) members of this band are contaminated by other transitions of the same energy, no double coincidence gates were placed on these γ rays. This explains their unusual large intensity in figure 3.1.

Following the same approach to identify the first excited SD band (called band2) in ^{190}Hg [Cro94], the cube was used to construct coincidence spectra gated on the known members of this excited SD band as well as on (i) members of the yrast SD band and (ii)

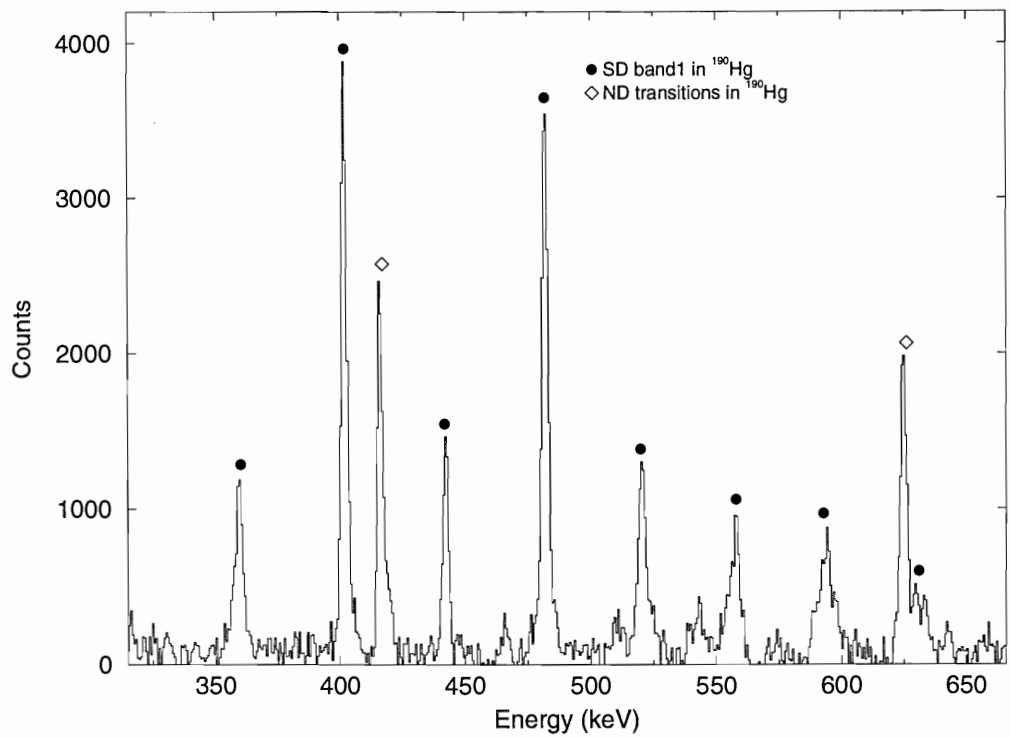

Figure 3.1 Representative sum spectrum for the yrast SD band in ^{190}Hg. This spectrum was constructed by summing all clean double coincidence spectra gated on members of this band (see text for details). The SD transitions are marked by a • symbol while transitions belonging to the normal deformed band (ND) are marked by the ⋄ symbol. Note that transitions belonging to the ND band appear in this coincidence spectrum due to the fact that the yrast SD band eventually decays into the ND band.

the inter-band transitions which link both SD bands. The cleanest double gated spectra have then been added together to construct a coincidence spectrum that shows all the transitions belonging to SD band2. Unfortunately, because of the many overlapping peaks in this sum spectrum and because the excited SD band is populated five times more weakly than the yrast SD band [Cro94], a spectrum of a quality similar to that presented in figure 3.1 could not be obtained.

It became clear then that the resolving power of an additional gating condition was required to ensure that contaminant-free spectra are obtained for the DSAM analysis. The analysis of 4-fold coincidence data was performed using the "Shrug" software package, where a number of spectra were constructed corresponding to triple coincidence gates placed on combinations of transitions in band1, band2 and the linking transitions. As explained earlier, in this analysis the spectra corresponding to γ rays detected in each of the 17 angular rings of Gammasphere were constructed individually and the appropriate background subtraction was performed.

To generate spectra for band1, coincidence gates were placed on combinations of transitions belonging to this SD band. The cleanest triple gated coincidence spectra for a particular Gammasphere angular ring were added together in order to construct the sum spectrum containing all the transitions belonging to this band at that particular angle. Transitions of SD band1 were seen clearly at each angle. To construct the equivalent spectra for SD band2, the same approach was followed but with triple coincidence gates placed on combinations of transitions in band1, linking transitions and transitions of band1 fed from band2. In this case, however, to enhance the statistical accuracy, spectra from adjacent rings were added together to produce five spectra corresponding to average angles of 33.2°, 52.4°, 89.5°,127.2° and 150.6°. The effective angles were obtained by weighting $cos(\theta)$ by the number of detectors located at a particular angle θ. For consistency, the same approach was used for SD band1 also; i.e. the five spectra corresponding to the same average angles were constructed and used in the subsequent analysis. Examples of those background subtracted spectra are presented in figures 3.2 and 3.3

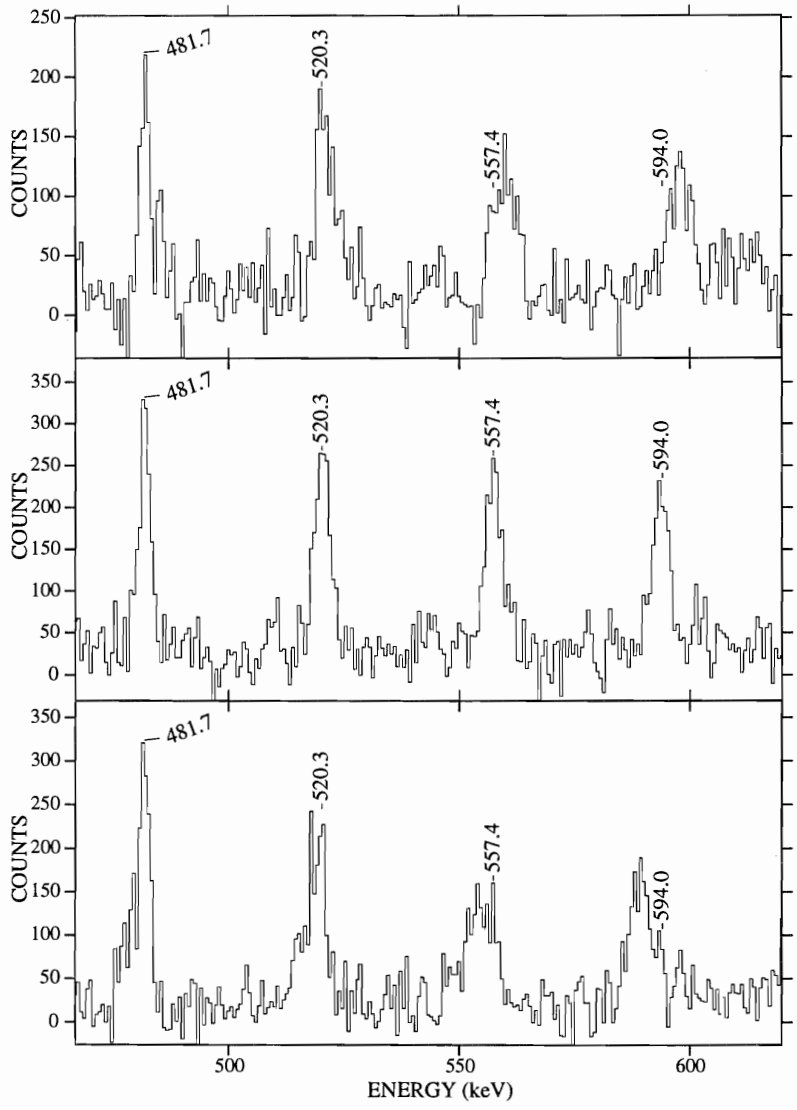

Figure 3.2 Spectra gated on transitions in band1 of ^{190}Hg as measured in detectors at 33.2°, 89.5° and 150.6° with respect to the beam direction. In these spectra, the nominal γ-ray energies of the SD transitions are marked. The Doppler shifts at forward and backward angles are clearly visible

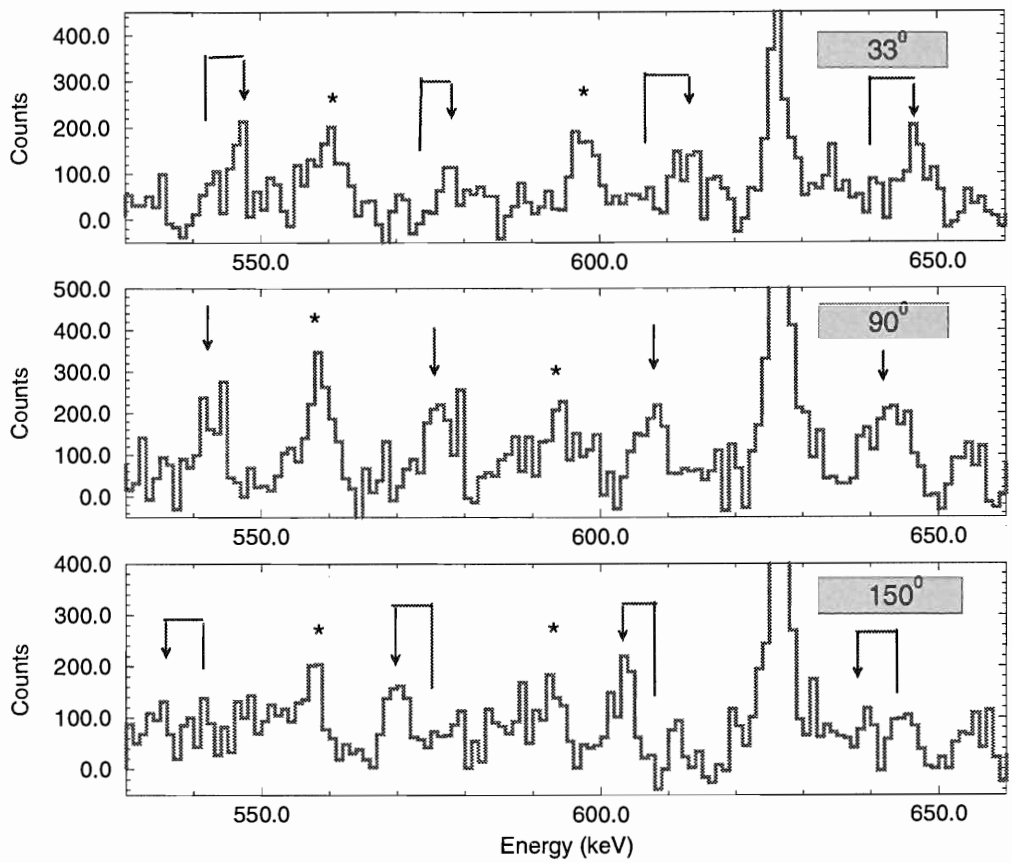

Figure 3.3 Spectra gated on transitions in band2 of ^{190}Hg as measured in detectors at 33.2°, 89.5° and 150.6° with respect to the beam direction. In these spectra, at 90° the arrow heads show the location of the unshifted energy, while at the forward and backward angles the arrow heads point to the location of the shifted energies. Note that in the forward and backward angles the tails of the arrows line up with the arrows at 90° to indicate the nominal transition energies.

3.3 The Fractions of Full Doppler Shift $F(\tau)$

As explained earlier, five sum spectra corresponding to the average angles of 33.2°, 52.4°, 89.5°,127.2° and 150.6° with respect to the beam were constructed individually for both the yrast (band1) and the excited (band2) SD bands in ^{190}Hg. The code GELIFT was then used to fit the γ rays belonging to SD band1 in each of the five coincidence spectra constructed for this band. The γ-ray centroids for all members of band1 at each of the five angles were obtained from the fits. Equivalent steps were followed to extract the centroids for the members of band2. Thus, at this stage of the analysis, the γ-ray energy, $\overline{E_\gamma}$, at each angle has been obtained for all the SD transitions of interest. These $\overline{E_\gamma}$ values were used as input to the code exp_ftau which performs a linear fit of $\overline{E_\gamma}$ versus $cos(\theta)$ for each individual transition using the first-order Doppler shift expression:

$$\overline{E_\gamma} = E_{\gamma_0}[1 + \beta_0 F(\tau) cos(\theta)] \tag{3.1}$$

where $\beta_0 = v_0/c$ is the initial recoil velocity of the residues. This quantity is determined by assuming that the reaction takes place at mid-target. Hence, the energy loss of the beam particles in the first half of the target is calculated first with the code TRIM95 [Zie85]. Then, from the kinematics of the reaction and the known E_{beam} at mid-target, β_0 is calculated to be 0.0173. Linear fits to the centroids of γ rays in band2 and to four of the inter-band transitions are presented in figure 3.4. The code exp_ftau then provides the slope of each line and calculates the $F(\tau)$ value associated with a particular transition from the expression:

$$F(\tau) = \text{slope}/\beta_0 \mathrm{E}_{\gamma_0} \tag{3.2}$$

The experimental $F(\tau)$ values for both SD bands are given in tables 3.1 and 3.2. The E_{γ_0} values were determined from the fits as well, those values are in excellent agreement with the previously published data [Wil96].

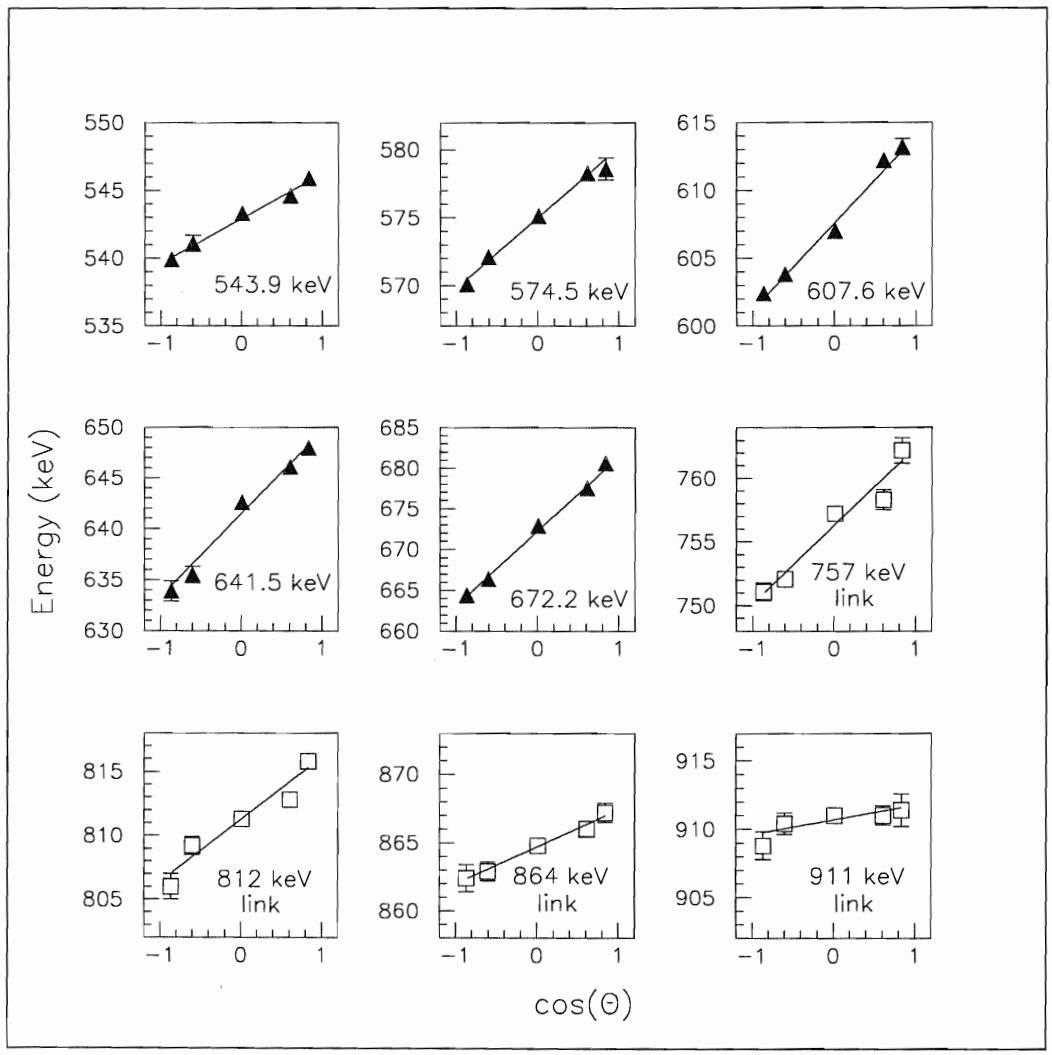

Figure 3.4 Linear fits to the γ-ray centroid energy as a function of $\cos(\theta)$ for transitions in band2 of ^{190}Hg (solid symbols) and the dipole transitions linking band2 to band1 (open symbols)

3.4 Transition Quadrupole Moments Q_0

The intrinsic quadrupole moments, Q_0, for the SD band1 and band2 were derived from the experimental $F(\tau)$ values using the computer code FITFTAU [Moo95] which requires two inputs: a velocity profile for the recoiling residues and a model for the γ-ray decay of the SD cascade. In this section both of these concepts will be discussed and the resulting quadrupole moments will be presented.

Table 3.1 The experimental $F(\tau)$ values for transitions in the yrast SD band in ^{190}Hg.

E_γ (keV)	$F(\tau)$
442.1	0.0246(15)
481.7	0.1154(12)
520.3	0.2178(17)
557.4	0.3429(19)
594.0	0.5326(14)
629.2	0.6491(25)
663.0	0.7415(17)
695.7	0.8083(21)
727.2	0.8459(24)
756.0	0.8746(21)
781.9	0.8876(21)

Table 3.2 The experimental $F(\tau)$ values for transitions in the excited SD band in ^{190}Hg.

E_γ (keV)	$F(\tau)$
542.9	0.3513(30)
575.0	0.5216(34)
607.6	0.6065(30)
641.5	0.7321(43)
672.3	0.7834(24)

3.4.1 The Velocity Profile Determination

The most recent formulation of stopping powers (included in the code TRIM95 [Zie85]) was used in the present work in order to determine the velocity profile of the recoiling nuclei. These stopping powers were used as input to a Monte Carlo simulation in order to compute the velocity profile, $v(t)$, of the recoiling nuclei through the target, and the Au backing. As stated earlier in chapter 3, the accuracy of lifetime determination depends greatly on the stopping powers calculation. The formulation of the code TRIM95 is accepted as the most accurate one, variations in stopping power calculations using different stopping powers formulation are illustrated in reference [Moo95].

3.4.2 Fitting the $F(\tau)$ Data

A fit to the experimental $F(\tau)$ values was carried out with the help of a simulation of the experimental process. To determine the average velocity as a function of time for each recoiling nucleus, the Gd target was divided into 10 equally thin slices (120 μg/cm^2). The kinetic energy for the beam for each slice is determined by taking into account the energy loss in the preceding slices. The clock is set at a time t=0 when 1000 SD nuclei

are created and distributed uniformly across the Gd target (i.e. the production cross section that corresponds to a particular beam energy in each Gd slice is assumed to be constant across the target). Time is then allowed to proceed in steps of 1.0 fs. The range of stopping times in the A=190 region is of the order of ps therefore, a 1.0 fs step is reasonable. The residues formed in each slice will slow down in the target and in the Au backing until they are eventually stopped according to the calculated stopping power $\frac{dE}{dx}$. Each recoiling nucleus is followed in time from the moment of creation until the moment it is finally stopped in the Au backing. Meanwhile, the recoiling nucleus is decaying by γ-ray emission. To proceed with the fitting, a model for the decay process is needed, such a model is described in the next section.

3.4.3 SD Cascade Model

In the code FITFTAU, the following basic assumptions are made to model the time history associated with the decay of the recoiling nucleus along a SD cascade:

1. The Q_0 quadrupole moments are the same for all SD levels within a band.
2. The side feeding into a SD state is approximated by a single rotational cascade having the same dynamic moment of inertia, $J^{(2)}$, as the main band, and controlled by a side feeding quadrupole moment Q_{sf}(assumed to remain the same throughout the entire band). The number of transitions in the sidefeeding cascade is proportional to the number of transitions in the main band above the state of interest.
3. A one-step delay at the top of all feeder cascades is parameterized by a single lifetime, T_{sf}.
4. The side feeding intensities are determined from the measured intensities within the band.
5. The competition between in-band and out-of-band decay at the bottom of a SD band (i.e. where the decay occurs) is taken into account as is a small correction for the internal conversion process.

6. The feeding delay due to the direct decay from band2 into specific states of band1 was treated explicitly by using the feeding intensities listed in reference [Wil96]. The intensities measured in the present experiment are in good agreement with those presented in reference [Wil96]. However, statistical errors on those intensities are less in reference [Wil96] because in the latter work a thin target was used, which results in peaks which are always Gaussian in shape and, hence, can be analyzed more reliably.

The mean lifetime, τ, of a particular state, which decays mainly by a γ ray of E2 multipolarity, as is the case for in-band transitions in all SD bands, is given by the expression:

$$\tau = B_\gamma \frac{8.210565 \times 10^6}{Q_0^2 E_\gamma^5 < IK20 \mid I - 2K >^2}, \tag{3.3}$$

where B_γ is the branching ratio for that state. τ is measured in units of femto-second (fs), E_γ is in MeV and Q_0 is in electron-barns (eb). The total mean lifetime of the state, τ_{tot}, is then determined by also taking into account the internal conversion process as follows:

$$\tau_{tot} = \frac{\tau}{1 + \alpha_{tot}} \tag{3.4}$$

where the total conversion coefficient, α_{tot}, for each transition was determined by extrapolation from the internal conversion coefficient tables of reference [Hag68]. The total mean lifetime for each decay step is now determined. Because this is still a radioactive decay process involving several parent-daughter decay steps, $N_k(t)$, the number of nuclei that populate a particular state k at time t, in this process is still needed. The Bateman equation can be solved as described in chapter 2 to obtain $N_k(t)$. Since each of the recoiling nuclei created in a particular layer of the target is tracked in time, the velocity at which each nucleus was moving when it emitted a particular γ ray is determined. From the information available thus far, an average $F(\tau)$ value for each SD state can be calculated from the simulation.

A fit to the measured $F(\tau)$ values using the three fit parameters; Q_0, Q_{sf}, and T_{sf} was

performed for both SD bands allowing for feeding into band1 through band2. Fitting $F(\tau)$ values of band2 was carried out first. The lifetimes derived from the best-fit parameters within this band were then kept fixed for the fit to the $F(\tau)$ values of band1. A χ^2 minimization approach yielded the best values for those fit parameters as well. The results of the fitting process are summarized in table 3.3. The quoted errors for both SD bands were determined by varying the fit parameters until the total χ^2 increased by one [Bev69]. The whole χ^2 space was mapped in this procedure to determine the covariance between the fit parameters: this is included in the quoted errors. The estimated 10-15% systematic uncertainties associated with the stopping powers are not included in the error bars. The quality of the fits can be judged from the inspection of figure 3.5. It is clear from this figure that the experimental $F(\tau)$ values for band2 are larger than those in band1. This is accounted for by the branching between the two bands, i.e. the competition between the in-band and the out-of-band decay from a particular SD state in band2, and does not come from differences in Q_0 values for both bands.

Table 3.3 Summary of centroid shift analysis results for the yrast SD bands in ^{190}Hg. The uncertainties quoted do not include the systematic stopping power uncertainties, which could be as large as 10-15%. The symbols Q_0, Q_{sf} and T_{sf} are defined in the text.

Band	Q_0 (eb)	Q_{sf} (eb)	T_{sf} (fs)
^{190}Hg (1)	$17.7^{+1.0}_{-1.2}$	$16\ ^{+5}_{-2}$	78 ± 12
^{190}Hg (2)	17.6 ± 1.5	$16\ ^{+10}_{-3}$	$80\ ^{+60}_{-50}$

3.5 Dipole Transition Rates

The lifetimes of the SD states derived from the present analysis were used to calculate the absolute transition rates for the inter-band transitions. The angular distribution of the

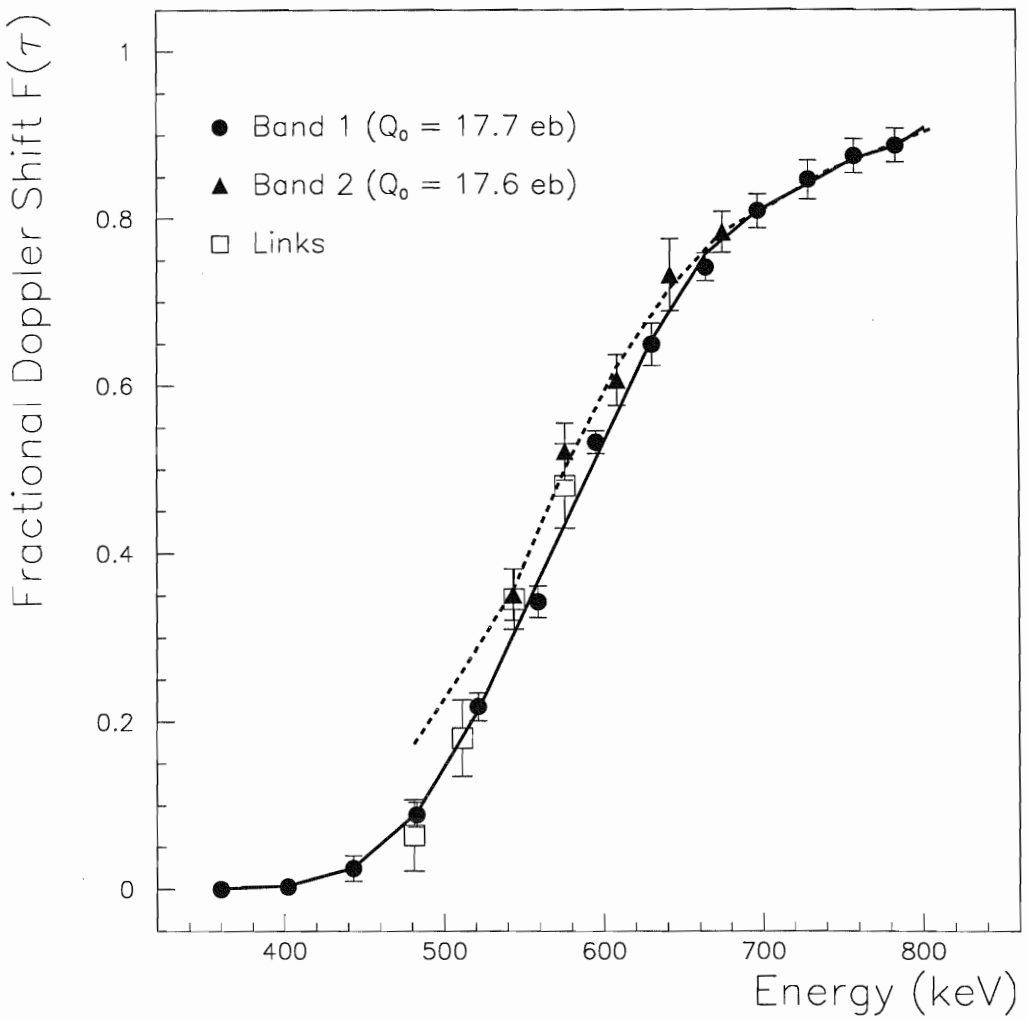

Figure 3.5 Measured fractional shifts $F(\tau)$ for γ rays in SD bands 1 and 2 of ^{190}Hg (solid symbols) and for the inter-band transitions linking band 2 to band 1 (open symbols). The $F(\tau)$ values for the inter-band transitions are plotted at the γ-ray energies of the corresponding in-band transitions of band 2. The solid and dashed curves represent the best fits corresponding to the values of the Q_0 moment given for bands 1 and 2, respectively.

inter-band transitions was measured by Crowell *et al.* [Cro95]. The observed patterns were found to be consistent with what is expected for dipole transitions, but the error bars are quite large, reflecting the fact that the transitions are rather weak. Information about the multipolarity character, e.g. *E1* versus *M1*, of the inter-band transitions is not available as it would require the measurement of linear polarization or of conversion electrons. Therefore, the inter-band transition rates should be calculated under the assumption of the inter-band transitions are either electric or magnetic in character. Under the assumption of $E1$ character for these transitions, the reduced transition rates, $B(E1)$, are given by the expression:

$$B(E1) = 6.288 \times 10^{-16}\mathrm{B.R.}/\tau \mathrm{E}_{\gamma}^{3} \tag{3.5}$$

where $B.R.$ is the out-of-band branching ratio listed for each transition in reference [Wil96], E_{γ} is the γ-ray energy in MeV, and τ is the mean lifetime of the SD level in seconds. On the other hand, if the inter-band transitions are of pure $M1$ character, the corresponding $B(M1)$ rates are given by:

$$B(M1) = 5.687 \times 10^{-14}\mathrm{B.R.}/\tau \mathrm{E}^{3}{}_{\gamma} \tag{3.6}$$

The derived $B(E1)$ and $B(M1)$ strengths, converted to single particle (Weisskopf) units are presented in table 3.4 along with the mean lifetimes for the SD states from which the inter-band transitions decay. The out-of-band branching ratios of reference [Wil96] are given as well.

Table 3.4 The reduced matrix elements assuming pure $E1$ and $M1$ radiation for the inter-band transitions are given in terms of Weisskopf units (W.u.). The branching ratios were taken from reference [Wil96], and the mean lifetime for SD levels were derived from the best fit to the $F(\tau)$ data as described earlier.

Transition energy(keV)	Inter-band branching ratio	Lifetime of level(fs)	B(E1) (W.u. x10^{-3})	B(M1) (W.u.)
757	0.23(8)	110(20)	1.5(6)	0.16(6)
812	0.29(10)	130(30)	1.2(5)	0.13(5)
864	0.50(16)	100(20)	2.3(9)	0.25(9)
911	0.67(27)	110(20)	2.5(11)	0.26(12)

Chapter 4

Interpretation

As discussed earlier, excited SD bands have been found in many nuclei in the A$\sim$150 and A$\sim$190 regions of superdeformation [Cro94,Dag94,Nak95]. These excited bands can be understood as rotational bands built on either quasiparticle or collective excitations [Nak96]. In most cases the excited SD bands have been interpreted as quasiparticle excitations, i.e. the excited SD bands can be understood in terms of excitations of particles across the Fermi surface in the deformed mean field. But the latest experimental results and calculations suggest that, in the A$\sim$190 and A$\sim$150 regions of superdeformation, octupole correlations in the second minimum should be expected.

Calculations (assuming quasiparticle excitations) are successful in reproducing the properties of almost all SD bands in the A$\sim$190 region of superdeformation. However, the first excited SD band in ^{190}Hg does not fit in the quasiparticle scenario. Therefore, a comparison between new calculations (where both quasiparticle and collective excitations in the second minimum are included) and the experimental results (of previous work as well as the present work) will be made in order to investigate the possibility that collective excitations occur in the second minimum of this nucleus.

4.1 Quasiparticle Excitations and the SD bands in the A∼190 Region of Superdeformation

In order to understand the structure of the SD bands, comparisons between the experimentally observed properties of these bands (i.e. spins, parities, and excitation energies for the SD levels) and calculations attempting to reproduce the data are desirable. Unfortunately, the only information obtained from the experimental investigations of the SD bands in all regions of superdeformation is limited thus far to the transition energies of the members of the SD bands, and to lifetimes of the SD states (limited to few cases). Only in the case of ^{194}Hg [Kho96] and ^{194}Pb [Lop96,Hau96] have the spins, excitation energies, and the likely parities (the actual parities in the case of ^{194}Pb) of the yrast SD levels been established from the observation of their direct decays to the normal-deformed levels through one-step γ rays. In the case of ^{194}Hg, those quantities are also known for an excited SD band both from the direct decays to the normal-deformed levels and from the observation of transitions linking this band to the yrast SD levels [Hac97]. In view of the experimental difficulty to find the transitions linking the SD states to the normal deformed levels, another probe that can be derived from the measured quantities (i.e. γ-ray energies) associated with the SD bands is needed to investigate the evolution of nuclear structure with rotation and to provide insight into the associated microscopic structure. The dynamic moment of inertia, $J^{(2)}$, fulfills this demand (i.e. $J^{(2)} = \frac{4\hbar^2}{\delta E_\gamma}$) and has been for a long time the only quantity giving clues regarding the associated physical phenomena. Thus, a comparison between the behavior of the derived $J^{(2)}$ moment as a function of rotational frequency, $\hbar\omega$, and the results of calculations attempting to reproduce the data is often employed to examine the microscopic configuration associated with a particular SD band.

In the even-even nuclei of the A∼190 region of superdeformation, most of the experimental $J^{(2)}$ values available exhibit a smooth rise with rotational frequency as illustrated in Figures 4.1 and 4.2 for the Hg and Pb isotopes.

According to mean-field calculations (based on quasiparticle excitations), this behavior can be attributed to three major factors contributing either separately or cooperatively:

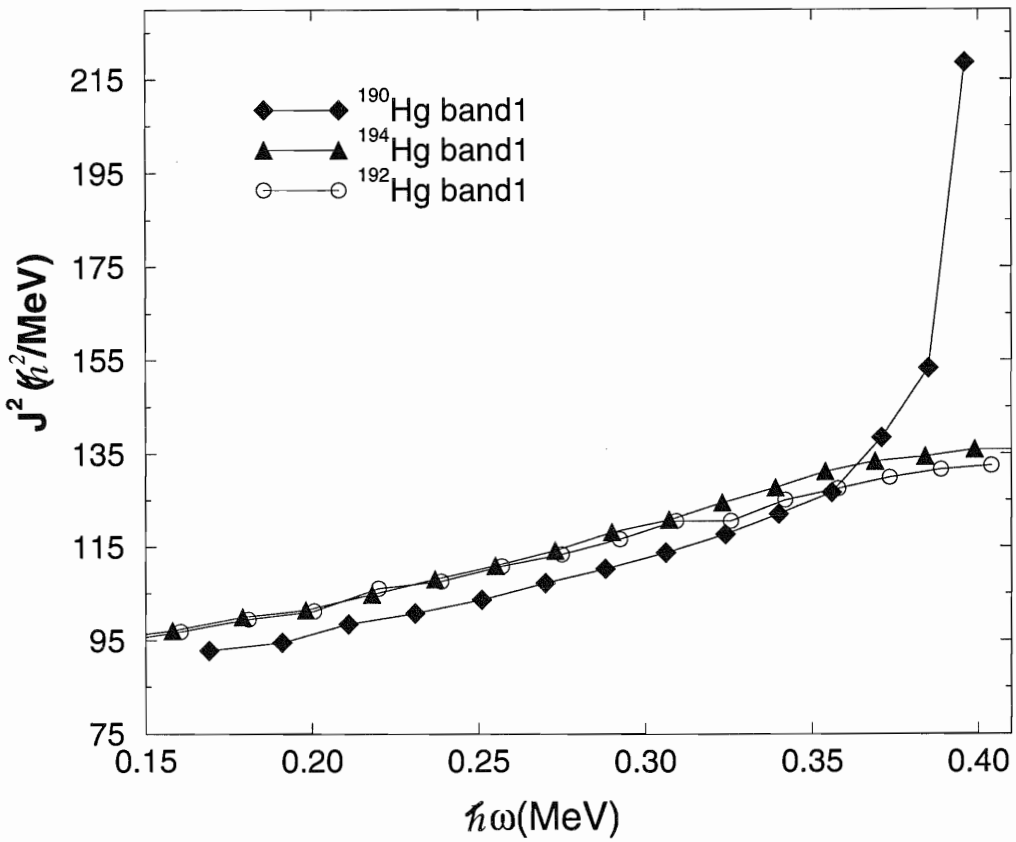

Figure 4.1 Evolution with rotational frequency of the dynamic moment of inertia, $J^{(2)}$, of the yrast SD bands in ^{190,192,194}Hg.

(i) the presence of pair correlations, (ii) centrifugal stretching (i.e. changes in deformation), and (iii) the occupation of specific high-N orbitals (i.e. high-N orbitals located two major shells higher at sphericity, which plunge down as a function of deformation and approach the Fermi surface at very large deformation, in this case $i_{13/2}$ protons and $j_{15/2}$ neutrons). The second possibility has been ruled out some time ago on the basis of detailed DSAM lifetime measurements for the yrast SD band in ^{192}Hg, which established that the quadrupole moment (and by implication the deformation) is essentially constant for all in-band transitions [Moo90]. This leaves only the possibility of pair correlations and/or of the occupation of specific high-N orbitals to account for the rise of the $J^{(2)}$ moments. Most of the data displayed in Figures 4.1 and 4.2 can be understood in the framework of cranked shell model calculations using a deformed Wood-Saxon potential with the inclusion of contributions from both factors. In particular, the inclusion of pairing in these calculations is essential to achieve a good description of the SD bands in even-even nuclei of A$\sim$190 region and to reproduce the data [Jan91]. In this framework, the interpretation of the rise of $J^{(2)}$ with $\hbar\omega$ is due to the gradual alignment of quasiparticles occupying high-N intruder orbitals (originating from the $i_{13/2}$ proton and $j_{15/2}$ neutron shells) in the presence of pair correlations. It is a direct consequence of this interpretation that, after the quasiparticle alignments are completed, the $J^{(2)}$ moments will exhibit a sudden drop at the highest frequencies $\hbar\omega$. This effect has been observed in the ^{194}Hg nucleus [Ced94]. Mean field calculations reproduce this effect fairly well, though, only when higher order corrections such as configuration-dependent pairing (e.g. quadrupole pairing) are included [Ced94].

Furthermore, in the quasiparticle excitation picture, Pauli blocking of high-N intruder orbitals is expected to induce a flattening of the $J^{(2)}$ moments of inertia in odd-even and odd-odd nuclei. Such an effect is indeed observed for two SD bands in the odd-odd ^{192}Tl nucleus, where $J^{(2)}$ moments have values comparable to those of other nuclei in the A$\sim$190 region, but exhibit little variation with $\hbar\omega$ [Fis96]. In odd-even nuclei, the presence of Pauli blocking is more subtle but can be seen in detailed comparisons of $J^{(2)}$ moments of bands in odd-even and even-even nuclei, as discussed in reference [Jan91]. The SD bands in the

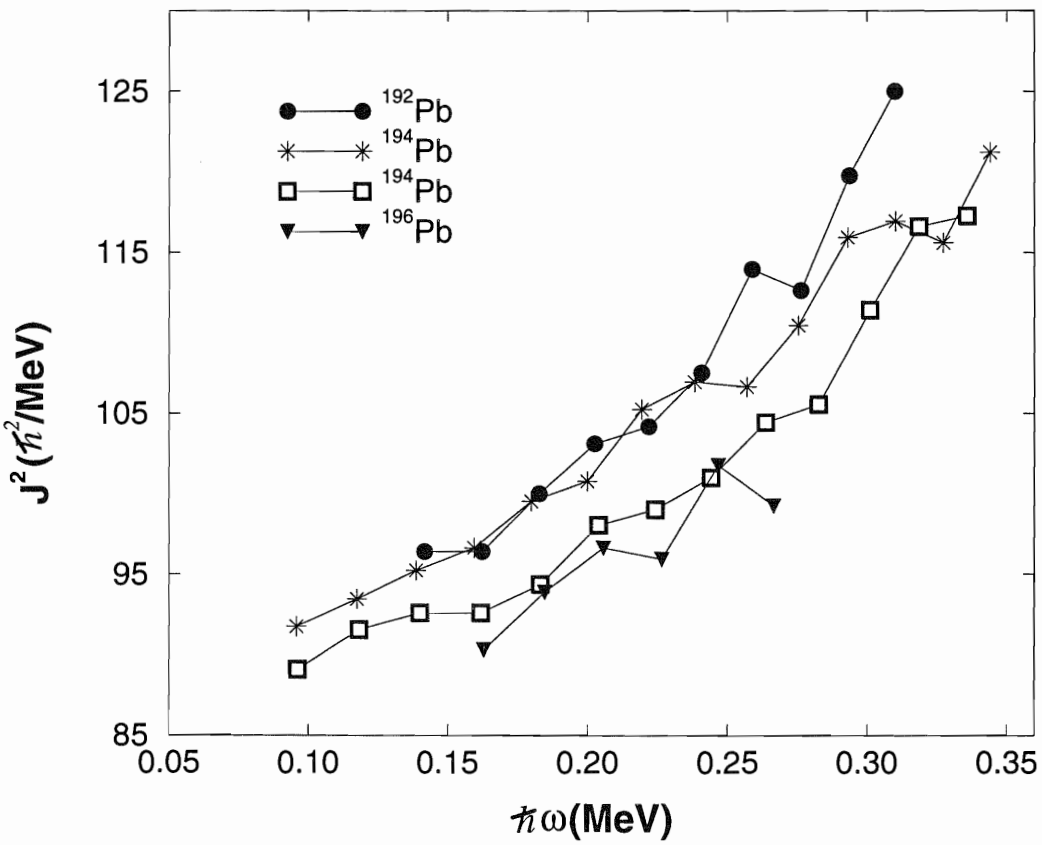

Figure 4.2 Evolution with rotational frequency of the dynamic moment of inertia, $J^{(2)}$, of the yrast SD bands in ^{192,194,196,198}Pb.

odd-even ^{193}Hg nucleus illustrate another success of the quasiparticle excitation picture. Dipole M1 transitions linking signature partner SD bands in this nucleus were observed. From the available information on the branching ratios and the quadrupole moments, the $B(M1)$ strengths for the inter-band transitions were determined. From these data, the g factors for the energy levels were extracted and were compared with the values computed for the configurations proposed on the basis of mean-field calculations using cranked Wood-Saxon potential [Joy93]. Excellent agreement was found. More recently, similar results have been reported for odd Tl nuclei in reference [Bou96], showing that theory applies with equal success to odd protons and neutrons.

In summary, the quasiparticle excitation picture seems to work successfully (when used in mean-field calculations) and reproduces a good fraction of the data available on the SD bands in the A$\sim$190 region of superdeformation, yet this picture may not suffice as is discussed below.

4.2 Collective Excitations in the Second Minimum

Because of the fact that SD nuclei have large single-particle shell gaps ($0.7 \leq \Delta \leq 1.0$ MeV depending on the theoretical estimate), collective excitations should also be considered. In many ways the situation is similar to that seen in normal deformed nuclei, where the lowest excited bands often correspond to collective β, γ or octupole vibrations while two-quasiparticle bands can be found at higher excitation energies. In SD nuclei, the large deformation brings together orbitals from several spherical shells creating a new shell structure. This novel shell structure has an influence on the types of surface vibrational modes which will be favored. For example, the presence near the Fermi surface of orbitals with opposite parity and δl=3 is expected to favor octupole shape vibrations. The presence of collective excitations in the SD well, especially those associated with octupole degree of freedom, has been predicted in different theoretical calculations [Dud90,Ska93,Bon91,Naz92]. This is mainly due to the fact that some pairs of orbitals such as the $i_{13/2} - f_{7/2}$ proton pairs and the $j_{15/2} - g_{9/2}$ neutron pairs, which are responsible for strong octupole correlations in light actinide nuclei [Naz90], also appear close to

the Fermi surface in SD configurations around ^{152}Dy and ^{192}Hg. One of the experimental signatures for such modes of collective vibrations, calculated within the Random Phase Approximation (RPA), is the occurrence of strong E1 transitions connecting the excited octupole vibrational states to the yrast SD levels [Nak96]. This is due to the fact that inter-band decays can only compete with the highly collective in-band decays if they themselves are collectively enhanced. In very few cases (band2 and possibly band3 in ^{190}Hg [Cro95,Wil96], band3 in ^{194}Hg [Hac97], and bands 3 and 4 in ^{196}Pb [Bou96]) have excited SD bands in the A$\sim$190 region been found to decay to their respective yrast SD bands through dipole inter-band transitions with energies $\leq$ 1MeV. In the A$\sim$150 region, such decay pattern have been observed for band6 in ^{152}Dy [Dag95], band5 in ^{150}Gd [Fal94], and perhaps band3 in ^{148}Gd [Ang96]. The theoretical predictions of octupole correlations in the second minimum gained additional strength from the observation of such excited SD bands.

4.3 Random Phase Approximation (RPA) Calculations

Calculations based on the Random Phase Approximation (RPA) using the cranked Nilsson potential and including both quasiparticle excitations and octupole collectivity have been performed by Nakatsukasa et. al. to investigate the octupole correlations for excited SD bands in ^{190,192,194}Hg [Nak96]. A constant quadrupole deformation parameter ϵ=0.44 is used, and pairing is allowed to vary and decrease dynamically with increasing frequency. In these calculations, the vibrational K=2 component of the octupole phonon is the lowest in excitation energy at zero frequency as illustrated in Figure 4.3. In fact, at ω_{rot}=0 the properties of the lowest K=2 octupole states in all three ^{190,192,194}Hg isotopes are almost identical. However, they evolve differently with rotation and the interplay between rotation and vibrations produces different effects depending on the neutron number. Figure 4.3 [Nak96] shows the evolution of the calculated RPA eigenvalues of the negative-parity states for the SD ^{190}Hg nucleus. It can clearly be seen in this figure that the energy spacing between the K=2 and the K=0,1 octupole states is relatively close. This causes (i) the K=2 octupole level to experience significant Coriolis mixing and (ii) the octupole

phonon to align along the rotational axis as frequency increases. It is because of this mixing (namely the mixing of K=0 and 1 components) that band2 decays into band1 via $E1$ transitions. The calculations suggest $B(E1)\sim 10^{-6}$-10^{-4} W.u. for the K=2,α=1 excited band. Assuming the proposed (K=2,α=1) configuration for band2, the value of the dynamic moment of inertia, $J^{(2)}$, as a function of frequency was calculated and it compares well with the available experimental data as will be illustrated in a later section.

4.4 SD Bands in ^{190}Hg Nucleus

Four SD bands, the yrast band and three excited SD bands, have been observed in the ^{190}Hg nucleus: the relevant spectroscopy studies can be found in references [Cro95,Wil96]. Information on the transition quadrupole moments for the yrast SD band and the first excited SD band (band2) as well as the dipole transition rates connecting these two SD bands comes from the present work. In this section the properties of each SD band will be discussed and compared with those predicted by calculations in order to investigate the associated microscopic configuration.

4.4.1 The Yrast SD Band

The evolution of the $J^{(2)}$ moment of inertia with $\hbar\omega$ of the yrast SD band (band1) is illustrated in Figure 4.1 where several features can be observed. At frequencies $\hbar\omega \leq 0.32$ MeV, the $J^{(2)}$ moment displays a smooth rise with $\hbar\omega$ similar to that of the yrast SD bands in the ^{192,194}Hg nuclei. However, the absolute value of the $J^{(2)}$ moment is about 6 $\hbar^2$/MeV lower. In general, it has been suggested that lower $J^{(2)}$ moments may be a result of: (i) a smaller β_2 deformation, or (ii) the occupation of a smaller number of intruder orbitals, or (iii) changes in pairing forces and/or the presence of octupole correlations. With the results of the present work, the first possibility can now be ruled out on the basis of the comparison between the Q_0 moments (and by implication the deformation) of the yrast SD bands in ^{190,192,194}Hg. Table 4.1 compares the results of recent calculations using a variety of theoretical models with the values presented in reference [MOO97] for ^{192,194}Hg nuclei and in the present work for ^{190}Hg nucleus.

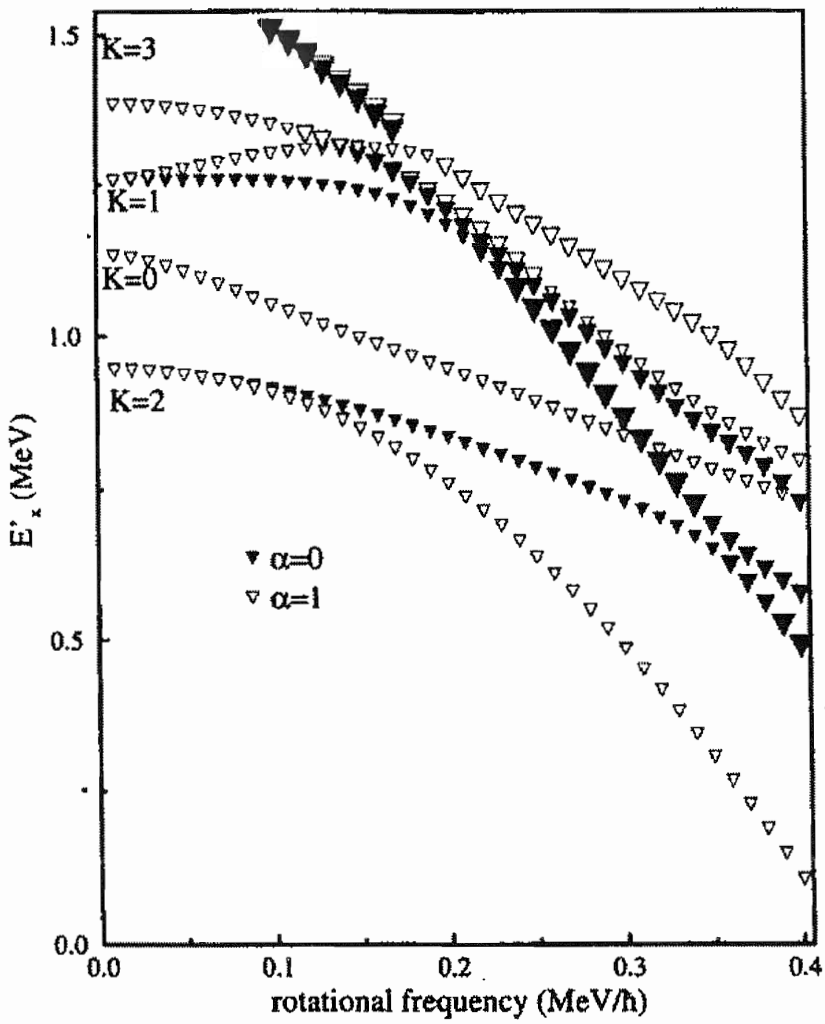

Figure 4.3 The evolution of the eigenvalues obtained by the RPA calculations (with fixed pairing gaps) of the lowest negative-parity states calculated relative to the yrast SD states in the SD ^{190}Hg nucleus. The open symbols indicate states with α=1; the solid symbols indicate states with α=0. The size of the symbols indicates the approximate degree of collectivity of a particular state.

Band	Expt.	CHA	SAT	GAL	GIR	KRI	BON	MEY	HEE
^{190}Hg	17.7 ± 1.1	19.0	19.1	18.3			17.6[1] 16.0[2]	18.1[1]	
^{192}Hg	17.7 ± 0.8	19.2	19.9	18.6		18.0	18.5[1] 17.5[2]	18.2	18.5
^{194}Hg	17.7 ± 0.4	19.3	19.5	18.5	18.4		18.5[1] 18.0[2]	18.5	18.6

Table 4.1 Experimental and calculated intrinsic quadrupole moments for SD bands in ^{192,194}Hg. The calculated results are taken from Chasman [Cha89], Satula et al. [Sat91], Gall et al. [Ggl94], Girod et al. [Gir94], Krieger et al. [Kri92], Bonche et al. [Bon90], Meyer et al. [Mey92], and Heenen et al. [Hee96]. The Q_0 values presented for the calculations of Chasman were derived from the values of the ν_2 and ν_4 deformation parameters given in the original paper. All quadrupole moment values are in *eb*.

[1]Obtained from Hartree-Fock + BCS calculations.
[2]Obtained from generator coordinate method calculations.

While the ^{192,194}Hg isotopes were studied with ^{48}Ca-induced fusion-evaporation reactions where the recoiling nuclei have a different velocity profile than in the present case, it is worth noting that in all the measurements (a) the recoiling nuclei were stopped in Au backing and (b) the same stopping power parameterizations and analysis codes were used. Furthermore, an added degree of confidence in these stopping powers comes from the observation that good agreement has been noted between Q_0 measurements performed with the DSAM and recoil-distance techniques (the latter technique does not rely on calculated stopping powers) in the case of the SD band1 in ^{192}Hg [Wil94]. Thus, it is interesting to compare the absolute Q_0 values measured for the three yrast SD bands of the even Hg isotopes.

It is clear from table 4.1 that: (1) within the experimental uncertainties, all three SD bands have the same quadrupole moment, (2) the agreement between experiment and theory is quite satisfactory, although there is a tendency for theory to give somewhat larger Q_0 values. The most important conclusion to be drawn from this comparison is that the

similarity in Q_0 values seen in the data is also present in the calculations, reflecting the fact that the additional neutron orbitals occupied in ^{194}Hg (with respect to ^{192,190}Hg) and in ^{192}Hg (with respect to ^{190}Hg) are not shape driving (i.e. the SD minimum in this mass region is very stable with respect to neutron number and orbital occupation). Furthermore, if the reduction in $J^{(2)}$ moment of the yrast SD band in ^{190}Hg nuclei relative to that in ^{192,194}Hg was due to a change in deformation (in addition to the lighter mass), a difference between respective Q_0 moments, $\delta Q_0 \sim 3\ eb$, would have been expected. Such a difference is well outside the experimental limits and possibility (i) above can be ruled out.

The second possibility can be ruled out also. Since the number of proton intruder orbitals is the same in all Hg isotopes, and because the rise with frequency of the $J^{(2)}$ moment in ^{190}Hg nuclei exhibits a slope similar to that of $J^{(2)}$ moments in the ^{192,194}Hg nuclei, it is very likely that the alignment process is similar. Hence, the same number of $j_{15/2}$ neutron intruder orbitals would be involved. This conclusion is also supported by all available cranked shell model calculations.

This leaves the possibility that changes in pairing forces and/or octupole correlations are involved ($J^{(2)}$ moments are known to be very sensitive to both effects). In the ^{190}Hg nucleus, the Fermi surface is located below the N=112 SD shell gap, a feature which may affect the pairing forces as the density of orbitals available increases. The ^{190}Hg nucleus is also expected to exhibit the strongest octupole correlations among all the Hg isotopes [Dud90]. Such correlations are expected to impact the excitation energies as well as the evolution with $\hbar\omega$ of the orbitals located near the Fermi surface.

For higher frequencies, the $J^{(2)}$ moments for ^{190}Hg become larger than those for ^{192,194}Hg and a sharp rise occurs at the highest frequencies (see Fig. 4.1). As shown in reference [Car93,Bea92], this sharp rise can be attributed to the combination of a dynamic reduction of the pairing correlations with increasing rotational frequency $\hbar\omega$ and to a band crossing with a configuration having a larger aligned angular momentum (i.e. between the zero-quasiparticle SD band and a rotation-aligned $(j_{1/2})^2$ neutron band).

The evolution of $J^{(2)}$ moments with $\hbar\omega$ has not been reproduced in cranked shell model calculations as well as one might hope. This failure is still an open question, although it

has been suggested in [Bea92] that the presence of a strong residual neutron-proton (np) interaction and /or higher order corrections to the pairing field could be responsible for the unsatisfactory reproduction of the evolution of the $J^{(2)}$ moments with $\hbar\omega$.

4.4.2 The First Excited SD Band in ^{190}Hg

The first excited SD band is characterized by a moment of inertia, $J^{(2)}$, strikingly different from those of other SD bands in even-even SD Hg isotopes: indeed, $J^{(2)}$ is essentially constant with rotational frequency and is also about 20% larger in magnitude than the $J^{(2)}$ moments of other SD bands in the even-even SD nuclei of the A $\sim$ 190 region of superdeformation. The behavior of the $J^{(2)}$ moment of this band relative to that of the yrast SD band in ^{190}Hg is illustrated in Figure 4.4.

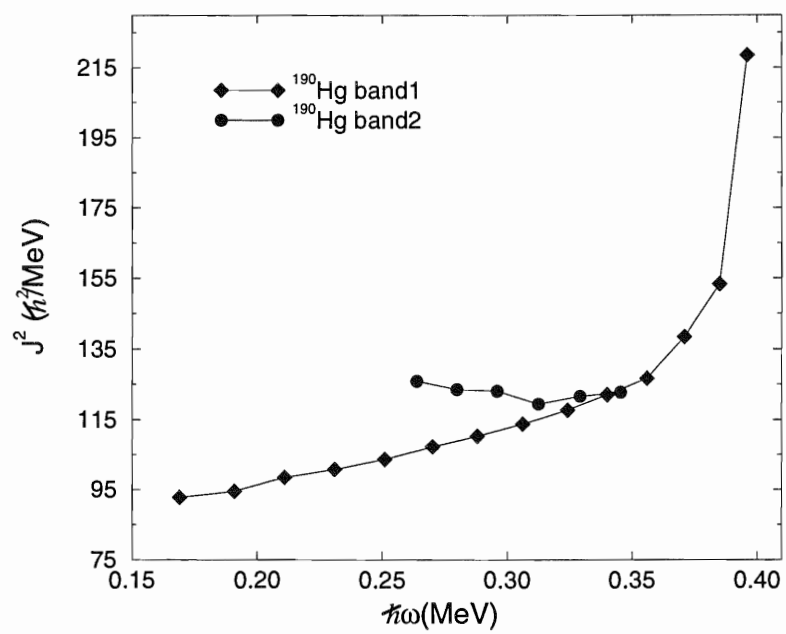

Figure 4.4 Comparison between the evolution of the dynamic moment of inertia with rotational frequency of the first excited SD band and the yrast SD band in ^{190}Hg.

Furthermore, this band entirely decays into the yrast SD states rather than to the normal deformed states, the usual decay out path of SD bands: strong dipole transitions

linking this SD band to the yrast SD band were observed [Cro94,Cro95]. The excitation energy of this band relative to the yrast SD band was established from the observation of these transitions; the lowest state in band2 is only ~911 keV above the yrast SD band. This is much lower than what would be expected for quasiparticle excitations (i.e. Δ_p =0.6 MeV and Δ_n =0.8 MeV). The relative position of the yrast SD band and this excited SD band along with the linking transitions are presented in Figure 4.5.

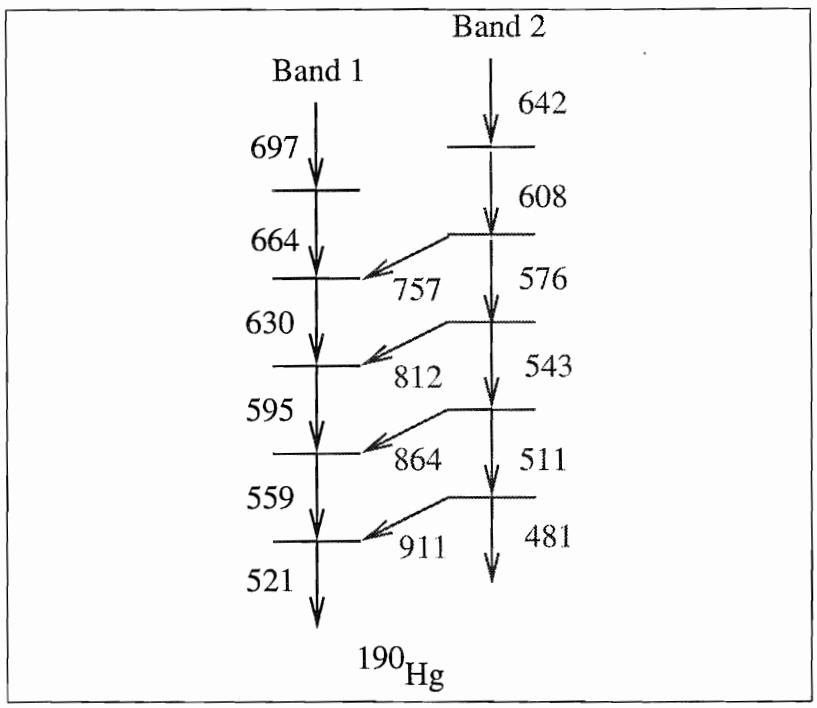

Figure 4.5 Partial level-scheme proposed for the SD states of yrast and the first excited band in ^{190}Hg.

Thus, the unusual properties of this SD band do not quite fit into a quasiparticle scenario. In fact, this band has provided the first experimental evidence for a new excitation scenario (collective vibrations) in the superdeformed well. The suggestion of such an interpretation of band2 was first presented in reference [Cro94,Cro95], where this excited band and the inter-band transitions were first observed. In the following sections more evidences of the octupole vibrational nature of this SD band from the present work will be discussed. Comparison between the experimental results and the Random Phase Ap-

proximation (RPA) calculations will be made to further investigate the configuration of this band.

(1) The Dipole Transition Rates for the Inter-band Transitions

The absolute dipole transition rates for the inter-band transitions derived from the present analysis were reported earlier. These rates are instrumental in ruling out the possibility that the dipole transitions are of $M1$ character. Indeed, if those transitions were magnetic in character, the derived $B(M1)$ strengths, converted to single particle (Weisskopf) units, would be $\sim$ 0.2 W.u. $M1$ transitions of such strength have been observed only between strongly coupled signature-partner bands in odd-A SD nuclei [Joy93]. The mechanism described in reference [Sem92] for strong M1 branches between signature partners cannot apply here since the yrast SD band in ^{190}Hg is presumably a K=0, zero-quasiparticle configuration. Therefore, any excited SD band based on a quasiparticle excitation would be very unlikely to decay to the yrast SD band through M1(configuration-changing) transitions of such large strength. On the other hand, the E1 assignment for the inter-band transitions gains support from the following facts:

1. The B(E1) rates are of the order of 1×10^{-3} W.u., i.e. values much larger than B(E1) rates seen in most deformed nuclei.

2. The B(E1) rates are similar to those reported for E1 inter-band transitions in nuclei with a substantial dipole moment arising from octupole collectivity, as in some of the normally deformed actinide nuclei [But96].

3. In addition, these extracted E1 rates are in good agreement with calculations [Ska93,Bon96] for ^{192}Hg which predict a similar strength for transitions from an octupole vibrational state in the SD well to the zero-phonon yrast SD band (at zero rotational frequency).

4. Further support for the $E1$ assignment to the inter-band transitions comes from the analogy with the situation in ^{194}Hg where E1 inter-band transitions have recently

been observed between band3 and band1 (the spins of band1 and band3 are firmly established)[Hac97].

As a result, the measured B(E1) strengths can be understood as strong evidence in support of the interpretation of band2 as a rotational band built on a one phonon octupole vibrational band head.

(2) The Dynamic Moment of Inertia $J^{(2)}$

Figure 4.4 clearly illustrates that the $J^{(2)}$ moment of band2 is: (i) essentially flat as a function of rotational frequency and (ii) unusually large. The first feature could be attributed to an effect similar to a well known effect observed in the study of octupole bands in the normally deformed well of many nuclei. In those normally deformed nuclei, at moderate spins, the wave-function of the negative parity states are dominated by a small number of two-quasiparticle configurations [Ahm93] even though the microscopic description contains small components of many configurations. If such effect were present in band2 of ^{190}Hg, most of the lowest two-quasiparticle excitations in this nucleus would involve a $j_{15/2}$ quasineutron coupled to a quasineutron occupying one of the positive parity orbitals near the Fermi surface [Dri91]. The occupation of a single $j_{15/2}$ orbital would have the effect of blocking the first rotational alignment of a $j_{15/2}$ neutron pair. Hence, the $J^{(2)}$ moment would be expected to remain constant at least until the first proton alignment occurs or until the alignment of a pair of neutrons in another state than $j_{15/2}$ takes place. In addition, octupole correlations are also predicted to dilute the rotation-aligned character of the quasi-particle orbitals [Dri91]. This effect would result in more constant $J^{(2)}$ values as a function of rotational frequency.

Two possible interpretations of the origin of the unusual large moment of band2 should be considered: either (1) SD band2 has an unusually large quadrupole moment Q_0 (i.e. large deformation) compared to the yrast SD band, or (2) the high $J^{(2)}$ moment arises from Coriolis mixing among different octupole vibrational bands. The first possibility can be ruled out since it is established from the results of the present work that band1 and band2 have the same quadrupole moments (the difference in the quadrupole

moment between band1 and band2, δQ_0, is 0.1±1.9 *eb*). In fact, if the difference in the dynamic moment of inertia between band1 and band2, $\delta J^{(2)}$, was simply due to a difference in deformation, then at $\hbar\omega \simeq 0.28$ MeV (where $\delta J^{(2)} \simeq 15\hbar^2/\text{MeV}$) the expected difference in the quadrupole moment would be $\delta Q_0 > 5$ *eb*. Clearly, such a difference is well outside the limits from the present work. This result is consistent with the assumption of equal deformation used in the RPA calculations [Nak96]. On the other hand, a generator-coordinate method calculation (GCM) of the octupole correlations in superdeformed ^{192,194}Hg and ^{194}Pb nuclei predict that in these nuclei the quadrupole moment for the excited SD band is about 15% larger than that of the respective yrast SD bands due to the coupling between the octupole and quadrupole degrees of freedom [Ska93,Mey95]. Again, this interpretation can be ruled out on the basis of the data presented in this work. Thus, the excitation corresponding to band2 is not associated with a permanent octupole deformation (which also drives the nucleus towards a large quadrupole deformation), but rather to a vibration for which the equilibrium deformation remains the same as that of the superdeformed ground state (i.e. that associated with the yrast band).

The last point made above is reemphasized by the comparison between the measured $J^{(2)}$ values and the values obtained in the RPA calculations for the lowest octupole vibrational mode (K=2, α=1) (Figure 4.6). It is clear that the characteristic features of band2 are well reproduced in the RPA calculations, particularly, when pairing is allowed to reduce dynamically with increasing $\hbar\omega$. This comparison supports the interpretation of band2 as a rotational band built on the K=2, α=1 one phonon octupole vibrational state [Nak96], although there is considerable mixing with other low-lying octupole excitations in the region of frequency where band2 is experimentally observed [Cro95,Wil96].

4.4.3 The Second Excited SD Band in ^{190}Hg

This excited SD band, band3, has been observed recently, and detailed information on transition energies and relative intensities is presented in reference [Wil96]. RPA calculations attempting to reproduce the properties of this band can be found in reference [Nak96]. The comparison between the data and the RPA calculations will be made in

order to investigate the configuration associated with this SD band. The evolution of the $J^{(2)}$ moment with $\hbar\omega$ along with results from RPA calculations are illustrated in Figure 4.6.

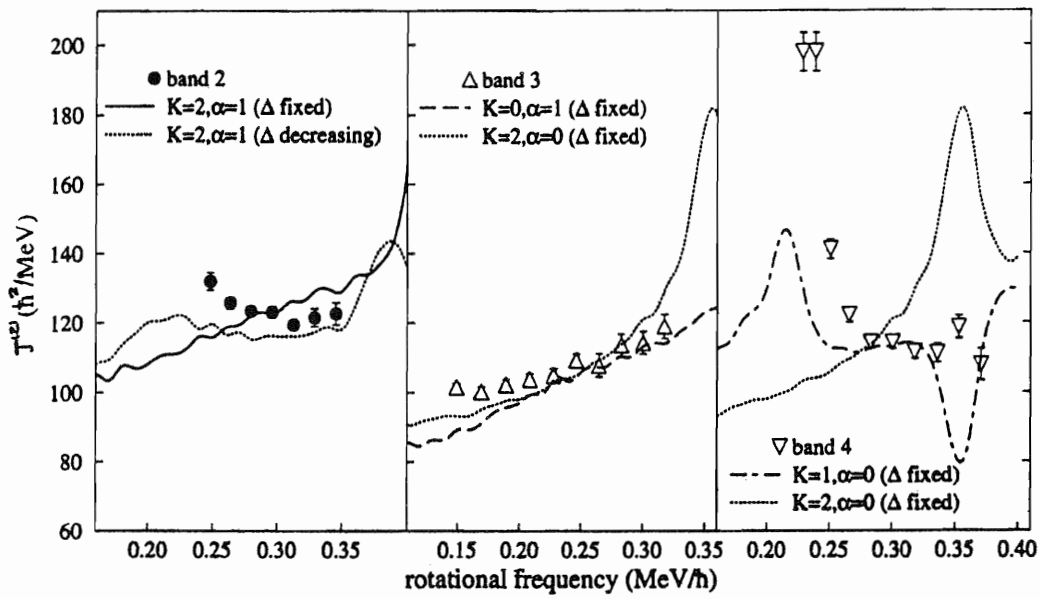

Figure 4.6 Comparison between the observed evolution of the $J^{(2)}$ moment with $\hbar\omega$ with that reproduced in the RPA calculations for the excited SD bands in ^{190}Hg. The observed values are • for band2 (left), △ for band3 (middle), and ▽ for band4 (right). Figure taken from reference [Wil96].

It is clear from Figure 4.6 that, over most of the frequency range in which band3 is observed, a reasonable agreement between the observed evolution of the $J^{(2)}$ moment and the results of the RPA calculations (with fixed pair gaps) is achieved. As a result of this comparison, two possible collective configurations for band3 can be considered. First, band3 could be interpreted as a rotational band built on the second excited octupole state K=2, α=0. This possibility implies that this band is the signature partner of band2 since the K=2, α=0 state is predicted by the RPA calculations to be the next available excitation above the K=2, α=1 state as shown in Figure 4.3. If this configuration is true, then one would expect the following consequences: (1) as signature partner, the intensity

of band3 should be similar to that of band2, and (2) no other SD band should have an absolute intensity in between those of band2 and band3. However, experimentally a large difference in the intensities of band2 and band3 was observed (the signature splitting between the two K=2 modes is not sufficient to explain this difference). In addition, the intensity of the third excited band (band4) is found to be closer to that of band2 than the intensity of band3. Hence, these difficulties make it less likely that band3 is the K=2, α=0 band. The second possible configuration would associate band3 with the K=0, α=1 octupole state. This mode was ruled out since it was predicted (by the RPA calculations) to have a strong decay branch to the yrast SD band and no experimental evidence was found for such a decay [Wil96].

The previous discussion might suggest that this band is associated with a quasiparticle excitation and does not involve octupole correlations at all. It is possible that the lowest positive-parity, two-quasiparticle excitations are populated at lower excitation energies than the lowest negative-parity one-phonon vibrational states (remember that Figure 4.6 shows only the lowest negative-parity states in ^{190}Hg and there will be no positive-parity one-phonon octupole vibrational states). The $J^{(2)}$ moment for a SD band with such a quasiparticle configuration should evolve with $\hbar\omega$ in a manner similar to that of the $J^{(2)}$ moment of the yrast SD band. This similarity is clearly illustrated in Figure 4.6; however, there are some minor differences. At low frequency (i.e. $\hbar\omega \leq$0.35 MeV), the $J^{(2)}$ moment has a slightly larger magnitude, with a flatter slope compared to that of the yrast SD band. For higher frequencies (i.e. $\hbar\omega \geq$0.35 Mev) this band has not been observed yet. Therefore, it is not possible to conclude whether a band crossing similar to that of band1 (this crossing is responsible for the sharp rise in the $J^{(2)}$ moment in band1) occurs. In view of all these observations, no definite conclusion regarding the configuration associated with this band can be made [Wil96].

4.4.4 The Third Excited SD Band in ^{190}Hg

Once again, a comparison between the observed evolution of the $J^{(2)}$ moment with $\hbar\omega$ and that obtained in the RPA calculations will be employed to examine the configuration

associated with this SD band (band4). This comparison is illustrated in Figure 4.6. One can clearly see from this figure that the observed evolution of the $J^{(2)}$ moment of band4 is different from that observed in other SD bands in even-even SD Hg isotopes. At frequencies $0.25 \leq \hbar\omega \leq 0.4$ MeV, the $J^{(2)}$ moment is essentially constant, similar to that observed in band2, while at the lowest frequencies, i.e. $\hbar\omega \leq 0.23$ MeV, a sharp rise occurs (similar to that observed in band1 at the highest frequencies) suggesting a sudden change in alignment due to a band crossing.

The RPA calculations, performed with fixed pairing gaps (Δ_n=0.8 MeV and Δ_p=0.6 MeV), predict that a band crossing will occur at frequencies around $\hbar\omega$ =0.23 MeV. At frequencies $\hbar\omega \leq 0.23$ MeV, the RPA calculations predict that band4 is based on the K=1, α=0 vibrational mode. While at frequencies $\hbar\omega \geq 0.23$ MeV, the RPA calculations predict that band4 is a two-quasineutron band involving the occupation of the favored N=7 and the unfavored N=6 neutron orbitals. For such a configuration, in which only one of the pair of N=7 orbitals is occupied, the alignment of these orbitals is blocked [Ril90] and, thus, one would expect the associated $J^{(2)}$ moment to be relatively constant with $\hbar\omega$ (similar to that of band2). The observed evolution of the $J^{(2)}$ moment and RPA calculations for band4 are in good agreement, as clearly illustrated in Figure 4.6 (where the $J^{(2)}$ moments are calculated for the vibrational mode K=1, α=0 and the K=2, α=0 at $\hbar\omega$=0). It can also be seen that the interaction between the K=1 state and the two-quasineutron state is slightly stronger than the observed one [Wil96].

Another possible configuration must be considered, despite the fact that RPA calculations (with fixed pairing gaps) reproduce the $J^{(2)}$ moment evolution with $\hbar\omega$ fairly well. If the pairing gaps in the RPA calculations are allowed to reduced dynamically with increasing $\hbar\omega$, all band crossings are lowered. The crossing between the two-quasineutron band and the K=2, α=0 vibrational mode will occur at $\hbar\omega \sim 0.28$ MeV. This interaction is weaker than that involving the K=1, α=0 state and thus a sharper rise in the $J^{(2)}$ moment will occur. Therefore, band4 might be the signature partner of band2.

Finally, if band4 corresponds to a collective vibrational state at low frequencies, one might expect transitions linking this band to the yrast SD band (as in the case of band2).

The experimental evidence for the existence of such transitions is very weak [WIL96]; however, RPA calculations for the K=2, α=0 band predict that these linking transitions should be much weaker than those seen in the case of band2. Hence, it seems that the behavior of band4 is consistent with it being built on either a K=1, α=0 or K=2, α=0 vibrational state at low frequencies. While at higher frequencies band4 is built on a two-quasineutron excitation involving the occupation of the unfavored (positive) signature of the N=6 neutron orbital and the favored (negative) signature of the N=7 neutron orbital [Wil96].

4.5 Conclusions

The results of the present work have now cleared the ambiguity surrounding the configuration associated with the first excited SD band (band2) in ^{190}Hg. The measured $B(E1)$ strengths of the transitions linking this band to the yrast SD states are consistent with the interpretation of band2 as an octupole collective excitation. In addition, the measured quadrupole moments of band2 and of the yrast SD band establish that no difference in deformation exists between both bands, reinforcing an interpretation where octupole correlations in the second minimum are responsible for the unusual behavior of the $J^{(2)}$ moment of band2, and for the unusual decay pattern into band 1. The RPA calculations of Nakatsukasa et al. reproduce the properties of band2 very well. They also provide an understanding of the properties of the other excited SD bands in this nucleus. Within this framework, band 2 is associated with the K=2, α=1 octupole vibration.

The present results, while important for the understanding of superdeformation in ^{190}Hg and, by extension, in all the A $\sim$ 190 nuclei, do not necessarily answer all the important issues: there is room for additional work. On the experimental side, measuring the polarization of the inter-band transitions to confirm their electric (E) character is desirable. Searching for the other ^{190}Hg excited SD bands predicted by the RPA calculations would put the interpretation on an even firmer ground. On the theory side, the RPA calculations of Nakatsukasa et al. remain rather schematic. The wave functions that were used are those calculated with a Nilsson potential known to be deficient (the SD shell

gaps are not reproduced well with the potential), and the theory still contains a number of parameters which are adjusted to the data and not computed from first principles as would be desirable.

Part III

Search for the Two-Phonon Octupole Vibrational States in ^{208}Pb

Introduction

The search for the double-octupole phonon vibrations in the doubly-magic nucleus ^{208}Pb remains a fascinating and unresolved problem in contemporary nuclear structure physics. The search for the members of this excitation is motivated mainly by the fact that their observation provides a direct measurement of the degree of harmonicity of octupole vibrations.

The lowest excited state in the doubly-magic ^{208}Pb nucleus has spin I and parity π quantum numbers $I^{\pi} = 3^{-}$. This level has been associated with a one-phonon vibration of octupole character. This interpretation is based mostly on the following experimental facts: (i) the excitation energy of 2614 keV is lower than what is expected for any particle-hole excitation; since ^{208}Pb is a doubly magic nucleus, the proton and neutron shell gaps are indeed quite large (Δ=3.44, 4.18 MeV for protons and neutrons, respectively), and (ii) the fact that the transition probability $B(E3, 3^{-} \rightarrow 0^{+})$ for this state is large when compared with single-particle estimates; $B(E3, 3^{-} \rightarrow 0^{+})$=34 *W.u* (Weisskopf units).

In fact, examples of one-phonon octupole excitations are found in the form of a low-lying 3^{-} state in all the closed shell nuclei from ^{16}O (with the highest excitation energy of 8.13 MeV) to ^{208}Pb (with the lowest excitation energy of 2.614 MeV). The existence of a two-phonon octupole vibrations is then naturally expected to occur at about twice the excitation energy of the one-phonon state (i.e. at about 5.2 MeV in ^{208}Pb). Among all the doubly magic nuclei, the ^{208}Pb is the most interesting candidate for the search of the 2-phonon octupole excitations, since it is in this nucleus that the excitation energy is the lowest. Thus, the double-phonon octupole state will lie in a region where the level density is still fairly low. Therefore, the coupling or interaction of members of the 2-phonon multiplet with other levels would be expected to be small and rather pure (i.e. unperturbed) excitations are most likely.

Theoretical calculations and experimental observations (which will be discussed later) predict a deviation of the 2-phonon octupole excitations in the ^{208}Pb from the pure harmonic picture. This departure from pure harmonicity can be viewed in light of the expected splitting of the 2-phonon octupole into a quartet of states; (i.e. $3^{-} \otimes 3^{-}$:$0^{+}, 2^{+}, 4^{+}$ and

6^+), which consequently, shifts the excitation energies of members of the multiplet away from the expected excitation energy of the 2-phonon octupole (i.e. ~5.2 MeV).

In principle, the following signatures should be expected for a two-phonon octupole excitation; (i) the excitation energies involved are about twice that of the one-phonon state (i.e. ~5.2 MeV ^{208}Pb), (ii) for the 0^+ and 6^+ members of 2-phonon multiplet, a cascade of two $E3$ transitions corresponding to the 0^+ or $6^+ \rightarrow 3^- \rightarrow 0^+$ decays should be seen, (iii) enhanced $E1$ transition(s) corresponding to the 2^+, $4^+ \rightarrow 3^-$ or 6^+, $4^+ \rightarrow 5^-$ decays (the 5^- level is the second excited state in ^{208}Pb at 3197 keV) should be present as well, and finally (iiii) state lifetimes τ of the order of few *ps* should be measured (theory predicts τ ~8 *ps* assuming that the state decays via an $E3$ transition, in the event of an $E1$ transition τ might be shorter). It should be mentioned that the measured lifetime of the one-phonon state in ^{208}Pb is about 17 *ps*.

While many examples of multi-phonon excitations are known, the expected "pure" two-phonon octupole vibrational states in doubly-magic nuclei have yet to be unambiguously identified. Multi-phonon excitations such as 2-phonon quadrupole vibrational states in even-even nuclei such as the cadmium (Cd) [Apr87] and tin (Sn) nuclei are well documented. In these nuclei, the first excited state is a 2^+ level and at roughly twice the excitation energy there is often a triplet of levels with $I^\pi = 0^+, 2^+$ and 4^+. Such behavior is typical of nuclei excited by one- and two-phonon quadrupole vibrations. Two-phonon γ-vibrations, in which a section of the nucleus in the xy-plane is an ellipse at any instant of time, are another known type of multi-phonon excitations in rare earth nuclei such as ^{166}Er [Fah96]. Two-phonon β-vibrations have been reported as well. The 0_4^+ state in ^{166}Er is proposed to be a member of a two-phonon β-vibrational multiplet, based on the the enhanced transition probability $B(E2; 0_4^+ \rightarrow 2_{gsb}^+)$ and its population in two-neutron transfer [Gar97]. This assignment, however, is not without controversy [Bur94]. Furthermore, the 2-phonon octupole vibrations may also couple to other modes of excitation such as particle excitations resulting in more complex states of the 2-phonon type. This is expected in nuclei with a number of valence nucleons. Example of such excitations have been proposed in the ^{144}Nd, ^{146}Sm [Bar95], ^{147}Gd [Kle82], and ^{148}Gd [Lun84, Pii93] nuclei.

For many years, the search for the expected "pure" two-phonon states in the doubly-magic nucleus ^{208}Pb went on using many experimental techniques [Mar83, Chr77], but in spite of those many attempts it was not possible to unambiguously identify members of the 2-phonon multiplet. The interest in the search for such excitations has been recently renewed by the results of a new measurement [Wol92] that also motivated the work described in the present thesis. This measurement was carried out at the "Gesellshaft fur Schwere Ionen Forschung" (GSI) by Wollersheim *et al.* [Wol92]. These authors reported evidence for the excitation of the 6^+ state of the double-octupole phonon multiplet from a Coulomb excitation experiment performed at energies 20% above the Coulomb barrier in the ^{208}Pb+ ^{208}Pb system. Indeed, it was proposed that a state located at an excitation energy of 5.683 MeV, and deexciting via a 2485 keV gamma ray towards the 5^- level, should be associated with the decay of the 6^+ member of the double octupole phonon multiplet, although a 4^+ assignment could not be entirely ruled out. The result of ref. [Wol92] was not without controversy: just as soon as it appeared in press, it was questioned because of the results of reference [Sch92] where a 2485 keV γ ray was also seen (in experiments with ^{64}Ni and ^{82}Se beams on a ^{208}Pb target at energies above the Coulomb barrier), but was assigned to a state in ^{207}Pb fed through a one-neutron transfer reaction. At this point in time, not completely ruling out the GSI results, it was decided to renew the search for members of the 2-phonon octupole multiplet in ^{208}Pb and to investigate further the placement of the 2485 keV γ ray.

A set of three experiments was carried out to address the issue. First, a modified version of the GSI measurement was repeated at the ATLAS accelerator at the Argonne National Laboratory, where thick ^{208}Pb and ^{209}Bi targets were bombarded with ^{208}Pb beams at energies roughly 20% above the Coulomb barrier. The analysis of the data showed conclusively that the results by Wollersheim *et al.* were in error and confirmed the placement of the 2845 keV transition in ^{207}Pb. In addition, the analysis (described in much detail hereafter) searched for any transition which could become a candidate for the deexcitation of a member of the double octupole multiplet. While no clear signal could be found, the presence of a number of weak, broad structures was deemed to be sufficiently

encouraging to propose a set of two experiments with the best gamma-ray spectrometer available: Gammasphere.

The first of the two Gammasphere experiments constitutes the central piece of this work. Using a ^{136}Xe beam on a thick ^{208}Pb target, at energies above the Coulomb barrier, a careful search for the γ rays associated with the deexcitation of the multiplet members was carried out. Once again, no signal could be found and the results were expressed in terms of upper limits on the probability of populating the levels of interest. These limits depend on the lifetimes of the double phonon states. Clearly, if these lifetimes were much shorter than anticipated, the gamma rays would undergo severe Doppler broadenings and/or shifts in the thick target and their observation would be severely hampered. The second Gammasphere experiment addressed this issue by using a thin target and detecting the beam-like and the target-like reaction products with position-sensitive, gas counters. This second measurement also addressed another concern. The choice of beam energies above the Coulomb barrier was motivated by the desire to enhance the cross sections for the production of the states of interest by taking advantage of the large contribution of nuclear excitations (in addition to the electromagnetic excitations) to the reaction mechanism. By performing the second measurement with the ^{136}Xe beam at energies well below the Coulomb barrier, a reaction regime was explored where only the well understood electromagnetic interaction contributes significantly. This experiment is discussed more briefly in this thesis because its analysis was performed mostly by members of the collaboration from the Lawrence Berkeley National Laboratory. Again, no clear signal was found and only upper limits were deduced [Vet98].

Finally, it should be noted that, while the present work was being carried out, another experimental approach was used by a group at the University of Kentucky to propose candidates for the 0^+, 2^+ and 4^+ double octupole phonon states. Using $(n, n'\gamma)$ reactions, Yeh *et al.* [Yeh96, Yeh98] observed candidate γ rays corresponding to decays from states with energies close to theoretical expectations for 2-phonon multiplet. These results will be reviewed in detail hereafter and their significance will be discussed in the context of the present negative results.

Chapter 5

Data Analysis and Results

An extensive search for the two-phonon octupole vibrational states of ^{208}Pb was undertaken in a series of Coulomb excitation experiments. In this chapter, results from this search will be presented and limits on the cross sections for the population of the two-phonon octupole vibrational members will be discussed.

5.1 Experimental conditions

Three different measurements were conducted in order to search for the two-phonon octupole vibrational states of ^{208}Pb. The first was conducted at ANL while the second and third were conducted at LBNL. The data analysis from the first two experiments was performed at ANL while the data analysis from the third measurement is still continuing by our collaborators at LBNL. In the following few sections, a brief description of the experimental conditions of all three measurements will be presented.

5.1.1 The Experiments at ANL

Excited states in ^{208}Pb were populated in the following reactions:

(1) ^{208}Pb(^{208}Pb,^{208}Pb$'$)^{208}Pb

(2) ^{209}Bi(^{208}Pb,^{208}Pb$'$)^{209}Bi

In these two measurements a 1305 MeV, ^{208}Pb beam was provided by the ATLAS accel-

erator facility at Argonne National Laboratory (ANL). The choice of this beam energy was motivated by the desire to reproduce the conditions of the GSI experiment of reference [Wol92] where a candidate for the 6^+ double octupole state had been reported. Thick targets ($\sim$ 50 mg/cm^2) of ^{208}Pb and ^{209}Bi were used and γ rays were detected using the Argonne-Notre Dame BGO γ-ray facility, consisting of 12 Compton-suppressed Ge-detectors surrounding an array of 50 BGO scintillators. The events of interest were selected using several triggers, including $\gamma - \gamma$, γ-BGO, and $\gamma - \gamma$-BGO coincidences. Both prompt and delayed coincidence events were recorded. A total of about 30×10^6 $\gamma - \gamma$ coincidence events were available for analysis in the ^{208}Pb target data set, while the corresponding number for the ^{209}Bi target data set is 13×10^6 .

5.1.2 The Experiments at LBNL

Excited states in ^{208}Pb were populated in the reaction ^{208}Pb(^{136}Xe,^{136}Xe$'$)^{208}Pb. Two different measurements were performed one with a thick target and the other with a thin target.

(a) The thick target measurement:

The experiment was performed with a thick ^{208}Pb target ($\sim$ 50 mg/cm^2) bombarded by a 884 MeV (i.e. 6.5 MeV/A) ^{136}Xe beam, provided by the 88" cyclotron of Lawrence Berkeley National Laboratory (LBNL). PTOLEMY calculations have been performed prior to this measurement to decide which beam energy maximizes the production cross section of the 2-phonon members, details of these calculations will be presented in a following section. The γ rays were detected by Gammasphere consisting, at that time, of 93 Compton-suppressed Ge-detectors. Two-, three- and higher-fold prompt coincidence events were recorded. About 3.6×10^9 prompt $\gamma - \gamma - \gamma$ events were collected.

(b) The thin target measurement:

The experiment was performed with a thin ^{208}Pb target ($\sim$ 0.9 mg/cm^2) bombarded by a beam of ^{136}Xe, provided by the 88" cyclotron of LBNL, at a 650 MeV (7% below the

Coulomb barrier of the $^{136}Xe + {}^{208}Pb$ system). The γ rays were detected by Gammasphere consisting again of 93 Compton-suppressed Ge-detectors. The two dimensional position sensitive parallel plate avalanche counter CHICO [Sim98] was used to select binary collisions, to correct for Doppler-shift of the γ-rays emitted in-flight and to determine excitation probabilities as a function of the scattering angle. The mass resolution of CHICO ($\sim$ 10%) allowed for the unique identification of the projectile-like and the target-like reaction products for the forward angle scattering. About 8.5×10^7 $particle - particle - \gamma - \gamma$ events were collected.

5.1.3 PTOLEMY Calculations

Coupled channel calculations have been performed using the code PTOLEMY [Rho80] which takes into account Coulomb and nuclear interactions in order to find the beam energy that yields the highest production cross section for the two-phonon octupole vibrational members. The calculations were carried out under the assumption that the 2-phonon multiplet is located at an excitation energy of 5.2 MeV. It is clearly illustrated in Figure 5.1 that beam energies of $\sim$ 707-843 MeV (this corresponds to a center of mass energy range which is $\sim$ 20% larger than the Coulomb barrier of the $^{136}Xe+{}^{208}Pb$ system) are probably the best beam energies one can use to populate the 2-phonon multiplet members. Figure 5.2 shows the calculated angular distributions of the differential cross section for the two-phonon octupole members. It is clear that only the 6^+ member of the multiplet receives an appreciable contribution from Coulomb excitation. Nuclear excitation plays the dominant role, giving rise to fairly large cross sections of the order of millibarns, which are peaked at about 80°. Those results are in agreement with those presented in reference [Lan77] where coupled channel calculations were performed to study the excitation of the double octupole phonon states in ^{208}Pb using a beam of ^{136}Xe ions at an energy 20% above the Coulomb barrier. It is clear from such calculations that the choice of 884 MeV ^{136}Xe beam was made to optimize the population of the double octupole phonon states over as much as possible of the thick ^{208}Pb target.

5.2 Data Analysis of the ANL Measurements

The primary goal of sorting the ^{208}Pb and the ^{209}Bi target data sets (i.e. the search for the two-phonon octupole vibrational states in ^{208}Pb) is best achieved by being able to create coincidence spectra gated on known transitions in ^{208}Pb, in particular on the $3^- \rightarrow 0^+$ and $5^- \rightarrow 3^-$ transitions which are believed to be the only ones with which the γ rays deexciting the two-phonon octupole vibrational states will be in coincidence. More details on the analysis will be given in the following sections.

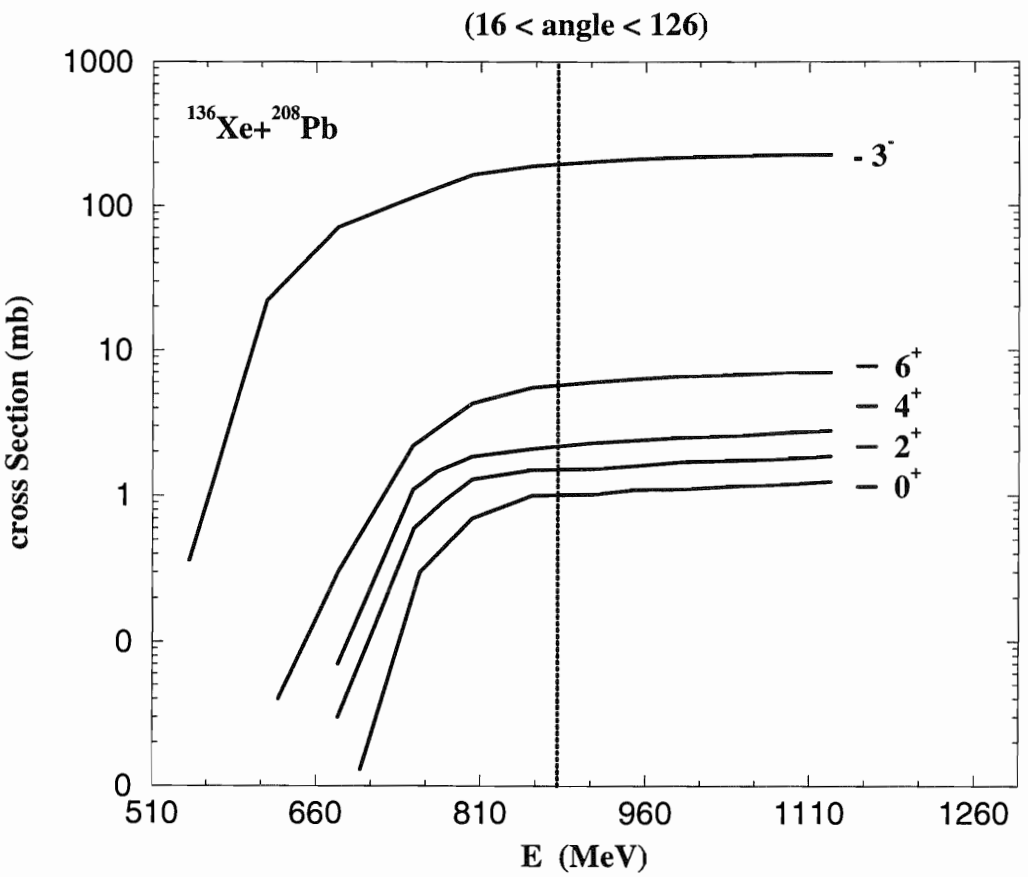

Figure 5.1 Results from PTOLEMY calculations for the total cross section of the one-phonon (3^-) and the two-phonon (6^+, 4^+, 2^+, and 0^+) states in ^{208}Pb as a function of beam energy.

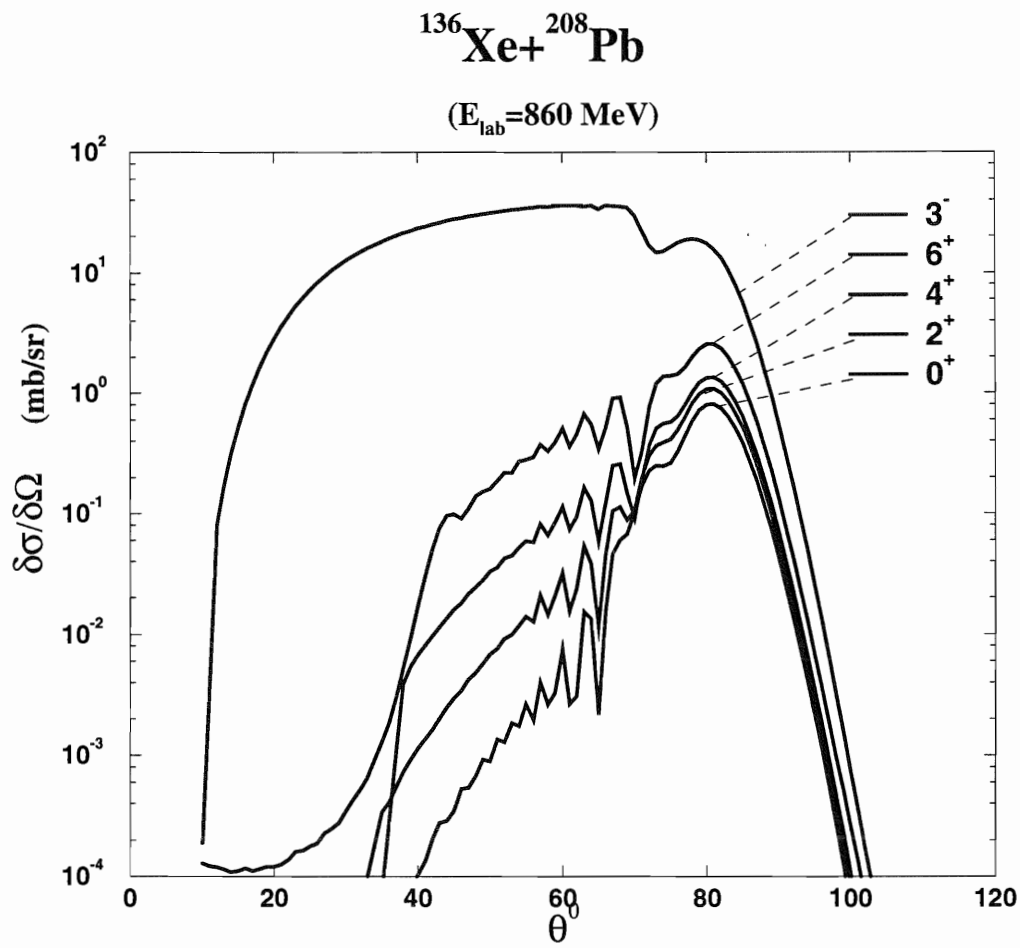

Figure 5.2 Calculated angular distributions for the one- and two-phonon octupole states in ^{208}Pb.

5.2.1 Constructing Prompt $\gamma - \gamma$ Coincidence Matrices

Prompt $\gamma - \gamma$ coincidence matrices were constructed from both data sets (obtained with the ^{208}Pb and the ^{209}Bi targets). The total projection of the prompt $\gamma - \gamma$ coincidence matrix for the ^{208}Pb target is presented in Figure 5.3. It shows all the γ rays produced in the ^{208}Pb+^{208}Pb collisions as detected in all the Ge detectors of the Argonne-Notre Dame BGO γ-ray facility. The following steps were essential in order to search for the two-phonons octupole vibrational states in ^{208}Pb:

(1) Identification of Coincident γ Rays Produced in the Data

It is clearly illustrated in Figure 5.3 that a large number of γ rays are present in the coincidence matrix. These γ rays need to be understood (i.e. placed in their respective nuclei) in as much as possible if one wants to identify new γ rays and possibly assign them to the deexcitation of a double octupole phonon level. From the measured coincidence relationships deduced from the careful inspection of gated spectra, almost all the γ rays could be assigned to a specific nucleus. In principle, one can identify coincident γ rays from the ^{208}Pb target data set only, but, since the beam energy used is $\sim 20\%$ larger than the Coulomb barrier for the Pb+Pb system, an appreciable number of γ rays produced in this data set involves reaction processes other than Coulomb excitation such as transfer-evaporation or direct transfer reactions. Evidence for such processes is present in the data. For example, as illustrated in Figure 5.4, γ rays belonging to ^{206}Pb and ^{210}Pb are found to be in coincidence with each other: this corresponds to a two-neutron direct transfer reaction. Table 5.2.1 summarizes all the multi-nucleon transfer processes extracted from the data and lists the measured relative intensities of all the γ rays produced in such reactions (intensities are measured relative to the ground state transition in the respective nucleus). Partial level schemes for all the nuclei produced in the data were also constructed. Figure 5.5 presents an example of the partial level schemes constructed for nuclei formed in the two-neutron direct reaction channel (i.e. for ^{206}Pb and ^{210}Pb nuclei). The ^{209}Bi target data set is then used to double check the coincidence relationships and to confirm the placement of the γ rays in their corresponding nuclei.

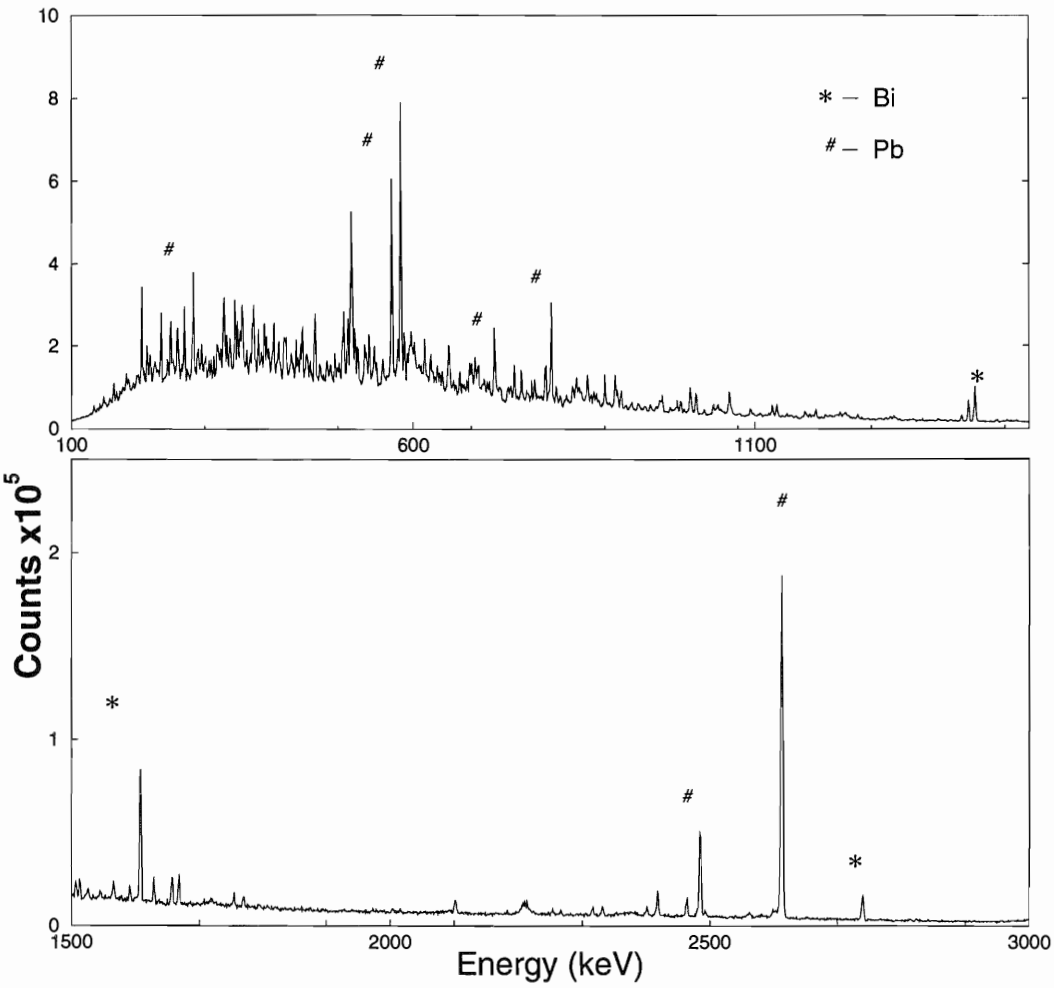

Figure 5.3 The total projection of the prompt $\gamma - \gamma$ coincidence matrix in the ^{208}Pb target data set. The symbol ♯ marks some of the sharp, strong transitions in the Pb nuclei. On the other hand, the symbol $*$ marks some of the sharp strong transitions in ^{209}Bi nucleus. No background subtraction is applied to this spectrum.

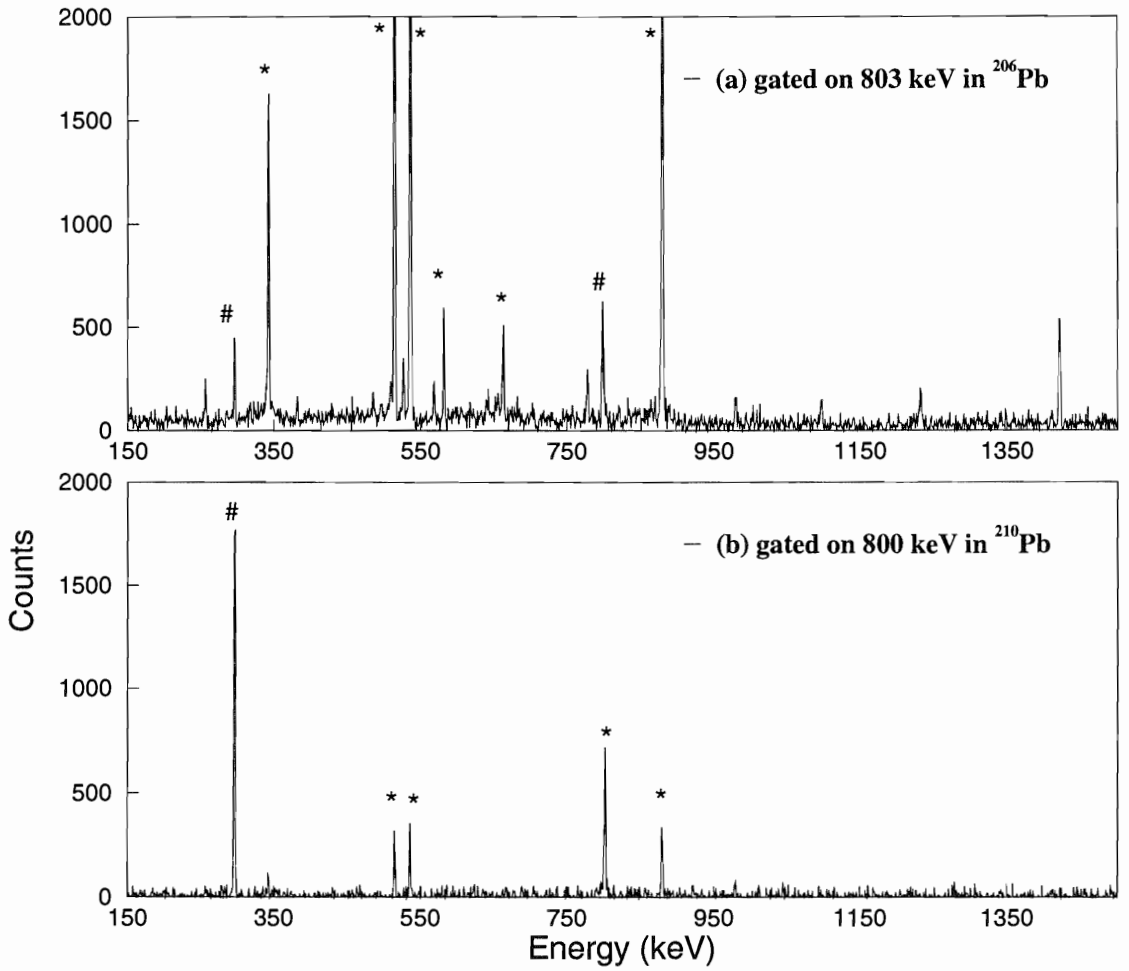

Figure 5.4 (a) is the coincidence spectrum gated on the ground state transition in ^{206}Pb while (b) is the coincidence spectrum gated on the ground state transition in ^{210}Pb. The symbol $*$ marks γ rays belonging to ^{206}Pb and the # label refers to those belonging to ^{210}Pb. The fact that γ rays in both nuclei are in coincidence with each other is clearly visible and indicates that the spectra correspond to a two-neutron transfer mechanism.

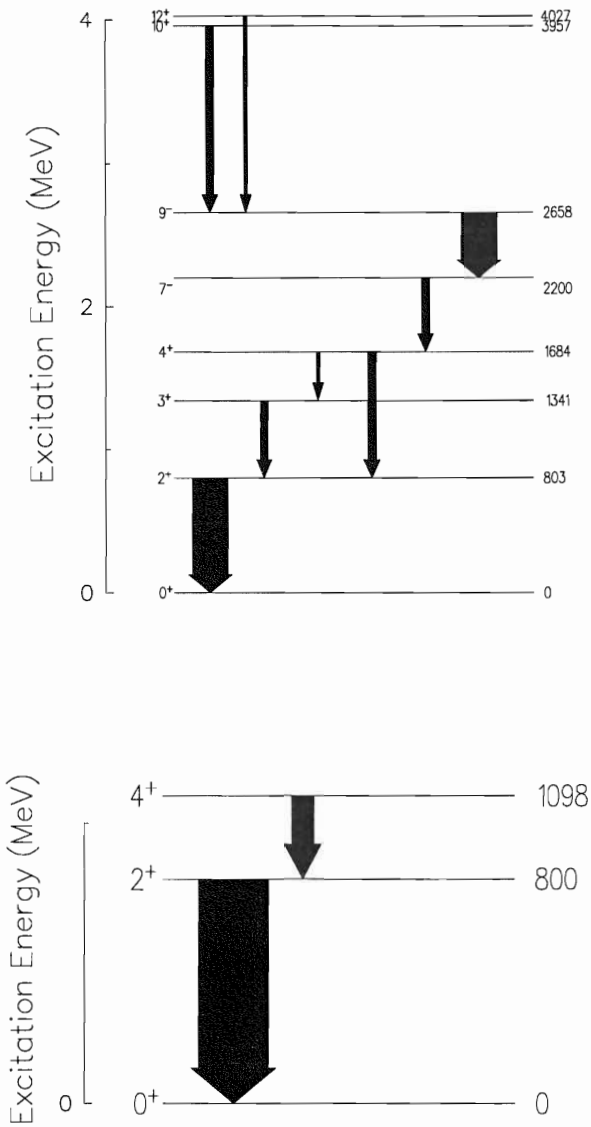

Figure 5.5 Partial decay schemes in ^{206}Pb (top) and ^{210}Pb showing transitions observed in coincidence in the present measurements. The width of the arrows are proportional to the measured intensities of γ rays normalized to the ground state transition of the respective nuclei. Similar level schemes were obtained for all reaction processes under investigation.

Table 5.1 A list of the nuclei produced in all channels in the data with the measured relative intensities of the observed γ rays belonging to those nuclei. The intensities are normalized to the intensity of the ground state transition in the respective nucleus. The assignment of those γ rays has been verified from coincidence relationships in data sets with both the ^{208}Pb and ^{209}Bi targets.

Channel	Nucleus	E_γ (keV)	Relative intensity
^{208}Pb+1n	^{209}Pb	465	5.9±0.68
		644	8.8±0.95
		779	26.8±1.86
		1422	63.4±4.10
		1566	9.8±0.79
^{208}Pb-1n	^{207}Pb	1064	12.21±1.14
		750	37.12±5.1
		384	22.99±2.5
		793	11.49±1.29
		626	14.93±1.66
		324	13.66±1.54
		593	24.37±2.65
		570	100.0±7.5
		2485	100.0±5.6

Channel	Nucleus	E_γ (keV)	Relative intensity
^{208}Pb-2n	^{206}Pb	343	9.55±0.95
		537	20.99±2.03
		881	25.11±2.44
		516	22.95±2.23
		485	100.0±5.19
		803	100.0±5.99
		1299	10.89±1.71
		1369	22.90±2.7
		899	100±9.3
^{208}Pb+2n	^{210}Pb	296	32.26±11.2
		799	100.0±7.41

Channel	Nucleus	E_γ (keV)	Relative intensity
^{208}Pb-3n	^{205}Pb	1147	52.25±13.25
		284	
		684	
		324	
		703	100±16.6
^{208}Pb-4n	^{204}Pb	376	103±13.97
		899	100±9.3

Channel	Nucleus	E_γ (keV)	Relative intensity
^{208}Pb+2p	^{210}Po	1181	100.0±10.0
		1599	8.4±1.5
		1484	9.5±1.7
		245	106.0±15.0
^{208}Pb+2p-1n	^{209}Po	545	100.0±8.7
		782	35.0±9.1
^{208}Pb-2p-2n	^{204}Hg	437	100.0±9.0
		1063	38.0±6.0
		692	102.0±28.0
^{208}Pb-2p-6n	^{200}Hg	368	100.0±8.1
		579	36.9±6.0
		795	37.5±5.6
		498	18.5±2.8
		181	21.1±3.2
		256	35.5±5.1

Channel	Nucleus	E_γ (keV)	Relative intensity
^{208}Pb-1p	^{207}Tl	351	100.0±6.0
		799	2.4±0.3
^{208}Pb-1p-1n	^{206}Tl	216	100.0±17.4
		266	100±7.5
		686	63.0±8.0
		536	10.0±1.4
		453	40.0±4.7
		604	6.1±1.0
		1140	2.4±0.4
		369	7.9±1.1
		457	89.4±23.5
		1022	37.5±9.5

Channel	Nucleus	E_γ (keV)	Relative intensity
^{208}Pb-1p-2n	^{205}Tl	204	100.0±13.0
		739	8.4±1.4
		810	10.4±1.7
		157	9.0±1.7
		340	17.6±3.0
		570	38.0±6.0
		506	41.0±7.0
		720	67.0±11.0
		416	14.0±2.3

Channel	Nucleus	E_γ (keV)	Relative intensity
^{208}Pb-1p-4n	^{203}Tl	279	100.0±11.0
		905	32.6±4.8
		795	72.2±10.0
		232	71.5±11.0
		588	66.8±9.0
		143	62.5±9.0
		537	6.8±1.0
^{208}Pb+1p-1n	^{208}Bi	511	100.0±1.4
		921	7.4±1.3
^{208}Pb+1p	^{209}Bi	896	41.7±4.1
		922	25.9±2.7
		1132	30.0±3.1
		246	31.7±2.9
		500	12.5±1.5
		2741	11.0±1.2
		1608	47.3±4.6

(2) Placement of the 2485 keV γ Ray

In an experiment to search for the two-phonon members in ^{208}Pb at GSI, a thin ^{208}Pb target was bombarded by a ^{208}Pb beam at an energy about 10% above the Coulomb barrier. A 2485 keV γ ray was observed to be in coincidence with the $5^- \rightarrow 3^-$ and $3^- \rightarrow 0^+$ transitions in ^{208}Pb and was attributed to the depopulation of one of the two-phonon members [Wol92]. In a subsequent experiment performed at HMI, targets of ^{208}Pb were bombarded with ^{64}Ni and ^{82}Se beams. The 2485 keV transition was observed in these measurements as well. However, this γ ray was not assigned to ^{208}Pb [Sch92] instead it was assigned to ^{207}Pb and attributed to the decay of states populated in single-neutron transfer reactions. This assignment was based on the following arguments: (i) coincidence relationships with transitions in both the ^{64}Ni and ^{82}Se nuclei (i.e. a prompt coincidence spectra gated on the 2485 keV transition from both beams data sets shows no trace of either the 583 keV or 2614 keV transitions in ^{208}Pb nucleus) suggested that this transition does not belong to the ^{208}Pb nucleus. (ii) From intensity considerations, the 2485 keV transition has to populate a ground state or an isomer. From the ^{64}Ni beam data set, the prompt 2485 keV line was found to be in coincidence with the 1017 keV isomer in ^{65}Ni as well as with known transitions of both ^{207}Pb and ^{206}Pb nuclei. This was suggestive that the 2485 keV line belongs to either ^{207}Pb (1n direct transfer) or ^{206}Pb (2n transfer followed by 1n evaporation). However, if the 2485 keV line is in the ^{206}Pb nucleus, it should be known already (this nucleus is very well studied). On the other hand, calculations predicted an isomeric state in the ^{207}Pb nucleus with an energy of 4118 keV, feeding the known 570 keV level in ^{207}Pb with a 2485 keV γ ray. Therefore, the 2485 keV transition and the related family of transitions belong most likely to ^{207}Pb. In the present measurements, this issue was also addressed. From coincidence relationships in both the ^{208}Pb and ^{209}Bi data sets, no evidence was found for the placement of the 2485 keV γ ray in ^{208}Pb. This conclusion is based on the following arguments: (i) Spectrum (a), Figure 5.6, is the prompt coincidence spectrum gated by the $3^- \rightarrow 0^+$ transition in ^{208}Pb constructed from the ^{209}Bi target data set. It can be clearly seen that there is no evidence for the 2485 keV line in this spectrum. If this γ ray truly belongs to the ^{208}Pb nucleus, it should be present in this coincidence

spectrum since in a Coulomb excitation measurement one should expect to excite both the beam (^{208}Pb) and target (^{209}Bi) nuclei simultaneously. The presence of the 2485 keV transition in spectrum (b) which constructed from the ^{208}Pb target data set, Figure 5.6, on the other hand is not surprising and can be attributed to the decay of states populated in single-neutron evaporation reactions. (ii) The coincidence spectrum obtained by gating on the 2485 keV transition, presented in Figure 5.7, shows no trace of either the $3^- \rightarrow 0^+$ or $5^- \rightarrow 3^-$ transitions in ^{208}Pb. If the 2485 keV transition is the deexcitation of the double octupole phonon to the 5^- state (as proposed in reference [Wol92]), one would expect both the 583 keV and the 2614 keV transitions to follow (i.e. to be in coincidence with the 2485 keV transition). Instead, 6 new transitions, previously reported in reference [Sch92], are seen in coincidence with the 2485 keV transition as illustrated in Figure 5.8 where they are placed in a partial level scheme from their mutual coincidences. The placement of the 2485 keV transition in the ^{207}Pb nuclei instead of the ^{208}Pb is also supported by the work reported in reference [Yeh96].

(3) Examining the Coincidence Spectra Gated on the $3^- \rightarrow 0^+$ and $5^- \rightarrow 3^-$ Transitions in ^{208}Pb

As mentioned earlier, almost all γ rays produced in our data set were identified and assigned to a nucleus. In particular, all γ rays belonging to the ^{208}Pb nucleus were identified from coincidence relationships and their relative intensities (relative to the $3^- \rightarrow 0^+$ transition in ^{208}Pb) were determined after the usual correction for detector efficiency and internal conversion. These results were summarized in Table 5.2.1. The partial decay scheme of ^{208}Pb nucleus that is relevant to our measurement was constructed and is presented in Figure 5.9. The widths of the arrows are proportional to the measured intensities of the transitions. States with spins up to $14\hbar$ were populated in these measurements. The majority of the transitions between the high spin states reported in earlier [Sch93] work has also been observed in the present experiment.

At this point of the analysis, almost all the γ rays produced in the data had been placed in their respective nuclei and the placement of the 2485 keV γ ray in ^{207}Pb had

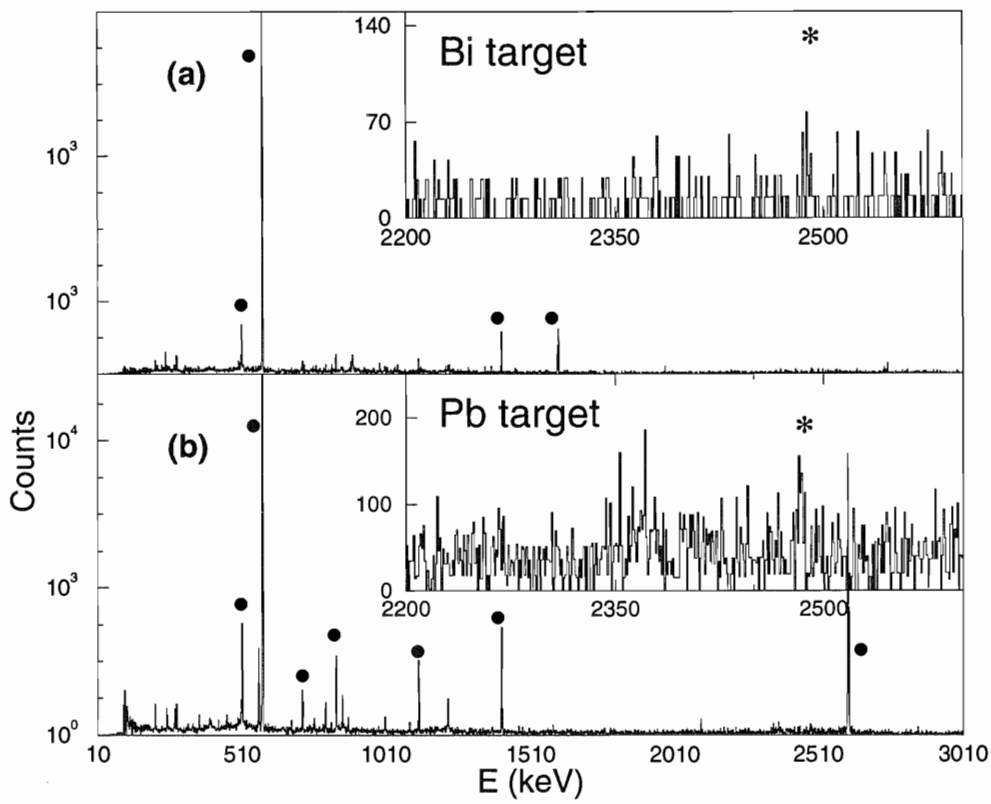

Figure 5.6 Coincidence spectra obtained by gating on the $3^- \rightarrow 0^+$ (2614 keV) γ ray in ^{208}Pb (a) from the ^{209}Bi data set and (b) from the ^{208}Pb data set. The symbol $*$ in the inserts marks the expected position of the 2485 keV γ ray. The symbol $\bullet$ marks known transitions in ^{208}Pb nucleus.

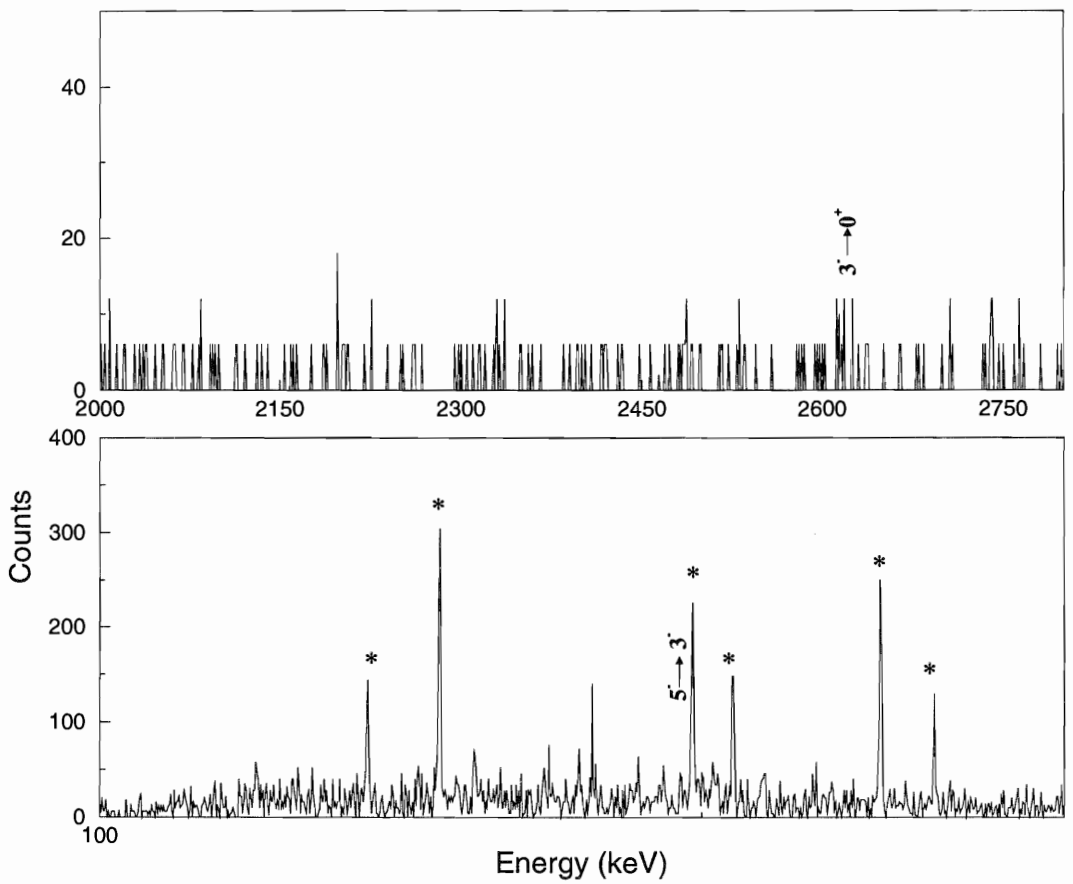

Figure 5.7 Coincidence spectrum obtained by gating on the 2485 keV transition from the ^{209}Bi target data set. It is clear that the high energy part of this coincidence spectrum (top) does not show any trace of the 2614 keV transition. In addition to that, the low energy part of this spectrum shows no trace of the 583 keV transition. The symbol $*$ marks all the transitions in coincidence with the 2485 keV. These are placed in the level scheme of the next Figure.

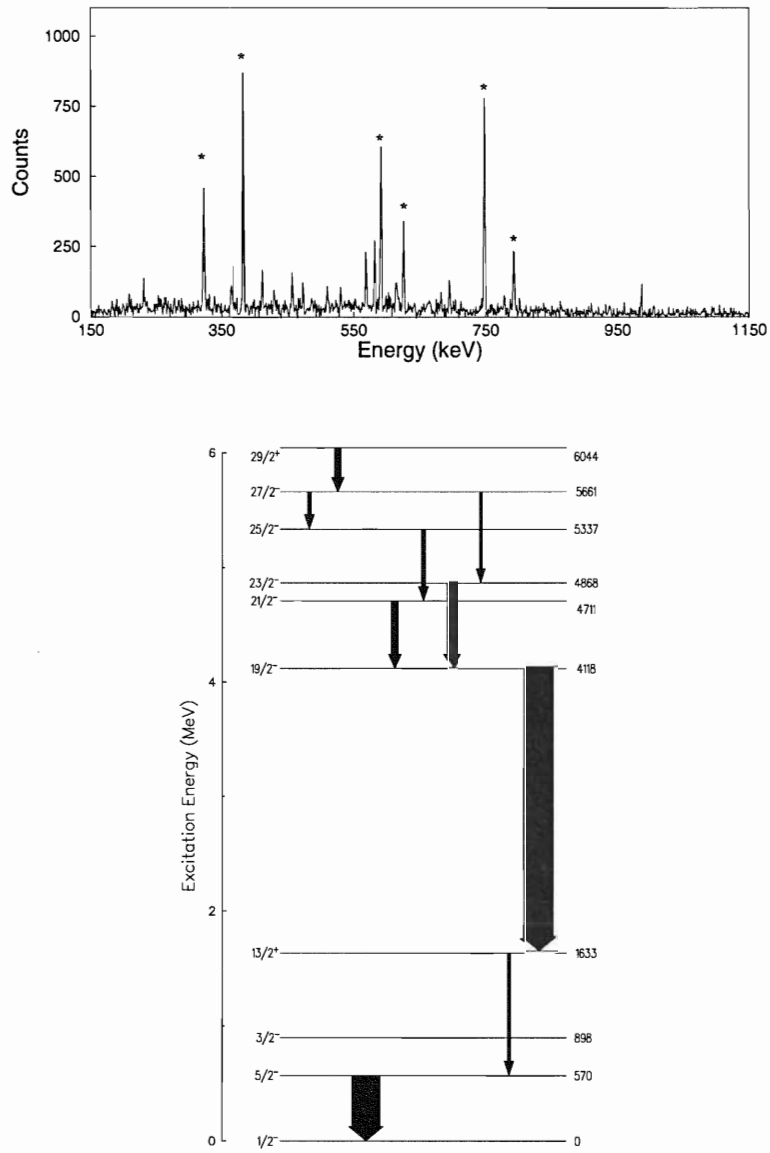

Figure 5.8 Coincidence spectrum obtained by gating on the 2485 keV transition in ^{207}Pb (top). The symbol $*$ marks all the γ rays in coincidence with this transition. The partial decay scheme in ^{207}Pb illustrates the coincidence relationship between those transitions. The width of the arrows in this level scheme are proportional to the measured intensities of the transitions. The fact that the measured intensity of the $13/2^+ \rightarrow 3/2^-$ transition is less than that of the 2485 keV transition is understood in terms of the $13/2^+$ level being an isomer.

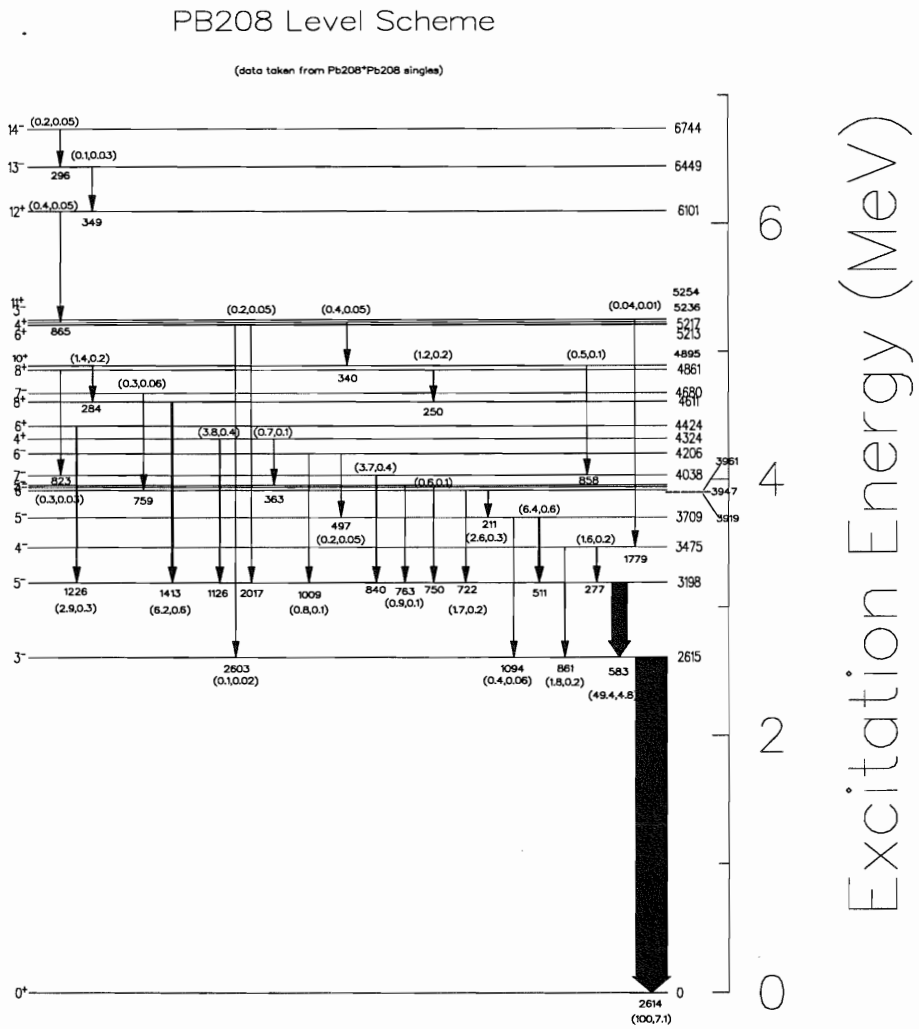

Figure 5.9 Partial decay scheme in ^{208}Pb showing transitions observed in the present measurements. The width of the arrows are proportional to the measured intensities of the transitions.

Table 5.2 A list of all the γ rays that are in coincidence with the $3^- \rightarrow 0^+$ transition in ^{208}Pb. The intensities are normalized to the intensity of the $3^- \rightarrow 0^+$ transition in ^{208}Pb. The assignment of those γ rays has been verified from coincidence relationships in both the ^{208}Pb and the ^{209}Bi targets.

E_γ (keV)	Relative intensity
2614	100.0±7.10
583	14.44±1.42
277	0.46±0.05
860	0.53±0.06
510	1.87±0.12
1094	0.12±0.02
211	0.76±0.08
722	0.49±0.05
750	0.17±0.025
763	0.26 ±0.03
840	1.10±0.11
497	0.06±0.01

E_γ (keV)	Relative intensity
1088	0.22±0.02
363	0.22±0.03
1126	1.10±0.11
1413	1.81±0.18
759	0.10±0.018
250	0.35±0.04
284	0.42±0.05
857	0.14±0.02
2017	0.06±0.01
2603	0.03±0.01
340	0.11±0.01
1779	0.01±0.002
865	0.11±0.02
349	0.04±0.01
296	0.06±0.01
823	0.08±0.01

been confirmed. Due to the fact that the decay of the two-phonon vibrational states is believed to be in coincidence with $3^- \rightarrow 0^+$ (2614 keV γ ray) and the $5^- \rightarrow 3^-$ (583 keV γ ray) transitions in ^{208}Pb, it becomes essential to search the coincidence spectra gated on the $3^- \rightarrow 0^+$ and the $5^- \rightarrow 3^-$ transitions for any unknown γ ray in the energy region expected for the decay of the two-phonon multiplets (i.e. $E_\gamma \sim 2.2 - 2.8MeV$). Figures 5.6 and 5.10 show the relevant coincidence spectra constructed by gating on $3^- \rightarrow 0^+$ and the on $5^- \rightarrow 3^-$ transitions in ^{208}Pb, respectively. The inserts in both figures focus on the energy region where the decay of the two-phonon multiplets is anticipated. A very thorough examination of both Figures reveals that all discrete lines in both coincidence spectra can be assigned to known decays in the ^{208}Pb nucleus, and they have been placed in the partial level scheme presented in Figure 5.9. No new sharp lines in coincidence with both the $3^- \rightarrow 0^+$ and/or $5^- \rightarrow 3^-$ transitions were observed. This negative result lead us to a search for Doppler broadened lines or even complex structures in coincidence with the $3^- \rightarrow 0^+$ and/or $5^- \rightarrow 3^-$ transitions.

5.2.2 Angle-Sorted Prompt $\gamma - \gamma$ Coincidence Matrices

In the pure harmonic approximation, assuming $E3$ transitions, one would expect a decay half-life for the two-phonon states of about 8×10^{-12} seconds, nearly a factor of 3 longer than the stopping times of the recoiling Pb nuclei in our target. If, however, the decay of the 6^+ and/or 4^+ members of the 2-phonon members proceeds via $E1$ transitions to the 5^- state, the lifetime could be somewhat shorter and the resulting γ rays could be severely Doppler broadened or perhaps even Doppler shifted. Another possible scenario would involve fragmentation of the decay pathways due to the large level density at high excitation energies (as is thought to be the case in the decay out of the superdeformed bands) and one may only be able to observe broad structures in the coincidence spectra. In order to investigate these possibilities, the coincidence spectra presented in Figures 5.6 and 5.10 were reexamined with a special emphasis on the possible presence of any broad structures. A few possible candidates were found although they are very weak. The data was then sorted according to the detector angle in order to examine if those broadened

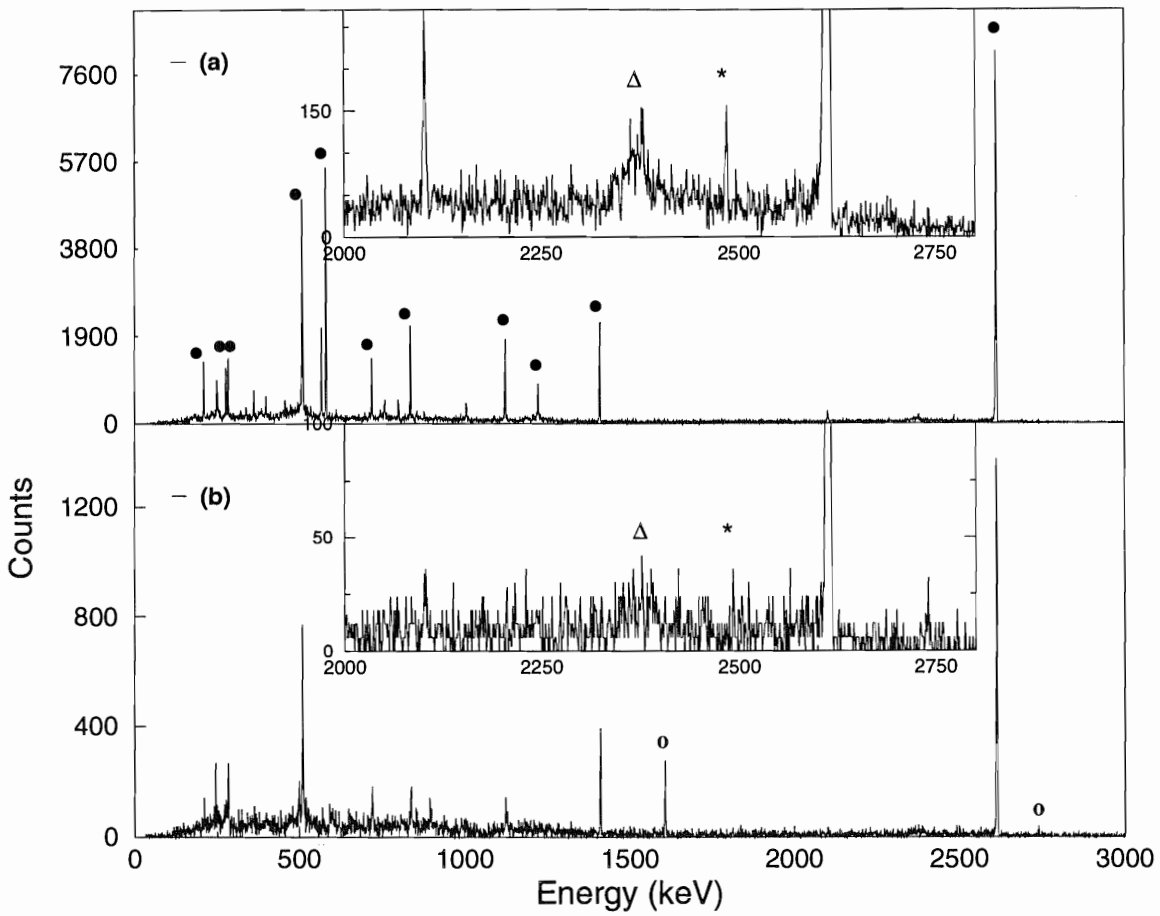

Figure 5.10 Coincidence spectra obtained by gating on the $5^- \rightarrow 3^-$ (583 keV) γ ray in ^{208}Pb (a) from the ^{208}Pb data set and (b) from the ^{209}Bi data set. The inserts in both figures focus on the energy region expected for the decay of the two-phonon multiplets (i.e. $E_\gamma \sim 2.2 - 2.8$ MeV) where the $*$ symbol labels the expected position of the 2485 keV γ ray and the Δ symbol marks the expected position of the escaped peak of the 2614 keV γ ray. The sharp lines in insert (a) are known transitions in ^{208}Pb. The sharp lines labeled by the symbol $\bullet$ marks known transitions in ^{208}Pb while the open symbol $\circ$ marks known transitions in ^{209}Bi. The insert in spectrum (b) exhibits no sharp lines or broad lines while the insert in spectrum (a) again shows the 2485 keV line as is expected.

structures exhibit the angular dependence expected for transitions undergoing a Doppler shift.

The 12 Compton-suppressed Ge-detectors in the Argonne-Notre Dame BGO γ-ray facility are grouped in three sets of 4 detectors each, located at $\pm 34.5°$, $\pm 90.0°$ and $\pm 145.5°$ with respect to the beam direction. This arrangement allows for
angle-sorting of the data (i.e. the construction of coincidence spectra corresponding to each of the three angles above, gated by the transitions in ^{208}Pb). Several candidate broad structures are present in the coincidence spectra gated on the $3^- \rightarrow 0^+$ and $5^- \rightarrow 3^-$ transitions in ^{208}Pb. At least one of these "bumps" (at about 2.5 MeV) exhibits the angular dependence expected for Doppler broadened transitions (i.e. these transitions will have a component that is shifted to higher γ-ray energies in the spectrum constructed from coincident γ rays collected in the forward detectors (fwd-spectrum) and a component shifted to a lower γ-ray energies in the spectrum from the backward detectors (bwd-spectrum)). If the bwd-spectrum is subtracted from the fwd-spectrum, (diff-spectrum), one expects the sharp unshifted γ rays to cancel out, while the sharp Doppler shifted lines appear as positive and negative spikes in the diff-spectrum. Furthermore, the Doppler broadened lines will appear in the form of a characteristic S like shape in the diff-spectrum, as is illustrated schematically in Figure 5.12. This technique of pattern recognition is not new. It was used successfully in References [Dri90] in the case of a collective structure in the ^{148}Gd nucleus. It is clear in Figure 5.11 that at an energy of 2.5 MeV there is an S shape suggesting that this might correspond to the decay out from one of the 2-phonon members. This is only a tantalizing possibility since this bump has very low statistics; the intensity corresponds at most to $0.233(\pm 0.033)\%$ of the $3^- \rightarrow 0^+$ transition. More statistics is expected from the LBNL experiment which should enable us to determine if, indeed, this bump corresponds to a discrete transition in ^{208}Pb which meets the expectations for the decay out from the 2-phonon members. It should be pointed out that the 2.5 MeV candidate is the only one showing decisively the expected S shape pattern. Any other broad structure in the $3^- \rightarrow 0^+$ and $5^- \rightarrow 3^-$ coincidence spectra (i) were weaker in intensity and (ii) did not show the expected Doppler shifts. Thus, these attempts

complete our negative search for the double octupole phonon states in ^{208}Pb from the ANL experiments.

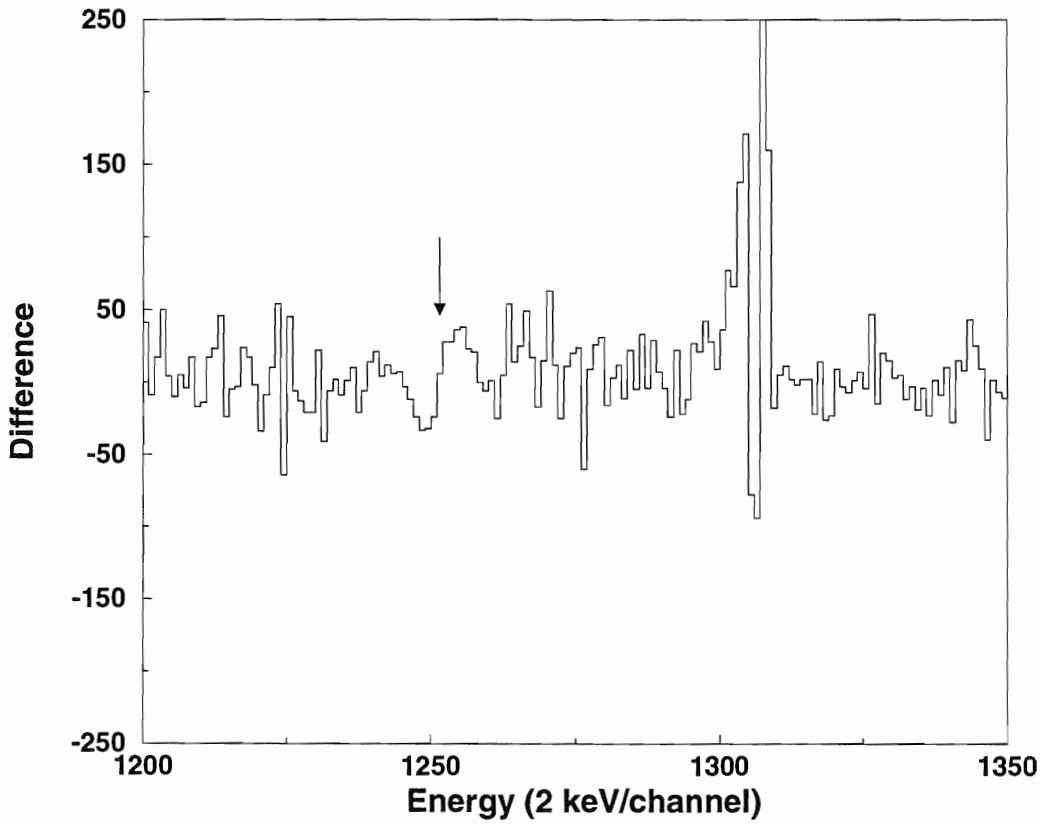

Figure 5.11 This spectrum shows the energy region of the diff-spectrum, see text, with an arrow pointing to the location of the bump at an energy of 2.5 MeV. The S shape described in the text is clearly visible.

5.3 Data Analysis of the LBNL Measurements

The detailed analysis of the thick target data will be presented in the following sections. The results obtained with the thin target will be discussed only briefly, since the detailed analysis was performed by our collaborators at LBNL.

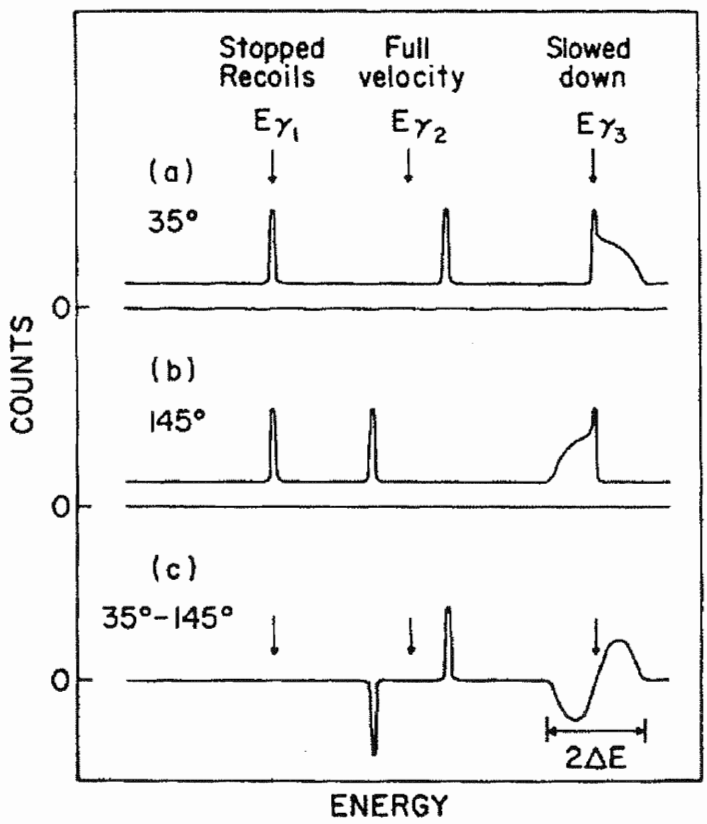

Figure 5.12 A cartoon illustrating what one would expect to see in the diff-spectrum when the three different γ rays (i.e. sharp shifted lines, sharp unshifted lines, and broad lines) are present in both the fwd-spectrum and bwd-spectrum.

5.3.1 The Thick Target Data Analysis

The primary goal of sorting this data set was a search for the two-phonon octupole vibrational states in ^{208}Pb. For this purpose, double coincidence spectra gated on transitions in ^{208}Pb and, in particular, on the $3^- \rightarrow 0^+$ and $5^- \rightarrow 3^-$ transitions are essential since the 3^- and the 5^- levels are believed to be the only states to which the γ rays deexciting the two-phonon octupole vibrational members will decay. Coincidence spectra gated on combinations of transitions in ^{208}Pb and ^{136}Xe are also of interest since mutual excitations of both the target and the beam particles can be expected in the presence of the strong Coulomb field (i.e. γ rays from both nuclei are expected to be seen in coincidence with each other). More details on the analysis will be given in the following sections.

5.3.2 Construction of Prompt Triple Coincidence Cubes and Matrices.

Since three- and higher-fold coincidence events were recorded during the experiment, the data were sorted into the following coincidence cubes and matrices:

(1) A cube with multiplicity 3 and higher

In this case, all events with multiplicity > 3 are decomposed into triples and histogramed into a triple coincidence cube, together with the $\gamma - \gamma - \gamma$ events.

(2) A cube with multiplicities 3 and 4 only

Since the beam energy was about 20% above the Coulomb barrier, transfer channels which dominate the higher multiplicity events (i.e. > 4), were found to be so strong in the first cube that transitions in ^{208}Pb were barely visible in the total projection. It became clear (as is illustrated in Figure 5.13) that a coincidence cube containing low multiplicity events only (i.e. three and four fold events only) was essential. Multiplicity 4 events were found to be useful because these combine many coincidence events where either ^{208}Pb X-rays or the ^{136}Xe $2^+ \rightarrow 0^+$ transition are detected in coincidence with both the $3^- \rightarrow 0^+$ and the $5^- \rightarrow 3^-$ γ rays in ^{208}Pb.

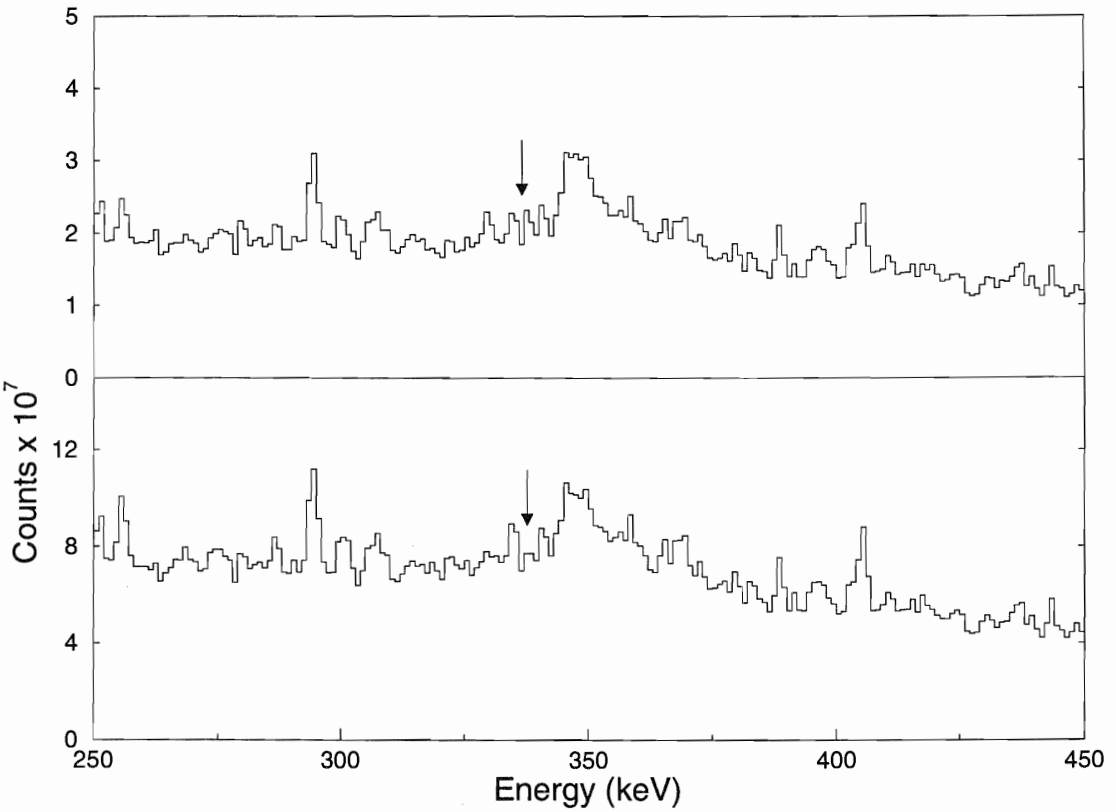

Figure 5.13 The total projection of the coincidence cubes constructed from events with multiplicities 3 and 4 only (top) and from events with multiplicities ≥ 3 (bottom). The arrow in both inserts points at the position of the 583 keV, $5^- \rightarrow 3^-$ transition in the ^{208}Pb nucleus. It is clear that the 583 keV transition is barely visible in the total projection of the first cube, and not at all in the second one.

Just to get a feeling about the coincidence rates, it is interesting to note that the intensity of the $3^- \rightarrow 0^+$ transition in ^{208}Pb, extracted from the second cube, is 2.0×10^6. On the other hand, this intensity extracted from the first cube is 3.2×10^6. Note also that the intensity extracted from the second cube for the $2^+ \rightarrow 0^+$ transition in ^{136}Xe is 3.5×10^6.

(3) gated $\gamma - \gamma$ matrices

A gated $\gamma - \gamma$ matrix was used as a double check on the results from the second cube (i.e. constructing a gated spectrum from a gated $\gamma - \gamma$ matrix is equivalent to constructing a double gated spectrum from a triple coincidence cube as is illustrated in Figure 5.14). Furthermore, this sorting was preferred when a better background subtraction was needed. Three matrices were constructed; the first gated on the $3^- \rightarrow 0^+$ transition, the second gated on the $5^- \rightarrow 3^-$ transition, and the third gated on the $2^+ \rightarrow 0^+$ transition in ^{136}Xe.

(4) angle sorted $\gamma - \gamma$ matrices

Finally, for reasons discussed in section 1.4 (the 2-phonon states lifetimes are expected to be of the order of few *ps*), angle sorting of the data was performed to search for effects associated with Doppler broadening/shift.

5.4 Results

Calculations of the excitation probability of members of the 2-phonon multiplet and simulations of the line shape(s) of γ rays deexciting these states have been performed in an attempt to understand what one should expect to see in the spectra of interest resulting from this experiment. In the following sections, results of these calculations and simulations will be presented. Results from searches of the data for any γ ray that could correspond to the decay from members of the 2-phonon multiplet will be presented subsequently. The upper limits for the population of members of the 2-phonon multiplet have been derived in the present work using the guidance provided by the calculations and simulations. These limits are presented in the last part of this section.

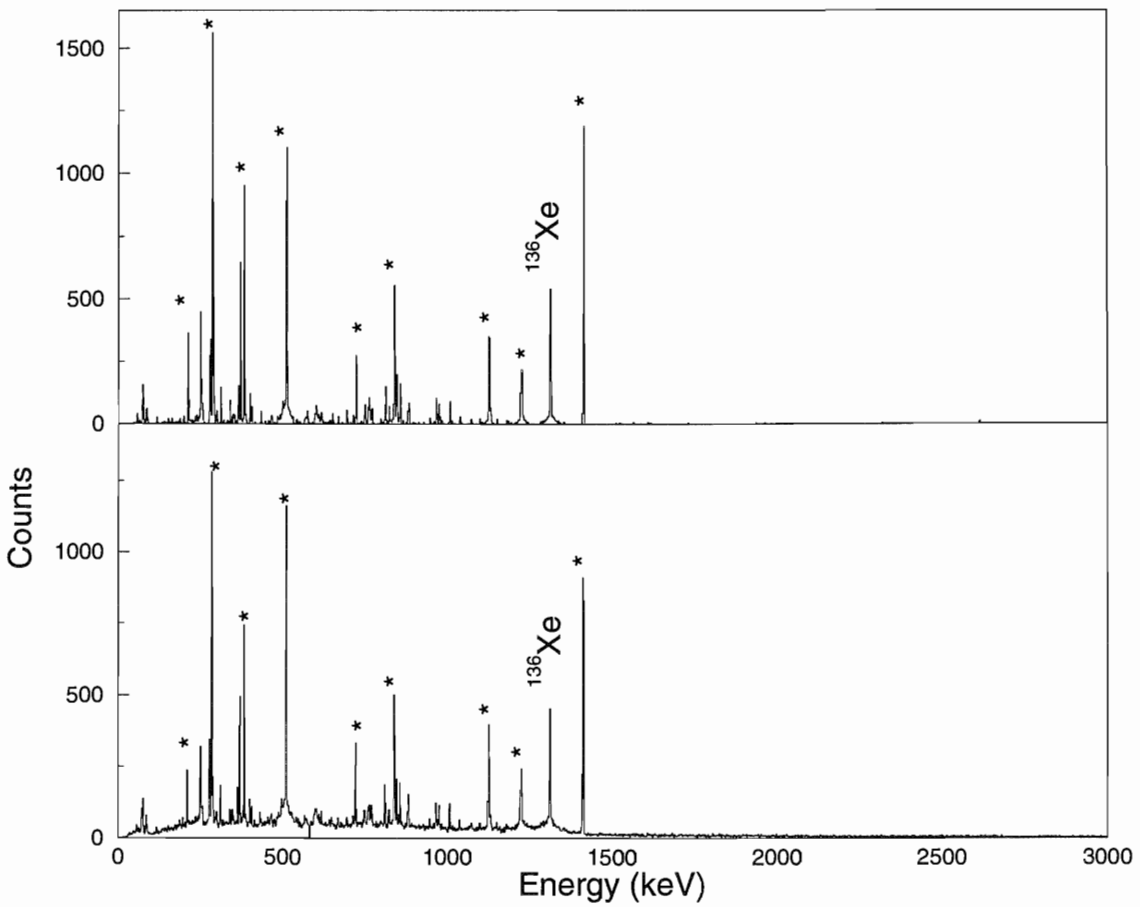

Figure 5.14 The coincidence spectrum gated on the 583 and 2614 transitions as constructed from the second cube (top) and the coincidence spectrum gated on the 583 transition as constructed from the $\gamma - \gamma$ matrix gated on the 2614 transition (bottom). In principle, these two spectra should be equivalent. The main difference between the two spectra is in the background as it appears that the top spectrum may well be over subtracted.

5.4.1 Cross Section Calculations and Line-Shape Simulations

In the following two sections results from line-shape simulations and the cross section calculations will be presented. The final section will summarize what was learned from those results.

1) Cross Section Calculations for the feeding of the One-phonon state and the Two-Phonon multiplet

Coupled channel calculations using the code PTOLEMY were performed (as discussed earlier) to determine the total cross sections for the one- and the 2-phonon octupole vibrational states as a function of the beam energy. The cross sections of the members of the the 2-phonon multiplet relative to the population of the first 3^- level (i.e. σ/σ_{3^-}) are summarized in Table 5.3.

2-phonon member	6^+	4^+	2^+	0^+
(σ/σ_{3^-}) %	2.94	1.14	0.77	0.52

Table 5.3 Total cross sections for the population of the 2-phonon octupole vibrational multiplet (from coupled channel calculations using the code PTOLEMY) relative to that of the one-phonon state for the ^{136}Xe+^{208}Pb system at a beam energy of 884 MeV.

2) Monte-Carlo Simulation of the Excitation of the Two-Phonon States

Due to the fact that thick targets were used in all measurements, the line shape(s) of the γ rays emitted in the deexcitation of the 2-phonon octupole multiplet are of interest for the present discussion. Therefore, a Monte-Carlo simulation was performed to simulate the peak shape as a function of the state lifetime for the transition deexciting the 6^+ member of the two-phonon octupole multiplet towards the 5^- state. Those simulations were carried out for the kinematics corresponding to the ^{136}Xe+^{208}Pb system at 884 MeV, under the assumption that the excitation energy of the 6^+ state is 5.683 MeV (i.e. about twice

the excitation energy of the one-phonon state), and that the cross section corresponds to the harmonic limit for the 2-phonon states. In order to fully appreciate the intrinsic lineshape as a function of the state lifetime, the γ-ray spectra were first simulated without background. In a second simulation, those spectra were generated not only from photopeak events, but also from Compton backscattered events (due to the $3^- \rightarrow 0^+$ transition). Results from the simulations are illustrated in the next three figures. Figure 5.15 presents the lineshape dependence on the detector angle for the $6^+ \rightarrow 5^-$ γ ray, if the lifetime of the 6^+ state is 3.0 *ps*. Figures 5.16 and 5.17 illustrate the lineshape dependence on the state lifetime, without and with the addition of a background component, respectively.

3) Discussion of the Results of the Yield Calculations and of the Line-shape simulations

In view of the results described above, the following can be concluded about the γ rays deexciting members of the two-phonon octupole multiplet:

1. γ rays deexciting members of the 2-phonon multiplet will be very weak (i.e. have an intensity of $\sim 0.5 - 3\%$ of the 2614 keV transition, as is illustrated in Table 5.3).

2. The lineshape (of any of the deexciting γ rays) is lifetime dependent, and three different situations can be recognized as a result of the lineshape simulations. First, if the state lifetime, τ, is sufficiently long (> 3 *ps* as the simulations indicate) the deexciting γ ray will be a sharp peak since it is emitted when the nucleus is fully stopped in the target. If $\tau < 0.5$ *ps*, then the yield of the γ ray is spread over a ~ 400 keV range and there is no sharp, stopped peak. Finally, if τ has a value somewhere between 0.5 and 3 *ps*, both stopped and shifted components should be present.

3. In the last case discussed above (i.e. τ is between 0.5 and 3 *ps*), the expected ratio between the strengths of the stopped (I_{st}) and the shifted (I_{sh}) components of the $6^+ \rightarrow 5^-$ transition varies as a function of state lifetime as $(I_{st})/(I_{sh})$=(74, 34, 8)% for $\tau = 3, 2, 1$ *ps*, respectively.

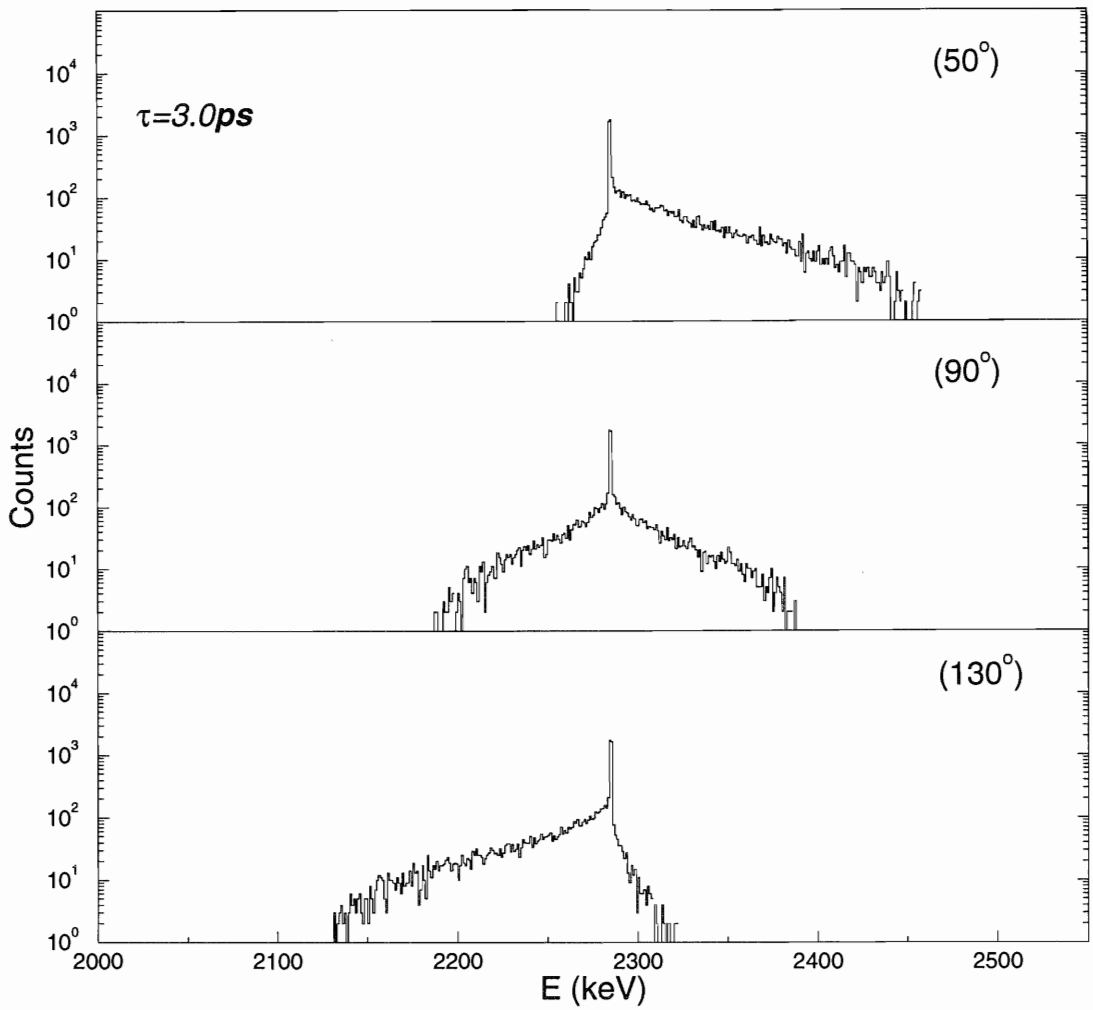

Figure 5.15 A Monte-Carlo simulation of the peak shape for the $6^+ \rightarrow 5^-$ transition deexciting the 6^+ member of the two-phonon octupole multiplet. The lifetime is assumed to be 3.0 *ps*. These spectra are constructed from Gammasphere rings of detectors located at a forward angle (top), 90° (middle) and backward angle with respect to the beam direction.

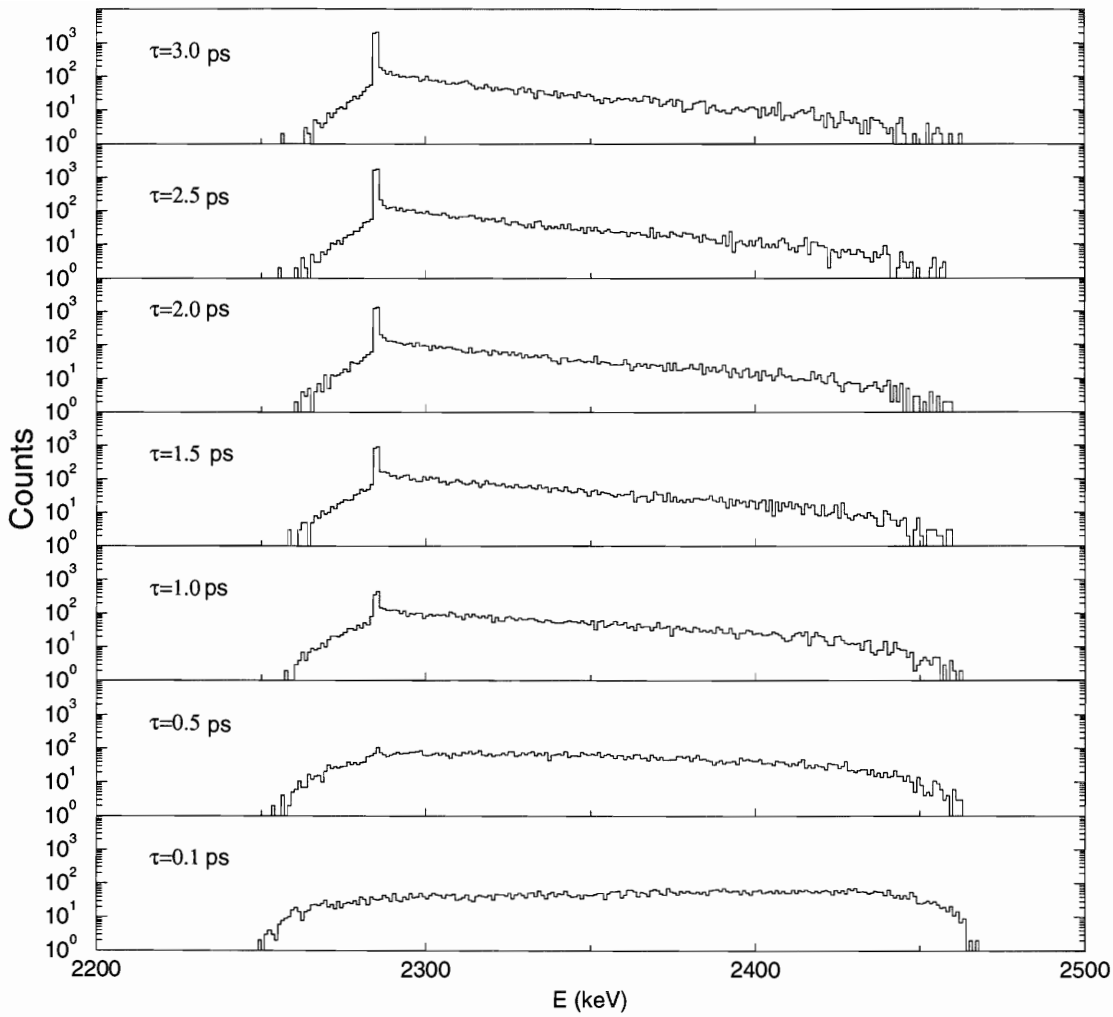

Figure 5.16 A Monte-Carlo simulation of the peak shape for the $6^+ \rightarrow 5^-$ transition deexciting the 6^+ member of the two-phonon octupole multiplet. The lifetime is assumed to vary between 0.1 and 3.0 *ps* in the various panels of the figure. These spectra are constructed for a ring of Gammasphere detectors located at 50° with respect to the beam direction. A stopped component of the peak can only be seen for $\tau > 0.5$ *ps*

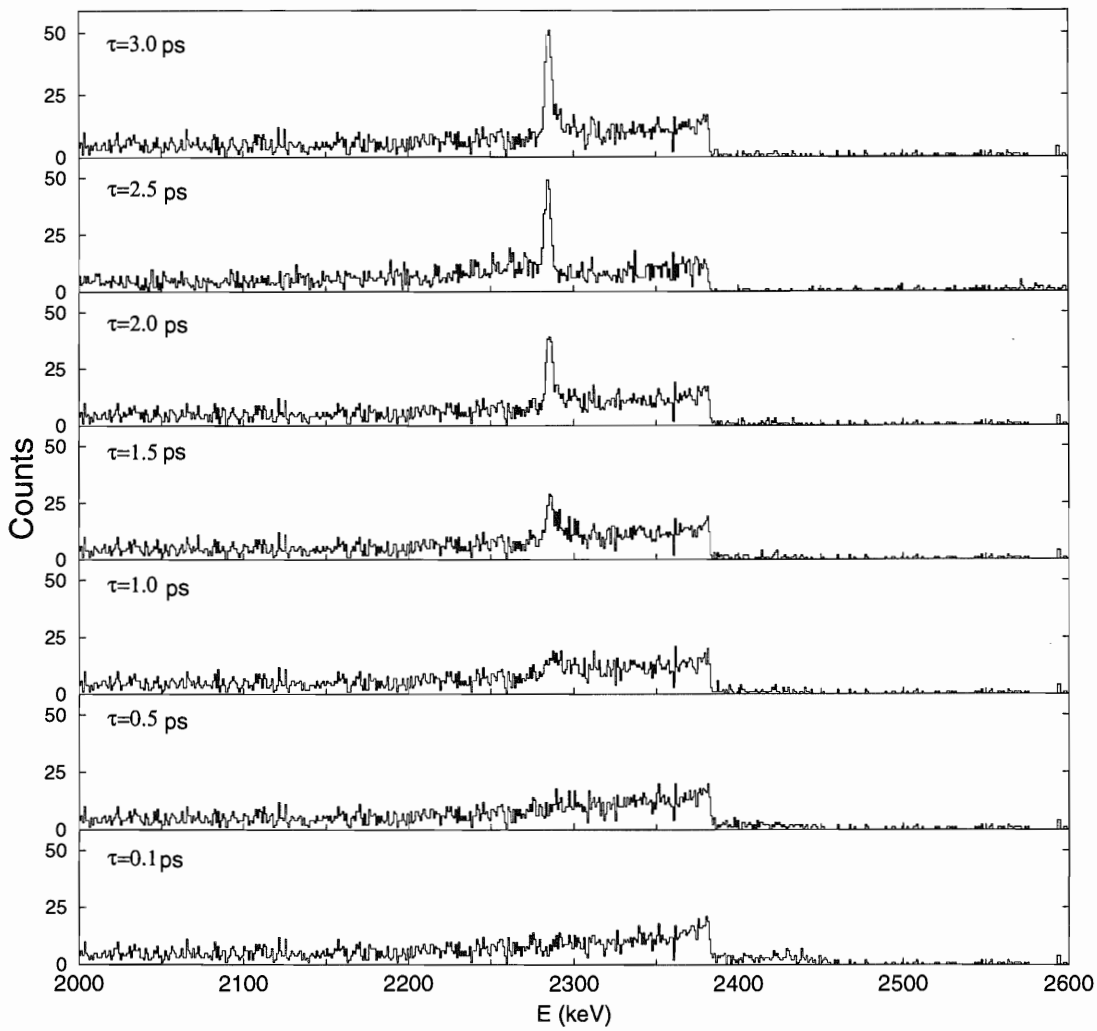

Figure 5.17 A Monte-Carlo simulation of the peak shape for the $6^+ \rightarrow 5^-$ transition deexciting the 6^+ member of the two-phonon octupole multiplet. The lifetime is assumed to vary between 0.1 and 3.0 *ps* and background is added, originating from Compton scattering of the $3^- \rightarrow 0^+$ γ ray. The purpose of the exercise is to simulate more realistic experimental conditions. These spectra are constructed for a ring of Gammasphere detectors located at 50° with respect to the beam direction.

4. Combining these values with the calculated ratio of yields σ_{6+}/σ_{3-} (2.94%), gives the expected strength for the stopped component of the $6^+ \rightarrow 5^-$ transition relative to the $3^- \rightarrow 0^+$ γ ray as a function of the state lifetime. This is illustrated in Figure 5.18 and Table 5.4.

$\tau(ps)$	$(I_{st})/(I_{sh})\%$	$(I_{st})/(I_{sh})$*(2.94%)
3	74	2.17%
2	34	1.0 %
1	8	0.24%

Table 5.4 Results from cross section calculations of the 6^+ member of the 2-phonon multiplet combined with results from line-shape(s) simulations to extract the intensity of an expected stopped component of the $6^+ \rightarrow 5^-$ transition relative to the $3^- \rightarrow 0^+$ transition.

From the findings 1-4 above, a clear "plan of attack" for the analysis of the data is apparent. First, coincidence spectra gated on the $3^- \rightarrow 0^+$ and $5^- \rightarrow 3^-$ transitions should be searched for weak, sharp peaks. The fact that the peaks have small intensity, and could be as weak as 0.25% of the $3^- \rightarrow 0^+$ transition, should not be viewed as a discouraging factor: Gammasphere was designed and built for the detection of very weak events, provided that a data sample of sufficient statistics is accumulated. If weak peaks are found, they become candidates for the decay of members of the double octupole multiplet, the energies give information on the degree of anharmonicity of the vibration, and the data also provide indications about the lifetimes of the levels involved (a comparison of the measured yield with those calculated -e.g. in Table 5.4- can be used to this effect). In the absence of sharp peaks, the problem becomes one of determining accurate upper limits. Again, the findings 1-4 above indicate that these limits become dependent on the state lifetimes and will become less significant as the state lifetimes become shorter.

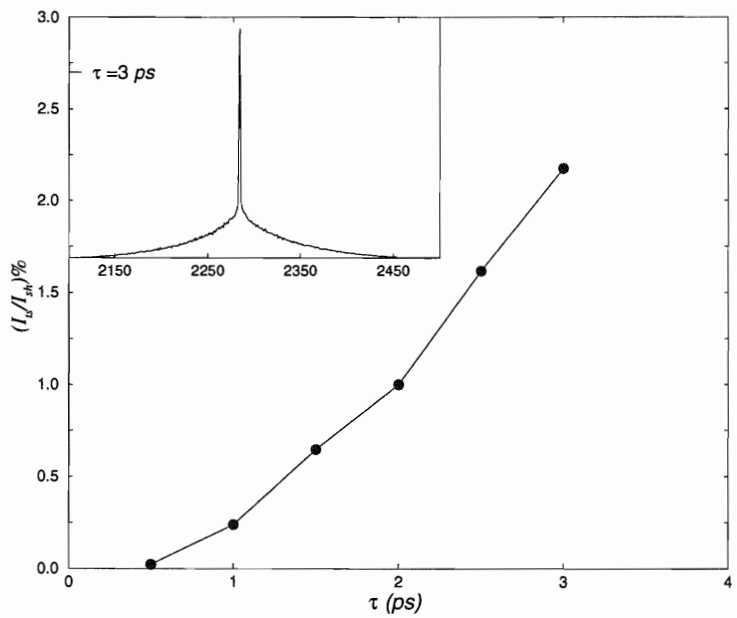

Figure 5.18 The expected strength for the stopped component of the 6^+ relative to the $3^- \rightarrow 0^+$ transition as a function of the state lifetime. The insert shows the line shape for the γ ray deexciting the 6^+ member of the 2-phonon multiplet for a lifetime of 3 *ps*.

5.4.2 Searching the Data for Sharp Peaks

At this point of the analysis, a sharp peak(s) is expected to be present in the data corresponding to the deexcitation of a member(s) of the 2-phonon multiplet. In order to search the data for such peak(s), several double-gated coincidence spectra (constructed from the second cube and/or the gated $\gamma - \gamma$ coincidence matrices) have been studied carefully, the ones of most interest to the present search are gated on:

1) $3^- \rightarrow 0^+$ and $5^- \rightarrow 3^-$ (i.e. 2614 and 583 keV)

2) $3^- \rightarrow 0^+$ and $(2^+ \rightarrow 0^+)_{^{136}Xe}$ (i.e. 2614 and 1313 keV)

3) $5^- \rightarrow 3^-$ and $(2^+ \rightarrow 0^+)_{^{136}Xe}$ (i.e. 583 and 1313 keV)

Figure 5.19 presents all three double gated spectra constructed from the second cube. This figure illustrates the high statistical accuracy of the data. As was the case with the data obtained in the ATLAS measurement, every γ ray present in these spectra was carefully inspected and, from coincidence relationships, all the sharp lines were identified and assigned to transitions in either ^{208}Pb or ^{136}Xe nuclei. This result illustrates (i) that there was no contamination in these coincidence spectra from other reaction channels and (ii) that the understanding of the data is excellent. In fact, several new transitions were placed in the ^{208}Pb level scheme as will be discussed in a following section.

The inserts in Figure 5.19 represent the region of interest (i.e. 2.2-2.8 MeV) where deexcitations from the 2-phonon multiplet should occur. This region, in all three coincidence spectra, was inspected carefully for sharp peaks. With the exception of the 2318 keV γ ray (present in the 2614 & 583 double gated coincidence spectrum), no sharp γ ray was found in the region of interest in any of those spectra. The 2318 keV γ ray was investigated and placed in the ^{208}Pb level scheme as corresponding to a $17^+ \rightarrow 14^- E3$ transition (a detailed discussion of this placement follows below). This γ ray is also clearly present in the coincidence spectrum of Figure 5.20, which is gated only on the $3^- \rightarrow 0^+$ transition alone. The intensity of this γ ray, from the present analysis, relative to that of the $3^- \rightarrow 0^+$ transition is only $(0.11 \pm 0.02)\%$. Such a low number is clearly a good indication of the quality of the present data.

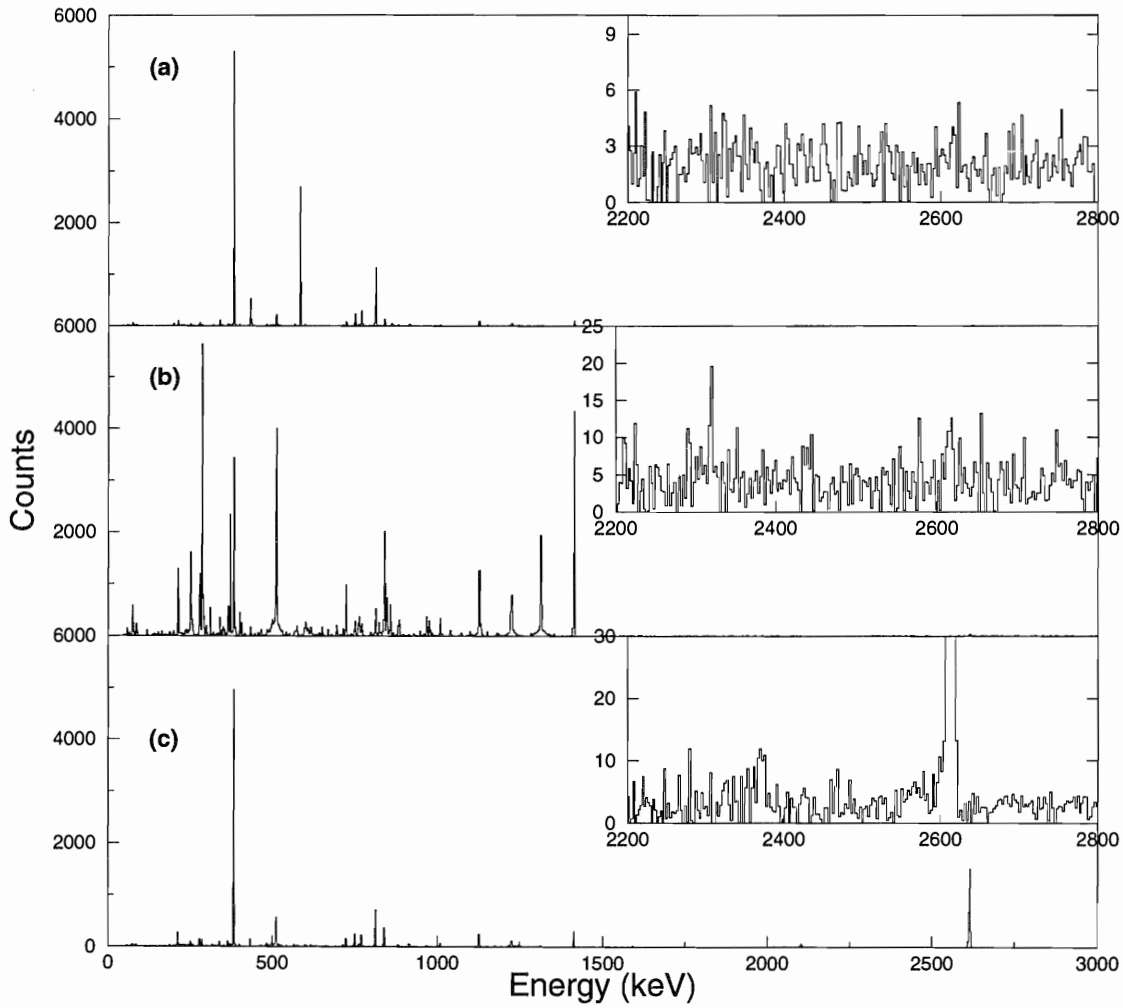

Figure 5.19 Double-gated coincidence spectra gated on; (a) 2614 & 1313, (b) 2614 & 583, and (c) 583 & 1313 transitions, respectively. The inserts in each spectrum focus on the region of interest (i.e. 2.2-2.8 MeV). The sharp lines in all spectra are known, assigned transitions in ^{208}Pb and in ^{136}Xe.

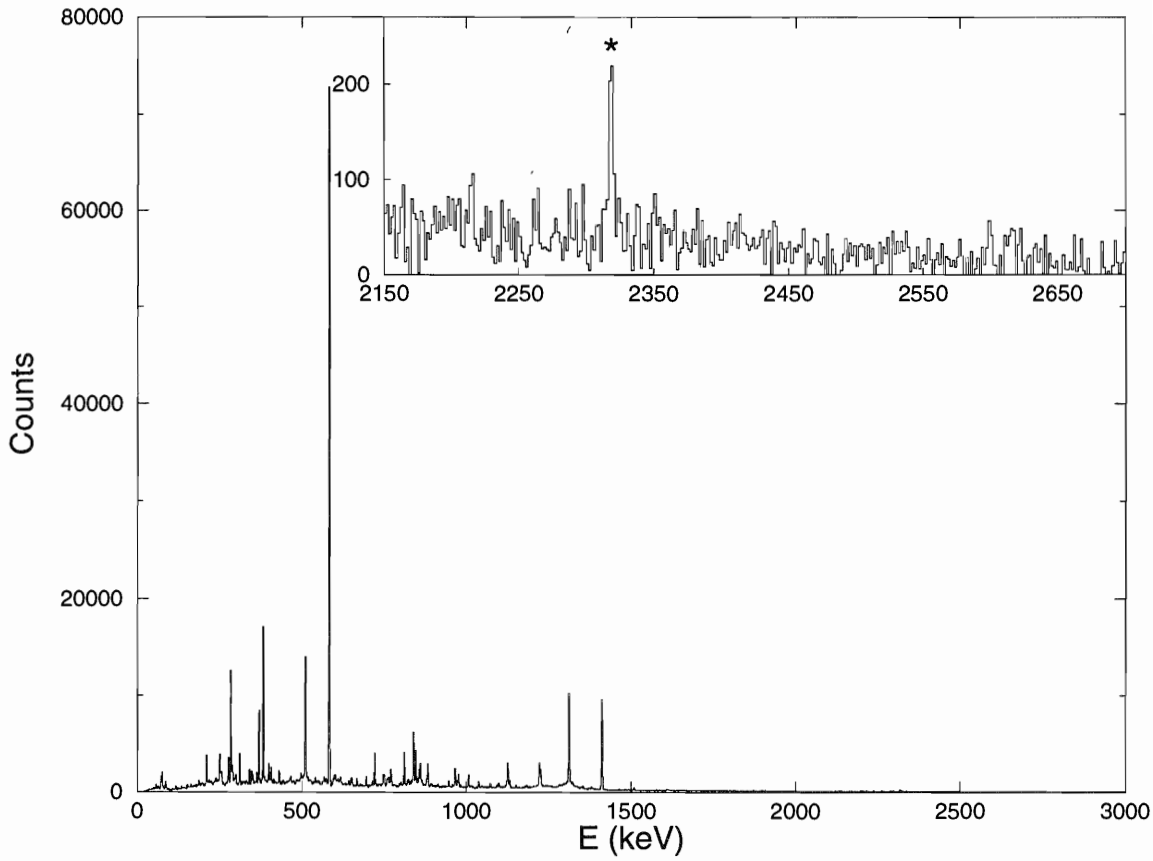

Figure 5.20 The coincidence spectrum gated on the $3^- \rightarrow 0^+$ transition. The sharp line in the insert, E_γ=2318 keV, is a new transition placed in ^{208}Pb level scheme.

5.4.3 Upper Limits on the Decay From the 2-Phonon Members

In view of the absence of any sharp peak other than the 2318 keV γ ray in the region of interest in all relevant coincidence spectra (as was illustrated in Figure 5.19), the results are expressed hereafter in terms of upper limits. Two different cases were considered:

1) Limits for state lifetimes > 3 *ps*; Lifetime-independent upper limits:

If the lifetime of the members of the 2-phonon multiplet is sufficiently longer than 3 *ps*, the deexcitation of the states will result in sharp peaks (for $\tau = 3$ *ps*, 75% of the total yield will be in a stopped peak). The upper limits in this case will be lifetime independent. It can be concluded from the negative results of the search obtained above that for such lifetimes any γ ray associated with the deexcitation of any member of the 2-phonon octupole multiplet must have an intensity well below 0.11% of the $3^- \rightarrow 0^+$ transition (i.e. below the intensity of the 2318 keV γ ray). As can be seen from Figures 5.19, and 5.20, the 2318 keV line stands out clearly above the background and even a peak weaker by a factor of 2-3 would have been observed. Hence a 0.1% upper limit is a conservative estimate.

2) Lifetime-dependent Upper Limits:

Two different cases were considered:

a) If the state lifetimes are between 0.5 and 3 *ps*

For this range of lifetimes the total yield in any transition will be shared between a stopped and a shifted component. Upper limits were extracted in the following manner: in the region of interest, every fluctuation above the background of the number of counts in a number of consecutive channels was considered as a "sharp peak". The intensity of these extremely weak "peaks" were then measured. As these "peaks" can only be viewed as upper limits, the measured intensities of these weak "peaks" were doubled. This can be taken to be a prudent, rather conservative approach. In a following step, a correction was applied as a function of the state lifetime. Indeed, the "peaks" correspond to a fraction of

the total yield and this was taken into account by considering the appropriate (i.e. lifetime dependent) $((I_{st})/(I_{sh}))$ factor. Those upper limits are presented in Figure 5.21.

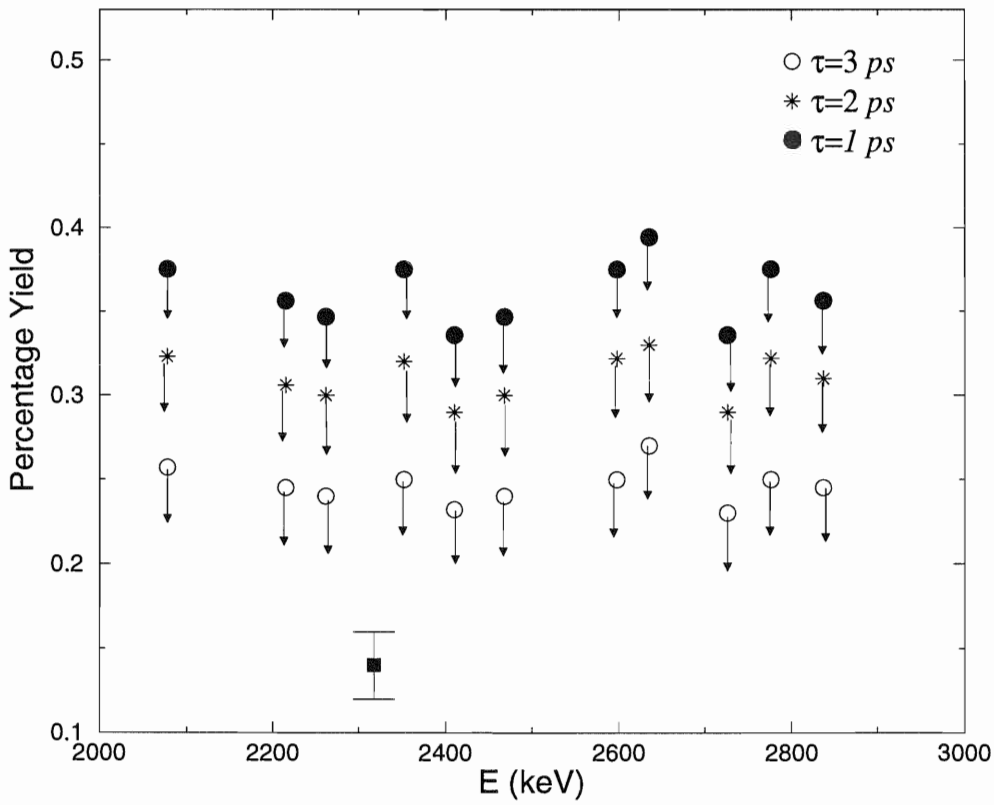

Figure 5.21 This figure illustrates the upper limits, as a function of energy, on the sharp component of the total yield of the γ ray decaying out of 6^+ member of the 2-phonon multiplet. Those limits are extracted assuming different state lifetimes and are normalized to the $3^- \rightarrow 0^+$ transition in ^{208}Pb nucleus. The relative intensity of the 2318 keV γ ray in ^{208}Pb is presented in this figure for illustration purposes.

b) If the state lifetimes are less than 0.5 *ps*

In this case, the lineshape will correspond to a broad bump extending over a $\sim$ 400 keV range (as is illustrated in Figure 5.16). To extract meaningful limits on the excitation of

the 2-phonon multiplets, it is necessary to insure that only photopeak events are present in the coincidence spectra. Though Gammasphere detectors are Compton suppressed, this suppression is not a 100% (i.e. some Compton-scattered events will remain in the data). Removing the Compton scattered γ rays from the coincidence spectra was done by using an "Unfolding" technique. This technique is described in detail in reference [Rad87]. Briefly, the response of a Gammasphere detector to mono-energetic γ rays from radioactive sources (covering the entire energy range of interest) is measured very carefully. With this response function, assuming that the highest channel in the spectrum contains only photopeak events, the contribution to all low channels due to partial collection of γ rays of this energy is removed. The process is then repeated for the next lowest channel until the "unfolding" reaches the lowest channel. This technique is well proven one, used in numerous spectroscopy applications by the Argonne group.

Figure 5.22 illustrates the effect of unfolding by showing the coincidence spectra gated on the 583 keV transition before and after unfolding. Upper limits on the excitation probability as a function of energy of the 2-phonon members in this case are extracted using the "unfolded" coincidence spectra gated on the 2614 & 583 keV transitions. Those limits (as a function of energy) are extracted from this coincidence spectrum in the following manner: the yield in a 400 keV energy bin centered around the desired energy is measured and normalized to the intensity of the $3^- \rightarrow 0^+$ transition. This yield was measured assuming two different scenarios. First, the hypothesis is made that there are still two components to the γ-ray spectra in the region of interest: γ rays associated with the decay out of the multiplet and those associated with the first steps of the decay of the nucleus. The later γ rays correspond to the decay towards the yrast line of excited states fed in the complex reactions taking place. Somewhat arbitrarily, the two components in the spectrum where associated one with the "grass", i.e. the fluctuations in counts from channel to channel, and the other with a smooth background drawn through the region of interest. In the second scenario, all the counts remaining after unfolding are proposed to be associated with the γ rays of interest. The upper limits extracted using both approaches are presented in Figure 5.23. For obvious reasons, the upper limits for such range of

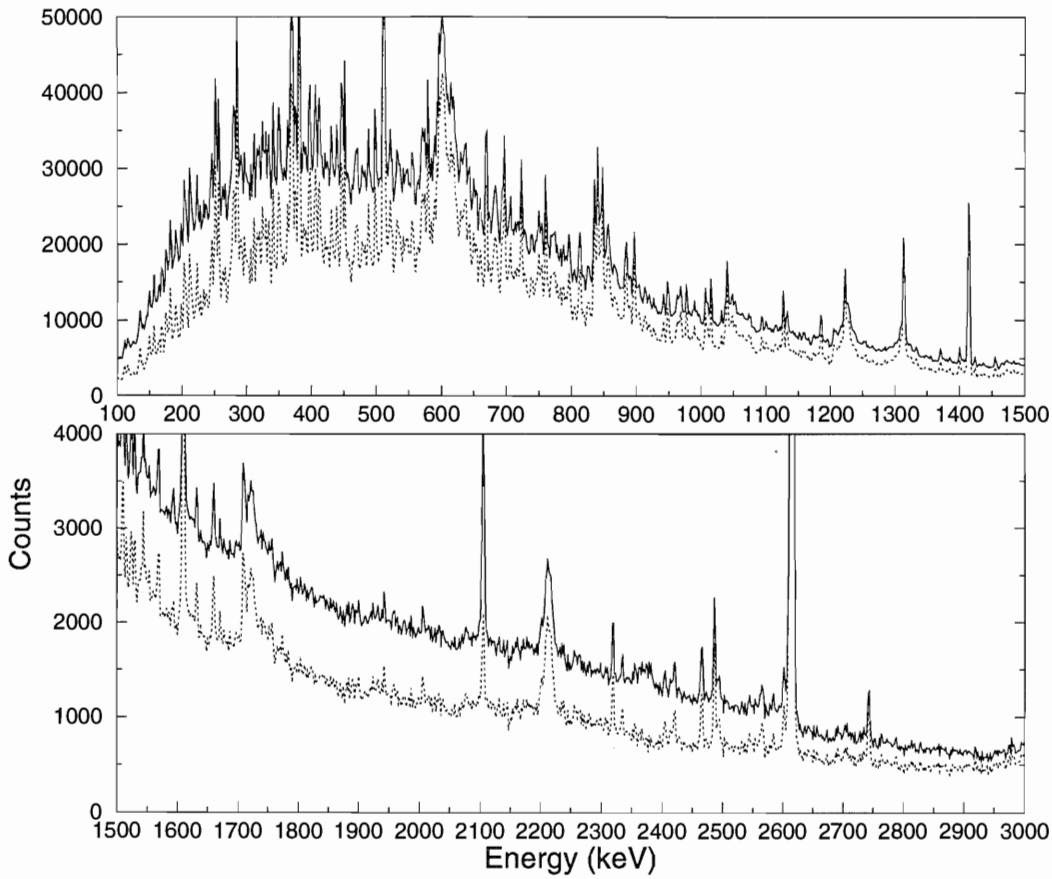

Figure 5.22 The coincidence spectra gated on the $5^- \rightarrow 3^-$ transition before (upper solid line) and after (lower dotted line) unfolding. The effect of "unfolding" is clearly illustrated in this figure.

lifetimes, as extracted from this measurement, are not of great significance.

5.5 Results From The Thin Target Data

Due to the fact that this data set was analyzed and later published by our collaborators at Berkeley [Vet98], the results will be only briefly reviewed in this section.

LBNL measurements were designed to populate members of the 2-phonon multiplet (in particular the 6^+ and the 4^+ levels) in the ^{208}Pb nucleus by "pure" electro-magnetic, Coulomb excitation using a ^{136}Xe beam and a thin ^{208}Pb target. While the thick target measurement was designed to enhance the probability of populating members of the 2-

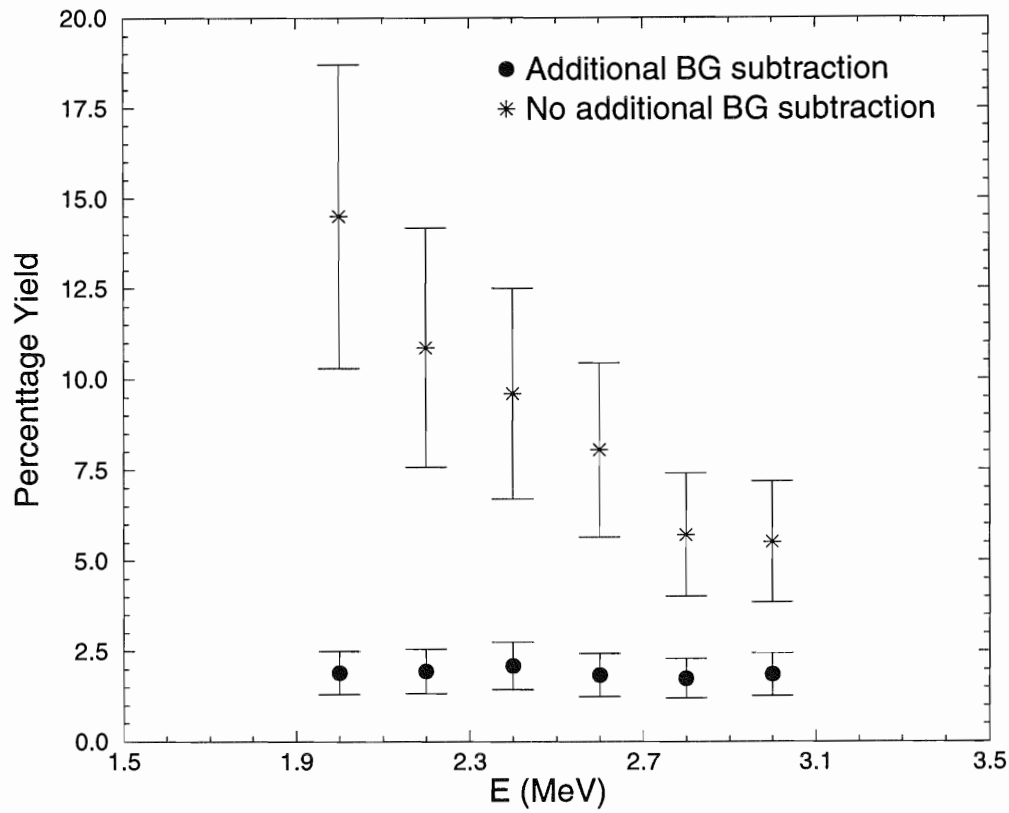

Figure 5.23 Upper limits on the excitation probability as a function of energy of the 2-phonon members. The • symbol represents limits extracted assuming a smooth background under the yield in the region of interest. On the other hand, the $*$ symbol represents limits extracted with no additional background subtraction.

phonon multiplet by using a beam energy 20% above the Coulomb barrier (i.e. where the nuclear interaction is calculated to enhance population of these states), this thin target measurement was performed at a beam energy 7% below the barrier where "pure" Coulomb excitation dominates and nuclear interactions are negligible. Clearly, the cross section for populating members of the 2-phonon multiplet will be lower in this case. However, since the electro-magnetic interaction is well understood, it is then possible to either extract, from the measured absolute field, the $B(E3)$ matrix elements for members of the multiplet (if these states are observed) or to place sensitive limits on their existence (if they are not observed). Gamma rays were detected with Gammasphere, and the CHICO array of position-sensitive gas counters was used for the detection of scattered particles. In this measurement, p-p-γ-γ and p-p-γ (coincident scattered charged particles, p, and γ rays) events were recorded. The data were sorted into the following matrices: (i) $\gamma - \gamma$ coincidence matrices (Doppler corrected for target-like particles), (ii) 15 scattering-angle-dependent γ-ray histograms, and (iii) six $\gamma - \gamma$ matrices (incremented for the sum of all scattering angles and events restricted to only forward scattering angles, using target-target, target-projectile, and projectile-projectile Doppler corrections (using information from CHICO array).

Coincidence spectra gated on transitions in ^{208}Pb were then constructed such as the spectrum gated on the $5^- \rightarrow 3^-$ transition. This spectrum is then searched for the decay from the 6^+ and the 4^+ members of the 2-phonon multiplet as well as from all the 6^+ levels in ^{208}Pb (five 6^+ states exist in this nucleus at excitation energies of 5.213 MeV, 5.738 MeV, 5.993 MeV, and 6.332 MeV). No transition that could correspond to the decay from either member of the multiplet could be identified in this spectrum. Furthermore, no state close in energy to 5.2 MeV (the expected energy of the 2-phonon multiplet within the harmonic limits) was populated and none of the previously known 6^+ states with excitation energies above the 5.2 MeV was observed. Only the 6^+ state at 4.424 MeV was seen in the data. It was found to be populated with a $B(E3)$ value which is about 20% of the calculated total $B(E3)$ strength (the theoretical $B(E3)$) strength expected for a pure harmonic octupole vibration). Therefore, only upper limits as a function of excitation energies on

the $B(E3, 6^+ \rightarrow 3^-)$ values for the 6^+ states in ^{208}Pb were obtained by combining results from the Coulomb excitation calculations (using the computer code GOSIA [Czo91]) and the observed intensity limits. These limits suggest a large fragmentation of the strength of the octupole mode of vibration of the two-phonon states in ^{208}Pb. Furthermore, these results are clearly in agreement with the finding reported above in the case of the thick target measurements.

5.6 New Transitions in ^{208}Pb and ^{207}Pb

Because the data required to obtain significant limits on the intensity of members of the double octupole multiplet have to be of very high statistics, it was also possible to obtain information on new transitions from high-spin states in both the ^{208}Pb and ^{207}Pb nuclei. These new transitions in ^{208}Pb decay from high spin states located above the known 10^+ isomer ($t_{1/2}$ = 500 ns). Their energies, along with the relative intensities (i.e. relative to the $3^- \rightarrow 0^+$ transition), are listed in Table 5.5. Several coincidence spectra were constructed by gating on various combinations of these transitions in order to establish their coincidence relationships. This is illustrated in Figure 5.24 (this coincidence spectrum is constructed by gating on the 341 & 291 keV γ rays). From these coincidence relationships and from intensity considerations, the new transitions were placed in the partial level scheme of the ^{208}Pb nucleus given in Figure 5.25. As is clear from this figure, the 2318, 291, 947, 1019, and the 1588 keV γ rays form a cascade of transitions which link newly found levels. This cascade decays directly into the 14^- level (i.e. the highest spin state known previously in ^{208}Pb). On the other hand, the 1508 keV, $14^- \rightarrow 11^+$ transition, (i.e. an $E3$ transition) and the 1554 keV, $13^- \rightarrow 10^+$, γ ray link levels established previously in the ^{208}Pb nucleus. Finally, the 1232, 1284, and the 1579 keV γ rays are deexcitations from other unknown states to the known 14^- and 13^- states with no link to the cascade on top of the 2318 keV γ ray. No indications for other γ rays above these transitions could be found. The spin and parities of the new states reported here have not been established directly from a correlation analysis. However, tentative values for these quantum numbers can be proposed on the basis of theoretical considerations. It should be noted that most

of the new transitions presented here have also been seen in another study performed concurrently in Europe [Bro96].

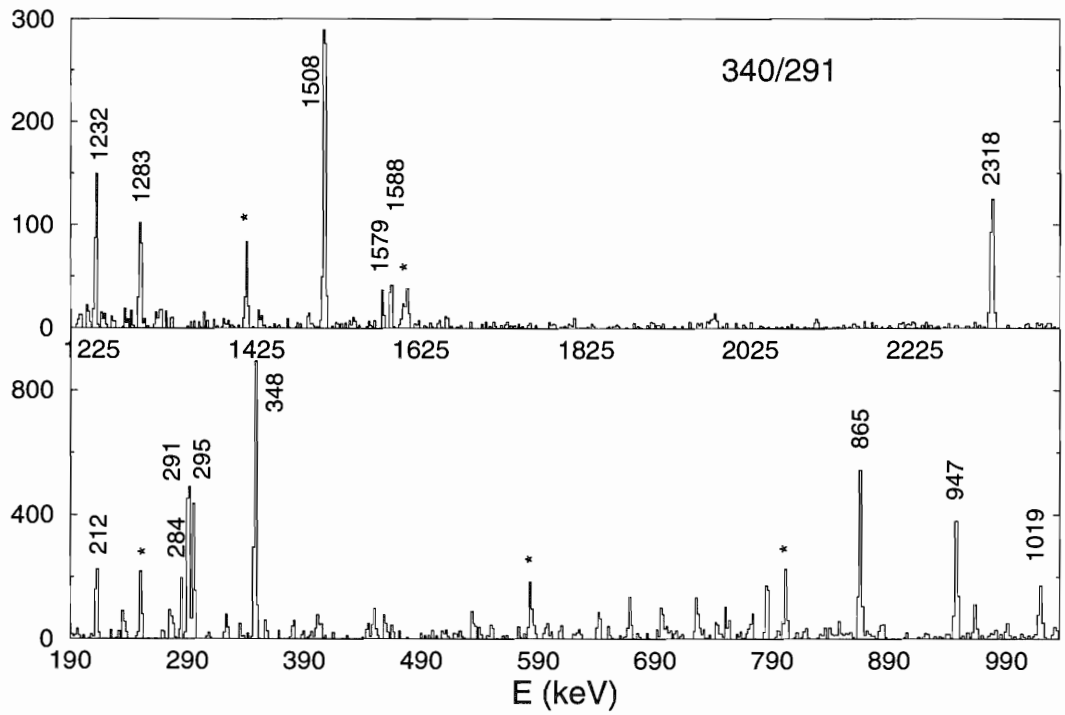

Figure 5.24 Coincidence spectra gated on the 341 & 291 transitions in the ^{208}Pb nucleus. All γ rays that corresponds to a decay from a high spin state (above the isomeric 10^+ state) are labeled. The $*$ symbol labels transitions corresponding to a decay from states below the 10^+ isomer.

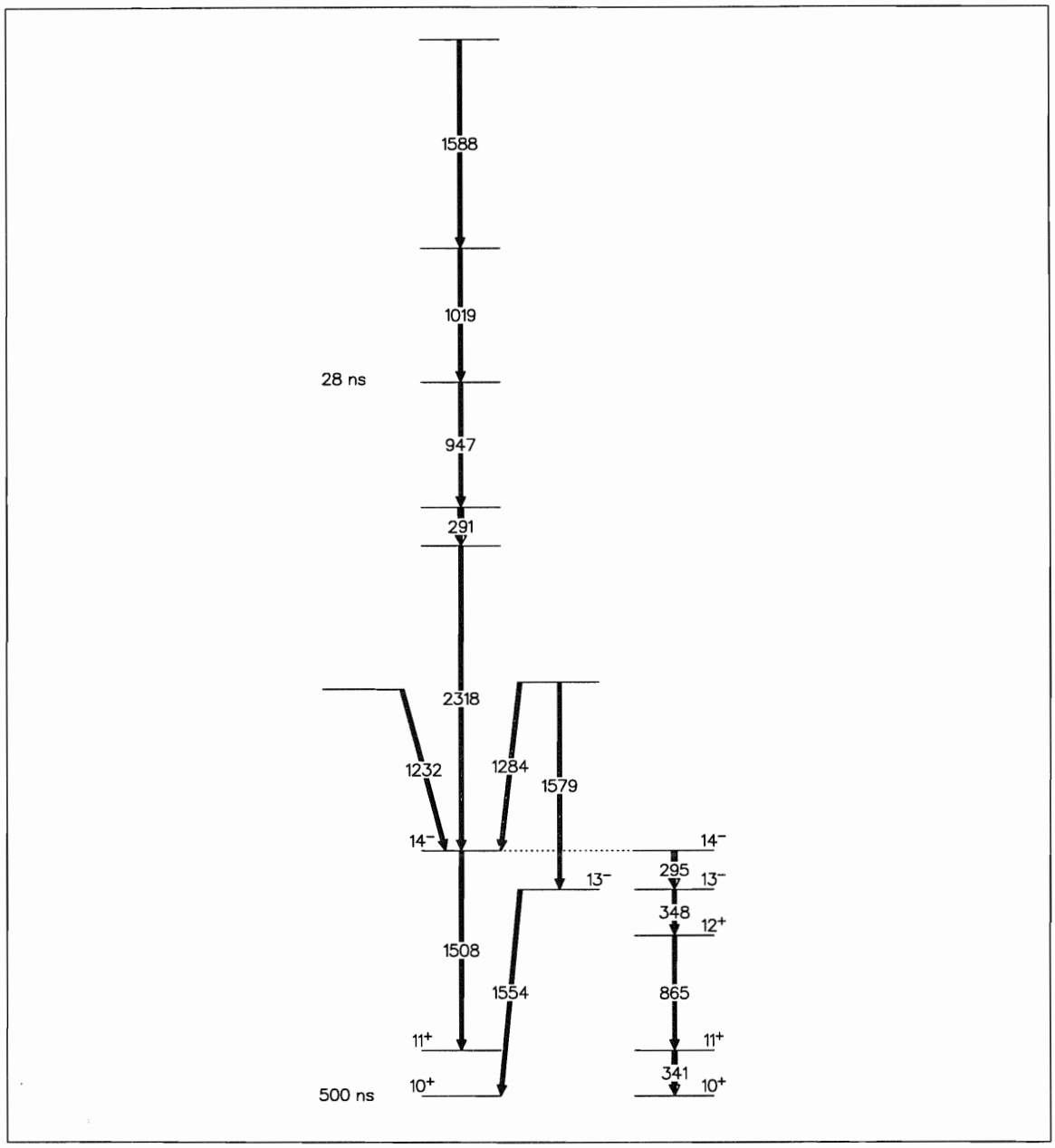

Figure 5.25 Partial level scheme showing the new transitions in the ^{208}Pb nucleus. The cascade of transitions on the right (i.e. the 295, 348,865, and 341 keV γ rays) are previously known transitions in the ^{208}Pb nucleus, shown for completeness.

E_γ (keV)	Relative intensity
1588	0.03 ± 0.0034
1019	0.06 ± 0.0062
947	0.10 ± 0.012
291	0.10 ± 0.013
2318	0.11 ± 0.02
1284	0.047 ± 0.005
1579	0.02 ± 0.0021
1232	0.05 ± 0.006
1508	0.17 ± 0.028
1554	0.025 ± 0.003

Table 5.5 List of the all the new transitions in ^{208}Pb nucleus. The intensities of these transitions are normalized to the intensity of the $3^- \rightarrow 0^+$ (2614 keV) transition.

A similar analysis was carried out for new transitions in the ^{207}Pb nucleus. Table 5.6 lists the energies and the relative intensities (normalized to the intensity of the total yield feeding the $(19/2^-)$ level) of these transitions. Once again, from coincidence relationships (as is illustrated in Figure 5.26) and from intensity considerations the new transitions were placed in the partial level scheme of the ^{207}Pb nucleus. This scheme is presented in Figure 5.27. It is clear from this figure that two branches feed the $(29/2^+)$ level, a weak branch (1569 and 939 keV γ rays) which accounts for only 6% of the total yield feeding this state, and a stronger one (696, 987, and 366 keV γ rays) accounting for 24% of that yield. All five new transitions decay from levels in the ^{207}Pb nucleus that had not been established in earlier work. As in the case of ^{208}Pb, the spins and parities of the levels are not known. It should noted that similar results have been reported independently in reference [Bro96] for the ^{207}Pb nucleus.

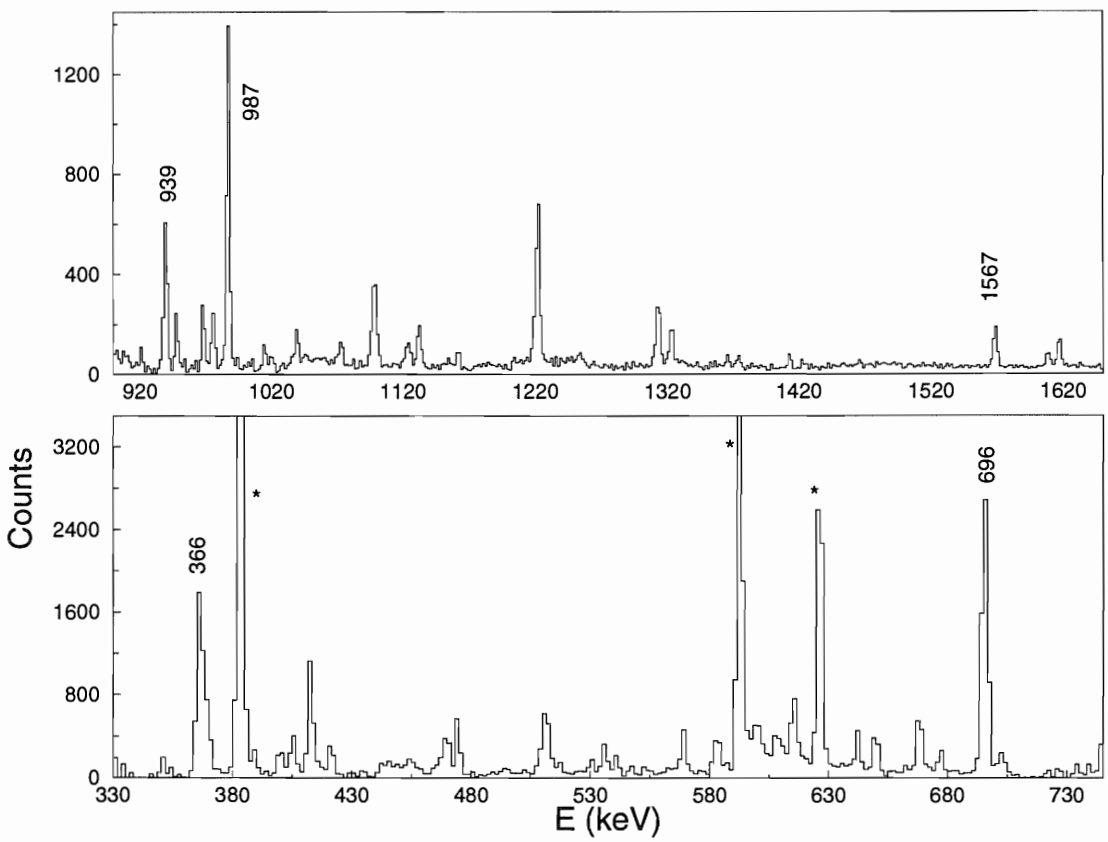

Figure 5.26 Coincidence spectrum gated on the 2485 keV transition in ^{207}Pb. All new transitions are labeled. The $*$ symbol indicates previously known transitions in this nucleus.

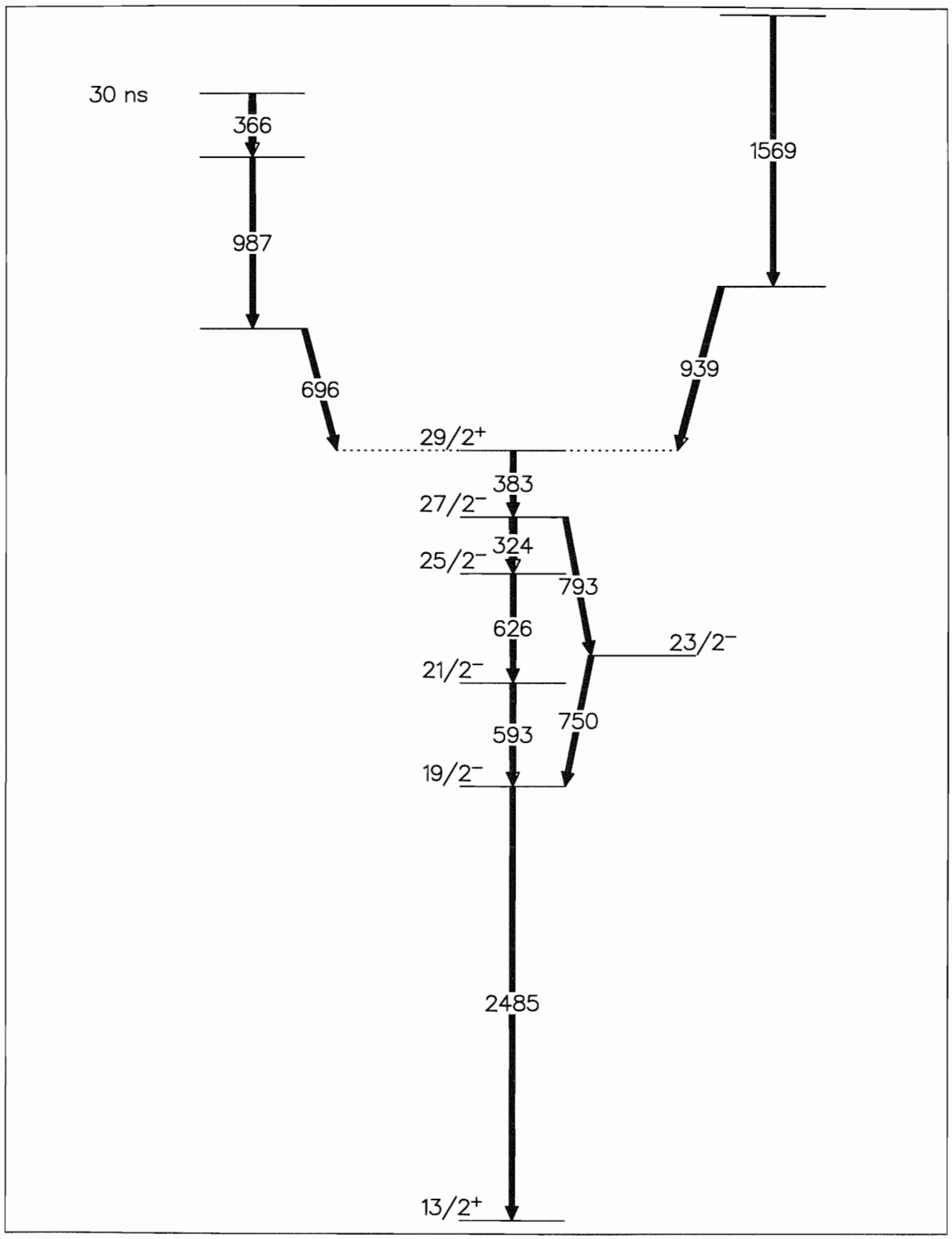

Figure 5.27 Partial level scheme showing the new transitions in the ^{207}Pb nucleus, i.e. transitions on top of the $29/2^+$ level.

E_γ (keV)	Relative intensity
696	24±2.4
987	13±1.6
366	9±1.1
939	6±0.76
1567	3±0.41

Table 5.6 List of the all the new transitions in ^{207}Pb nucleus. The intensities of these transitions are normalized to the intensity of the of the total yield feeding the $(19/2^-)$ level. The assignment of those γ rays has been verified from coincidence relationships.

Chapter 6

Interpretation

This chapter is devoted to the discussion of the results from the present work on the search for members of the two-phonon octupole vibration multiplet in the ^{208}Pb nucleus. In addition, a discussion of relevant recent results [Yeh96, Yeh98, Vet98, Pon99] obtained elsewhere is also presented. All the available information, experimental as well as theoretical, is then used in an attempt to provide some insight into the possible mixing of double-phonon octupole excitations with other types of excitations in the ^{208}Pb nucleus.

As discussed earlier, the first excited level in ^{208}Pb has long been interpreted as a one-phonon octupole vibrational state. This interpretation is based mostly on the low excitation energy and the large $B(E3)$ transition probability which both point to the collective nature of this state. Within this vibrational picture, the existence of a double-phonon octupole vibration is, of course, naturally expected. In a pure harmonic description, a two-phonon excitation will be located at twice the excitation energy of the one-phonon state (i.e.,$\sim$5.228 MeV in the case of ^{208}Pb). An unambiguous identification of a 2-phonon octupole excitation, in a pure harmonic picture, will follow from the observation of the following experimental quantities; (i) an enhanced $B(E3, (2-phonon)_{state} \rightarrow 3^-)$ transition probability, since this quantity provides a direct measure of the collectivity, and (ii) the excitation energy, since this is linked directly to the harmonicity of the vibration. It should be stressed that without measuring these two quantities a 2-phonon octupole excitation cannot be unambiguously identified.

However, looking at precisely twice the energy of the one-phonon excitation is not sufficient. Indeed, various theoretical calculations [Blo70, Bro71, Ham74] indicate that deviations from the pure harmonic picture should be expected. These calculations suggest the following deviations: (i) a shift in the excitation energy of the 2-phonon state from the unperturbed excitation energy of twice that of the one-phonon (i.e. ~5.23 MeV) that is estimated by different theoretical calculations; on the average, the estimated shift predicted by theory is in the order of ~200 keV; (ii) a splitting of the the two-phonon octupole vibrational states into a multiplet of levels; i.e. $3^- \otimes 3^-$:$0^+, 2^+, 4^+, 6^+$. This departure from the pure harmonic picture is understood as being due to: (i) the coupling of the octupole vibration to a particle vibration [Ham74] and/or to (ii) the interaction with the 2-phonon pairing vibration modes [Blo70, Bro71, Cur88], and (iii) the coupling between the octupole and the quadrupole modes of vibrations [Blo70] (inferred from the observed large intrinsic quadrupole moment of the one-phonon state, $Q(3^-) = -0.34 \pm 0.15\ b$ [Spe83]).

Due to the splitting of the 2-phonon octupole state, it becomes important to view all the possible and most favorable decay paths from members of the 2-phonon multiplet. Except for the 0^+ member of the multiplet, where the $0^+ \rightarrow 3^-$ decay via an $E3$ transition is expected, decays with transitions of lower multipolarities, e.g. $E1$, $M1$ or $E2$ transitions, may now be involved for the other multiplet members. First, the deexcitation from the 6^+ level to the 3^-, 1-phonon, state via an $E3$ transition is unlikely, since this state can reach the 5^- level at 3197 keV via an $E1$ transition which can be much faster. decay from the 4^+ member of the multiplet could follow either the $4^+ \rightarrow 3^-$ or the $4^+ \rightarrow 5^-$ paths, again via $E1$ transitions. first path is more favorable, particularly in view of the energy factor; i.e., $E_{4^+ \rightarrow 3^-} = 2614$ keV and $E_{4^+ \rightarrow 5^-} = 2031$ keV. Finally, the $2^+ \rightarrow 3^-$ decay path for the 2^+ member of the multiplet via an $E1$ transition will compete favorably with the $2^+ \rightarrow 5^-$ decay via an $E3$ transition. In the literature, such $E1$ transitions which correspond to deexcitations from members of the 2-phonon octupole multiplet, are often referred to as "octupole $E1$ transitions", indicating that they correspond to the destruction of an octupole phonon. As discussed in the previous chapter, in the present work, all three measurements (two with a thick target and one with a thin target) carried out to search

for members of the 2-phonon multiplet in ^{208}Pb yielded negative results: not a single γ ray was identified that could be considered as a candidate for the deexcitation of any member of the multiplet. In the thick target measurements, the calculated excitation probability for members of the multiplet had to be folded in with results from line-shape simulations. It was shown that deexcitation from the 6^+ member of the multiplet should occur with an intensity corresponding to a few percent of the strength of the $3^- \rightarrow 0^+$ transition (see Figure 6.1). This is clearly within the detection sensitivity of the experiment. Similarly, the sensitivity should have been sufficient to allow for the identification of the 4^+ level and, perhaps, even the 2^+ state. However, upon searching the region of interest in the relevant coincidence spectra, no sharp peak was found. Clearly, this finding could suggest that the state-lifetimes for members of the 2-phonon octupole multiplet are much shorter than anticipated (i.e. they are calculated to be of the order of a few *ps* but would be shorter-lived for some reason). As a result, the γ rays deexciting these states would then undergo severe Doppler shifts and/or broadenings and the observation of a stopped component would be severely hampered. However, in the case of the thin target measurement, where the observation of a γ ray corresponding to the decay from any member of the multiplet is independent of the state lifetime, negative results were obtained as well. Again, no candidate for any member of the 2-phonon octupole was observed. This is a particularly surprising result since the calculated population rates for these 2-phonon members are about an order of magnitude higher than the sensitivity of the γ-ray array used in these measurements (Gammasphere). In view of the absence of sharp peaks, only upper limits on the probability of populating members of the multiplet were extracted. In the case of the thick target measurements, the extracted upper limits are lifetime dependent and the results are summarized in Figure 6.2. In the case of the thin target experiment on the other hand, lifetime-independent upper limits were extracted for the excitation probabilities of all 6^+ states known in ^{208}Pb as shown in Figure 6.3. It is worth pointing out that this experiment provided one surprising result which is relevant in the present context: the $B(E3 : 6^+ \rightarrow 3^-)$ value for the lowest 6^+ state at 4.424 MeV was found to be about 20% of the total $E3$ strength expected in a 2-phonon octupole excitation.

These negative results cast serious doubts on the existence of a "pure" two-phonon octupole excitation in ^{208}Pb. In this context, "purity" refers to the extent in which the states of interest remain distinct (i.e. no mixing) from other excitations in ^{208}Pb. It seems clear that "pure" octupole states, i.e. distinct, specific levels isolated from all other states by their enhanced collective character, are not present in this nucleus. It is time then to contemplate the possibility that these levels may have interacted and mixed with other states of roughly the same excitation energy, i.e. that the octupole character might have been diluted to a large degree. This could then explain how the lowest 6^+ level, which has been interpreted originally as a mixture of a $(\nu g_{9/2})(\nu i_{13/2})$ and a $(\pi h_{9/2})(\pi h_{11/2})$ particle-hole excitation [Mar87, Sch97], could carry a degree of collectivity. At this point, before elaborating further on this suggestion of significant mixing, it is important to introduce very recent results obtained with another technique.

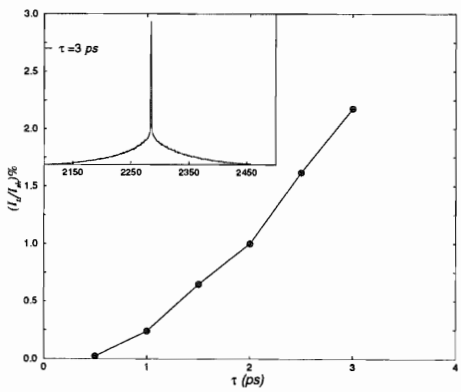

Figure 6.1 The expected strength for the stopped component of the 6^+ relative to the $3^- \rightarrow 0^+$ transition as a function of the state lifetime. The insert shows the line shape for the γ ray deexciting the 6^+ member of the 2-phonon multiplet for a lifetime of 3 *ps*. This figure is discussed in more detail in the preceding chapter.

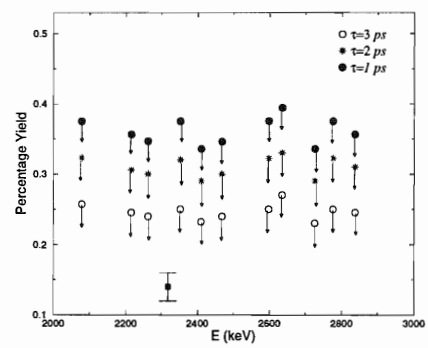

Figure 6.2 Upper limits, as a function of energy, on the sharp component of the total yield of the γ ray decaying out of 6^+ member of the multiplet. se limits are extracted assuming different state lifetimes and are normalized to the $3^- \rightarrow 0^+$ transition in ^{208}Pb nucleus. relative intensity of the 2318 keV γ ray in ^{208}Pb is presented in this figure for illustration purposes (see previous chapter for further details)

Inelastic neutron scattering, $(n, n'\gamma)$, was used by a group at the University of Kentucky

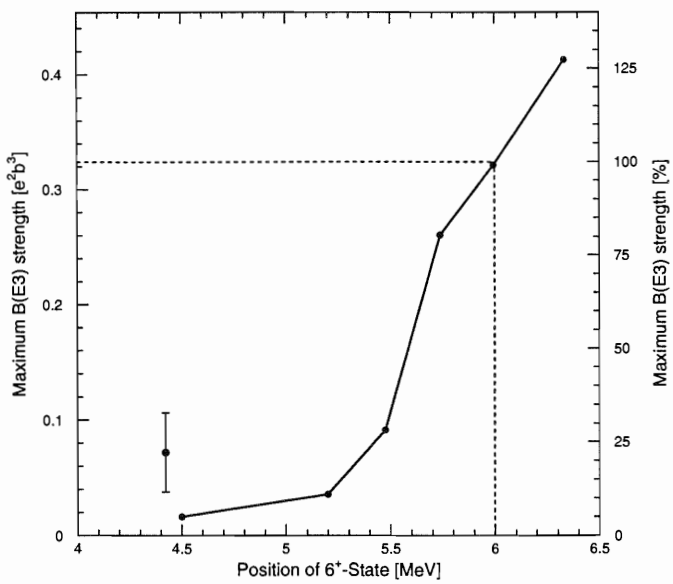

Figure 6.3 Limits on the $B(E3)$ values of the 6^+ states in ^{208}Pb obtained by combining experimentally observed intensity limits and multiple Coulomb excitation calculations as a function of the excitation energy of the 6^+ state. strength limits are also given relative to theoretical values expected for a pure harmonic octupole vibration. In addition, the $B(E3)$ value obtained for the only observed 6_1^+ state at 4.424 MeV is shown. given error follows from the assumption that the maximum 6_1^+ decay intensity is determined only by the direct population of this state, and the minimum by considering the feeding according to the observational limits from the next two higher 6^+ states [Vet98].

to search for the 2-phonon octupole excitations in ^{208}Pb. From this work, Yeh *et al.* [Yeh96, Yeh98] proposed a set of levels with energies close to the theoretical expectations for the 2-phonon multiplet members. first measurement [Yeh96] provided the most promising experimental evidence identifying a candidate for the 0^+ member of the 2-phonon octupole multiplet. Indeed, a 5241 keV level was observed and assigned 0^+ quantum numbers. most compelling evidence for the assignment of this level to the double-octupole phonon is the observation of a cascade of two $E3$ transitions of energy 2626 and 2614 keV, which could correspond to the sequence $0^+ \rightarrow 3^- \rightarrow 0^+_{g.s}$. Furthermore, the observed angular distribution of the 2626 keV γ ray is consistent with the assigned zero spin for the 5241 keV level. No Doppler shift was seen for the 2626 keV γ ray, indicating a lifetime of this state $\tau > 1$ *ps* (the expected lifetime is $\gg 1$ *ps*). absence of other decay branches competing with the 2626 keV γ ray was taken as an important indication of the collective nature of the $0^+ \rightarrow 3^-$ decay. As this evidence stands, it can be viewed as the most

promising assignment of a member of the 2-phonon multiplet, but more measurements are desirable. In particular, a polarization measurement to determine the parity of this level is certainly needed. experiment only confirmed the spin of this state to be zero (i.e. there is no direct proof that the decay proceeds via a $E3$ transition, although $M3$ radiation is admittedly unlikely). Furthermore, measuring the lifetime of the 0^+ state would allow the determination of the $B(E3 : 0^+ \rightarrow 3^-)$ value, which provides a direct measure of the degree of the collectivity.

In the second measurement [Yeh98], possible candidates for the 4^+ and 2^+ members of the 2-phonon multiplet were proposed. The assignments are based on the observation of enhanced $E1$ decays from the observed levels to the 1-phonon, 3^-, octupole state in ^{208}Pb. Since it has been observed in the $N = 82$ region [Gat90, Bel95] that octupole-coupled states decay by "fast" $E1$ (referred to as "octupole $E1$") transitions, such $E1$ decays are naturally expected to occur from the $2^+, 4^+$, and 6^+ members of the 2-phonon octupole multiplet. Therefore, a comparison of $B(E1)$ values measured in ^{208}Pb with those of similar "octupole $E1$" transitions in odd-A nuclei, such as ^{207}Pb and ^{209}Bi was made (in these nuclei, collective octupole excitations arise from the weak particle-vibration coupling of single-particle (or hole) configurations to the 3^- octupole vibrational state in the ^{208}Pb core). This comparison revealed that $E1$ decays in ^{207}Pb and ^{209}Bi, which result from the destruction of an octupole phonon, have transition rates that are similar to the $E1$ rates for decays from the proposed 4^+ and 2^+ members of the 2-phonon octupole multiplet in ^{208}Pb. This is illustrated in Figure 6.4. From the figure it is, however, clear that an argument based on the $E1$ rates remains quite weak as other $E1$ transitions, not associated with octupole excitations, have rates which are comparable to those of interest here. No candidate for the 6^+ member of the multiplet was proposed. Candidates for members of the 2-phonon octupole (from both measurements by Yeh *et al.*) are summarized in Figure 6.5. It is certainly striking that the 4^+ and 2^+ members of the multiplet, as proposed by Yeh *et al.*, are located at energies close to expectations based on a pure harmonic picture. At first glance, the observation of these states does not seem to be in accord with the results discussed in the present thesis from both the thick and thin target measurements.

However, the validity of proposing candidates for the 4^+ and 2^+ members of the multiplet based solely on the observation of enhanced $E1$ decays from these states to the 1-phonon level needs to be critically examined, as was done recently by Ponomarev *et al.* [Pon99]: this is discussed further below.

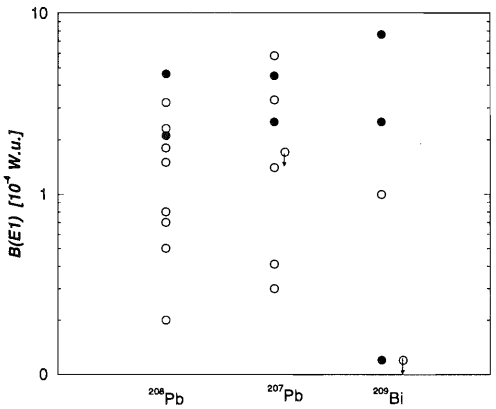

Figure 6.4 $E1$ transition strengths in ^{208}Pb, ^{207}Pb, and ^{209}Bi. Transitions from 2-phonon candidates in ^{208}Pb are represented as filled symbols, while other $E1$ transitions in ^{208}Pb references [Yeh96, Yeh98] are shown as open symbols. For comparison, $B(E1)$ values from the $3^- \bigotimes f_{5/2}^{-1} \rightarrow f_{5/2}^{-1}$ transitions in ^{207}Pb (filled symbols), $3^- \bigotimes h_{9/2} \rightarrow h_{9/2}$ transitions in ^{209}Bi (filled symbols) and other transitions (open symbols) in these nuclei are also shown. Most of the $B(E1)$ values for transitions in ^{207}Pb and ^{208}Pb are from references [Yeh96, Yeh98].

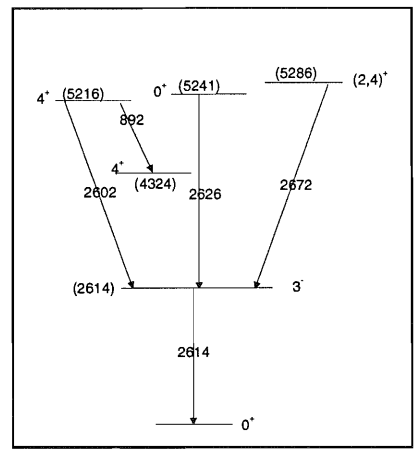

Figure 6.5 Candidates for the two-phonon octupole states in ^{208}Pb as suggested by Yeh *et al.* [Yeh96, Yeh98].

At this point it becomes essential to further explore the possibility that the members of the 2-phonon octupole multiplet might be fragmented. While the previous theoretical calculations regarding the 2-phonon octupole excitations in ^{208}Pb mainly focused on the

anharmonicity of such excitations relative to the 3^- state [Blo70, Bro71, Ham74], only recently, the energy shifts as well as the "purity" of members of the two-phonon multiplet have been examined in an attempt to provide an explanation to the surprising experimental results [Pon99]. The properties of the 2-phonon octupole vibrational states were studied within the quasiparticle-phonon model (QPM) described in detail in reference [Sol92]. The model Hamiltonian includes terms corresponding to the mean field for neutrons and protons, monopole pairing and residual interactions. The calculations were performed with wavefunctions for excited states including all relevant 1p-1h, 2p-2h, 3p-3h and 1-phonon configurations in the low-energy spectrum of ^{208}Pb. Excitation energies below 7,9, and 12 MeV were included for 1p-1h, 2p-2h, and 3p-3h configurations, respectively. All 2p-2h and 3p-3h states resulting from pure, non-collective configurations were neglected in the calculations since they couple very weakly to other configurations. Their omission does not affect the final results for the states under consideration here. Whenever possible, experimental values were used in the calculations. This is the case for the energy gap between particles and holes, the strengths of the residual interactions, and the single particle energies. The physical properties of phonons (the term phonon is used in the QPM model to refer to any solution of the RPA, surface vibrations are refered to as collective phonons), their excitation energy, and their internal fermion structure was obtained by diagonalizing the model Hamiltonian in the random phase approximation (RPA). The diagonalization of the model Hamiltonian with the full model space for a given spin and parity, λ^π, yields a set of excited states λ^π_ν where the index ν denotes the ordering by increasing excitation energy. In order to test the approach used in the calculations, the properties of the first excited states in ^{208}Pb, i.e. the 3^- and 5^- levels, were reproduced. The calculated excitation energies and transition strengths were found to be in good agreement with experiment. The properties of the members of the 2-phonon multiplet, $[3^- \otimes 3^-]_{6^+,4^+,2^+,0^+}$, (including the energy shift and fragmentation induced by the interaction with the full model space of 1p-1h, 2p-2h, and 3p-3h configurations) were calculated. The calculations concluded the following regarding the "purity" of members of the 2-phonon multiplet: (i) the 0^+ remains unaffected (i.e. little mixing) due to the fact that its excitation energy is well

below that of any other excitation (i.e. particle-hole configurations) expected to mix with the 2-phonon excitations, (ii) the 4^+ also remains practically pure, because mixing with other particle-hole configurations is calculated to be weak, (iii) the 2-phonon octupole configuration is distributed over the lowest three 2^+ states present in the vicinity of the 2-phonon octupole levels, however, about 75% of the total 2-phonon strength remains in a state at 5.29 MeV, finally, (iv) the 6^+ state mixes with practically all 1p-1h, 2p-2h, and 3p-3h configurations, therefore, its strength is fragmented over an energy region of about 2 MeV.

In general, the results of the calculations seem to be in accord with the experiment. For the first time, a calculation provides a theoretical explanation for the failure to observe the 6^+ member of the 2-phonon octupole multiplet since it is found to be highly fragmented. This is clearly in agreement with the results from the present work where it has been concluded (i) that there is no single 6^+ state carrying the expected yield , but (ii) from the thin target measurement that the lowest 6^+ state in ^{208}Pb carries about 20% of the total strength of the $B(E3)$ rate expected in a 2-phonon octupole excitation (in the harmonic picture). In addition, the calculations are in agreement with the results from reference [Yeh96] regarding the proposed candidate for the 0^+ member of the multiplet, since it is predicted by the calculations to be a pure 2-phonon octupole state.

The situation is somewhat less clear for the 2^+ and 4^+ members of the double-phonon octupole multiplet. The QPM calculations strongly suggest that large $E1$ transition rates cannot be regarded as a unique signature for the decay of states associated with the double octupole phonon. Indeed, some particle-hole excitations are calculated to decay with $E1$ transitions of comparable strength and this finding is also confirmed by experiment (see Fig. 6.4). Thus, there is little basis to associate the 2^+ state reported by Yeh *et al.* [Yeh98] with a double octupole phonon excitation. This argument is reinforced by the fact that the calculations also predict some fragmentation of the 2-phonon octupole strength which leaves even less justification to make a correspondence between the observed 2^+ level and a double octupole 2^+ state. The calculations indicate that the 4^+ member of the multiplet is hardly mixed with any level and remains relatively pure. This result of the calculations

would then be in clear contradiction with the experimental findings described in the present work. In the absence of mixing, the Coulomb excitation measurements should have found the γ ray associated with the decay of the 4^+ level. However, at this stage, it is the results of the calculations that appear somewhat surprising. It is relatively easy to understand why the 0^+ double phonon level remains pure (it is simply very difficult to construct 0^+ states of low excitation energy from p-h configurations, and other collective excitations such as proton pairing vibrations are characterized by wavefunctions without significant overlap with the octupole vibration), and why only few 2^+ levels can mix. However, on general grounds, the density of 4^+ and 6^+ levels can be expected to be large and mixing should occur. No explanation for the lack of mixing is suggested in ref. [Pon99] and one is left to wonder whether this lack of mixing is purely accidental, i.e. whether it is possible that slightly different input parameters in the calculations would lead to a different conclusion. Thus, it is still possible that mixing can account both for the negative result of the measurements reported in this thesis (i.e. the $E3$ strength is again spread over many levels) and the positive result of Yeh *et al.* [Yeh96].

Based on the present discussion, a somewhat clearer picture appears to emerge. The results discussed in this thesis demonstrate unambiguously that well isolated levels (beyond the 0^+ level), carrying the strength expected for a double-phonon octupole vibration do not exist in the experimental spectrum of ^{208}Pb. Rather, the results are consistent with a picture where the octupole character is severely diluted through interactions with other excited states. A possible task for future studies would then be the complete spectroscopy of the ^{208}Pb nucleus in the region of interest. Such a study would lead to the identification of the many levels over which the octupole strength is spread. However, because of the sizable mixing, there is no longer a specific character to associate with any particular state. The very picture of a "simple" double-phonon octupole excitation has in fact disappeared, i.e. the implicit beauty of a "simple" octupole vibrational mode has vanished.

Summary and Conclusions

The aim of the present work was to examine two of the many facets associated with octupole degrees of freedom in nuclei. In the first part of the thesis, it was shown that at the extreme prolate deformations associated with a superdeformed well, octupole effects can still play a decisive role. By measuring the lifetimes of the states in the yrast and in the first excited superdeformed bands of ^{190}Hg, it was unambiguously established that the dipole transitions linking the two bands are associated with enhanced $B(E1)$ transition rates reminiscent of those observed in nuclei of the actinide region where strong octupole correlations are present. It was also shown that the deformations associated with the two bands are the same, despite the fact that the respective dynamic moments of inertia are very different. All these results have been explained satisfactorily in RPA calculations which treat the octupole degrees of freedom explicitly.

Prior to this work and that of Hackman *et al.* in ^{194}Hg [Hac96], there was considerable debate about the nature of excited bands in the $A = 190$ region of superdeformation. One school of thought interpreted the many bands that had been observed as quasiparticle excitations. A number of calculations with different mean field techniques such as the cranked shell model or the Hartree Fock Bogoliubov approximation managed to reproduce most of the observables satisfactorily. The other interpretation proposed that most of the excited bands could be associated with the various components of the octupole phonon. With the present work and that of ref. [Hac96], the latter interpretation is now validated. Indeed, within the quasiparticle picture, it is hard if not impossible to account for the low excitation energies of the excited superdeformed bands as well as for the large transition rates. Also, the peculiar moment of inertia of the excited superdeformed band in

^{190}Hg, which was so difficult to reproduce in the quasiparticle approach, finds a natural explanation within the RPA framework described above.

The present work highlights the similarity between the excitation spectra of the superdeformed nuclei of the $A = 190$ region and those of normal deformed nuclei of the rare earth and actinide regions: rotational bands built on octupole vibrations appear at low excitation energy. This finding can, however, not be generalized to the other regions of superdeformation. Only in the $A = 190$ region does superdeformation occur in a regime where pairing still dominates (i.e. low rotational frequencies). As a result, the quasiparticle excitations which have to overcome the pairing gap are located at much higher energy and they remain to be found. In other regions of superdeformation, and in particular in the $A = 150$ and $A = 80$ regions, the superdeformed bands are seen only in the frequency domain where pairing is either very small or has vanished all together and the properties of the superdeformed bands are a direct reflection of the specific orbitals being occupied. The presence of collective excitations in these nuclei should not be ruled out. However, in view of the density of available orbitals near the Fermi surface in the superdeformed well, these excitations cannot be expected to carry much of the strength and their discovery remains a formidable experimental challenge.

While the first part of this work found its physics meaning in a positive signal, it is the absence of one that highlights the second part where a longstanding issue in nuclear structure physics was revisited: the existence of double-octupole phonon states in ^{208}Pb. The search for this multiplet of states was prompted by the suggestion that the 6^+ member had been observed in a ^{208}Pb + ^{208}Pb measurement performed at GSI. This experiment was first repeated at the ATLAS accelerator where it was shown not only that the assignment was in error and that the candidate gamma ray originates from ^{207}Pb, but that there was no other viable candidate at least at the level of sensitivity of the detection system being used.

To pursue the issue further, two other measurements were performed with the most sensitive γ-ray detection system available in the world today: Gammasphere. In the first one, the reaction ^{136}Xe + ^{208}Pb was studied at energies 15% above the Coulomb

barrier where the production cross section to the levels of the multiplet with the highest spins is enhanced. This data set, where a thick target was used, was analyzed entirely within the context of the present work. In a second experiment with a thin target ^{208}Pb was investigated once more with the same ^{136}Xe beam, but now at an energy below the Coulomb barrier where the production cross section is purely electromagnetic. The data were analyzed by our collaborators of LBNL. None of these experiments found any candidate for a gamma ray to be associated with the deexcitation of a member of the double octupole phonon multiplet. Moreover, because of the sensitivity of Gammasphere, the upper limits for any possible yield for these states is now so low that the simple picture of a double octupole vibration can now be unequivocally ruled out. Surprisingly, the $B(E3)$ excitation probability to the lowest 6^+ state in ^{208}Pb was found to be larger than expected: it exhaust nearly 25% of the total transition probability.

The full significance of the negative results from the present searches comes to light only when it is considered together with recent measurements performed with neutron scattering at the University of Kentucky. These results were discussed in depth in the preceding chapter. The picture that emerges is one where considerable fragmentation of the double octupole phonon strength occurs because of the large level density available at this excitation energy in ^{208}Pb, i.e. the mixing is so large that at least the 4^+ and the 6^+ members of the double phonon lose their specific identity and, in fact, only the 0^+ level may survive. Interestingly, very recent RPA calculations of ref. [Pon99] reached similar conclusions regarding the fragmentation of the yield. The message is clear: the elegant, simple picture of a vibrational spectrum with multiple phonons breaks down just as soon as the associated excitation energies lie above the pairing gap.

At the conclusion of the present work a few new directions of investigation can be proposed. In the case of the superdeformed ^{190}Hg nucleus, a search for the bands associated with the other components of the octupole phonon is warranted as it would complete the experimental verification of the RPA calculations. The knowledge of the full spectrum of excitations in the second well also requires a new search for quasiparticle excitations. This in turn will also provide insight into the interplay between collective and quasiparticle

excitations. In the case of ^{208}Pb, the situation is less clear although a detailed study of the fragmentation of the $B(E3)$ strength is of interest. It is quite possible that these lofty goals will require detection systems with a higher sensitivity than those presently available: in both nuclei, the γ-ray yields in the new structures can be expected to be at most of the order of 10^{-4} - 10^{-5} of the groundstate yield, e.g. at the very limit of the signals that Gammasphere can detect.

The nucleus remains a fascinating object to study and this thesis represents one of the many attempts to contribute to the exploration of the multiple facets that this many body system has to offer. While much has been discovered, there is no doubt that more surprises lie ahead. As we stand at the edge of the 21st century, the nucleus continues to provide us with wonderful intellectual challenges.

Bibliography

[Abe90] S. Åberg, Nucl. Phys. **A520**(1990)35c.

[Ahm93] I. Ahmad and P. Butler, Ann. Rev. Nucl. Part. Sci 43(1993)71.

[Ang96] G. de Angelis *et al.*, Phys. Rev. **C53**(1996)R679.

[Apr87] A. Aprahamiian *et al.*, Phy. Rev. Lett **59**, (1987)535.

[Bar95] L. Bargioni *et al.*, Phy. Rev. **C51**, (1995)R1057.

[Bea92] I.G. Bearden *et al.*, Nucl. Phys. **A576** (1992)441.

[Bea93] I.G. Bearden, *Detailed Band structures in A=188-190 Mercury Isotopes: Superdeformation and Other High-Spin Excitations*, Purdue University, 1993.

[Bel95] T. Belgya *et al.*, Phys. Rev. **C52**, (1995)R2314.

[Bev69] P.R. Bevington, *Data Reduction and Error Analysis for the Physical Sciences*, McGraw-Hill, New York(1969).

[Bla54] J.S. Blair, Physical Review, **95**(1954)1218.

[Bla52] J.M. Blatt and V.F. Weisskopf, *Theoretical Nuclear Physics*, Wiley, New York(1952).

[Bla66] A.E. Blaugrund, Nucl. Phys. **88**(1966)501.

[Blo70] J. Blomquist, *et al.*, Phys. Lett. **B 33**,(1970)541.

[Boh69] A. Bohr and B. Mottelson, *Nuclear Structure*, Vol 1., Benjamin, New York(1969).

[Bon96] P. Bonche, H. Flocard and P.-H. Heenan, Nucl. Phys. **A598**(1996)251.

[Bon91] P. Bonche *et al.*, Phys. Rev. Lett. **66**(1991)876.

[Bon90] P. Bonche *et al.*, Nucl. Phys. **A519**, (1990)509.

[Bro96] R. Broda *et al.*, *in Proceedings of the Conference on Nuclear Structure at the Limits*, Argonne, Illinois, (1996) (unpublished).

[Bou96] S. Bouneau *et al.*, Phys. Rev. **C53**(1996)R9.

[Bro71] R.A. Broglia *et al.*, Phys. Lett. **B 37**, 159 (1971)159; **B 37**,(1971)257.

[Bur94] D.G. Burke *et al.*, Nucl. Phy. **A569**, (1994)523.

[But96] P. Butler *et al.*, Rev. Mod. Phys. **68** (1996)349.

[Car93] M.P. Carpenter *et al.*, Nucl. Phys. **A557**(1993)57c

[Ced94] B. Cederwall *et al.*, Phys. Rev. Lett. **72**(1994)3150.

[Cha87] R. R. Chasman, Phys. Lett. **B 187**(1987)219.

[Chr77] P. Christensen *et al.*,(unpublished), quoted in Phy. Lett. **B 70**, (1977)229.

[Coh74] S. Cohen *et al.*, Ann. Phys. **82**(1974)505.

[Cro95] B. Crowell *et al.*, Nucl. Instr. Meth. **A 355**(1995)575.

[Cro94] B. Crowell *et al.*, Phy. Lett **B 333** (1994)320.

[Cro95] B. Crowell *et al.*, Phys. Rev. **C 51**(1995)R1599.

[Cur88] P. Curutchet *et al.*, Phys. Lett. **B 208**, (1988)331.

[Czo91] T. Czosnyka *et al.*, *GOSIA Users Manual*, UR-NSRL (1991)305.

[Dag94] P.J. Dagnall *et al.*, Phys. Lett. **B 335** (1994)313.

[Dag95] P.J. Dagnall *et al.*, Phys. Lett. **B 533** (1995)313

[Dri90] M.W. Drigert *et al.*, Nuc. Phys. **A 515**(1990) 466.

[Dri91] M.W. Drigert *et al.*, Nuc. Phys. **A 530**(1991) 452.

[Dud87] J. Dudek, *Superdeformed Nuclear Shapes: New Features, Systematics and Predictions*, CRN preprint, Strasbourg, 1987.

[Dud85] J. Dudek and W. Nazarewicz, Phys. Rev. **C 31**(1985)298.

[Dud90] J. Dudek *et al.*, Phys. Lett. **B 248** (1990)235.

[Fah96] C. Fahlander *et al.*, Phys. Lett. **B 388**, (1996)475.

[Fal94] P. Fallon *et al.*, Phys. Rev. Lett. **73**(1994)782.

[Fee77] S.J. Feenstra *et al.*, Phys. Lett. **B 69**(1977)403.

[Fis96] S.M. Fischer *et al.*, Phys. Rev. **C 53**, (1996)2126.

[Gal94] B. Gall *et al.*, Nucl. Phys. **A 348**(1994)183.

[Gar97] P.E. Garrett *et al.*, Phys. Lett. **B 400**, (1997)250.

[Gat90] R.A. Gatenby *et al.*, Phys. Rev. **C 41**, (1990)R414.

[Gir94] M. Girod *et al.*, Phys. Lett. **B 325**, (1994)1.

[Hac95] G. Hackman, J.C. Waddiington, Nucl. Instr. Meth. **A 357**(1995)559.

[Hac97] G. Hackman *et al.*, Phys. Rev. Lett. **79** (1997)4100.

[Hag68] R.S. Hager and E.C. Seltzer, Nucl. Data **A 4**(1968)122.

[Ham74] I. Hamamoto, Phys. Rep. **63**, (1974)63.

[Hau96] K. Hauschild *et al.*, *Proc. Int. Conf. on Nuclear Structure at the Limits*, Argonne(1996).

[Hax49] O. Haxel, J.H.D. Jensen and H.E. Seuss, Phys. Rev. **75**(1949)1766.

[Hee96] P. Heenen *et al.*, submitted to Rapid Communication, Phys. Rev. C.

[Jan91] R.V.F. Janssens and T.L. Khoo, Annu. Rev. Nucl. Part. Sci. **41**(1991)301.

[Joy93] M.J. Joyce, J.F. Sharpey-Schafer *et al.*, Phys. Rev. Lett. **71**(1993)2176.

[Kho96] T.L. Khoo, M.P. Carpenter *et al.*, Phys. Lett. Rev. **76**(1996)1583.

[Kle82] P. Kleinheinz *et al.*, Phy. Rev. Lett. **48**, (1982)1457.

[Kri92] S. Krieger *et al.*, Nucl. Phys. **A 542**, (1992)43.

[Kue92] J.A. Kuehner, J.C. Waddington and D.P. Heenen *et al.*, *Proceeding of Int. Conf. on Nuclear Structure at High Angular Momentum*, AECL-10613, Ottawa(1992)413.

[Lan77] S. Landowne *et al.*, Phys. Lett. **B 70**, (1977)292

[Leo87] W.R. Leo, *Techniques for Nuclear and Particle Physics Experiments*, Springer-Verlag, Berlin(1987).

[Lop96] A. Lopez-Martens, F. Hannachi, A. Korichi *et al.*, *Proceedings of Int. Conf. on Nuclear Structure at the Limits*, Argonne(1996).

[Lun84] S. Lunardi *et al.*, Phy. Rev. Lett **53**, (1984) 1531.

[Mar83] M. Mariscotti *et al.*, Nucl. Phy. **A 407**, (1983)98.

[Mar87] M. J. Martin, Nucl. Data Sheets **47**, (1987)797.

[May49] M.G. Mayer, Phys. Rev. **75**(1949)1969.

[Mey95] J. Meyer *et al.*, Nuc. Phys. **A 588**, (1995)597.

[Mey92] J. Meyer *et al.*, Phys. Rev. **C 45**, (1992)233.

[May55] M. G. Mayer and J. H. D. Jensen,*Elementary Theory of Nuclear Shell Structure*, Wiley, New York, 1955.

[Moo89] E.F. Moore, R.V.F. Janssens *et al.*, Phys. Rev. Lett. **63**(1989)360.

[Moo90] E.F. Moore *et al.*, Phys. Rev. Lett. **64**(1990)3127.

[Moo97] E.F. Moore *et al.*, Phys. Rev. **C 55**(1997)R2150.

[Moo95] E.F. Moore, D. Nisius, R.V.F. Janssens *et al.*, *Proceedings of the Gammasphere Dedication*, Berkeley(1995).

[Nak95] T. Nakatsukasa, *Proceedings of XXIV Mazurian Lakes School of Physics*, Piaski (1995).

[Nak96] T. Nakatsukasa *et al.* Phys. Lett. **B 343**(1996)19.

[Naz87] W. Nazarewicz, G.A. Leander and J. Dudek, Nucl. Phys. **A 467**(1987)437.

[Naz89] W. Nazarewicz, R. Wyss and A. Johnson, Nuc. Phys. **A 503**(1989)285.

[Naz90] W. Nazarewicz, P.J. Twin, P. Fallon and J.D. Garrett, Phys. Rev. Lett. **64**(1990)1654.

[Naz92] W. Nazarewicz *et al.*, Phys. Rev. Lett. **68**(1992)154.

[New78] J.O. Newton, S.H. Sie and G.D. Dracoulis, Nucl. Phys. **A 210**(1978)19.

[Nis96] D. Nisius, *The Many Facts of Superdeformation In Dysprosium Isotopes: Multi-Band Structures, Shape-Driving Orbitals and Identical Bands*, Purdue University, 1996.

[Nis95] D. Nisius, R.V.F. Janssens *et al.*, Phys. Lett. **B 346**(1995)15.

[Nis97] D. Nisius *et al.*, Phy. Lett **B 392** (1997)18.

[Nor70] L.C. Northcliffe and R.F. Schilling, Nucl. Data Tables **7**(1970)256.

[Pal85] G. Palameta *et al.*, Nucl. Instr. Meth. **A 234**(1985)476.

[Pii93] M. Piiparinen *et al.*, Z. Physik A-Atomic Nuclei **337**, (1990)387.

[Pol62] S.M. Polikanov, V.A. Druiin, V. A. Karnoukhov, V.L. Mikheev, A.A. Pleve, N.K. Skobelev, V.G. Subotin, G.M. Ter-Akopjan and V.A. Formichev, Sov. Phys. JETP **15**(1962)1016.

[Pon99] V. Ponomarev *et al.*, Phy. Rev. Lett **82**, (1999)501.

[Rad92] D.C. Radford, *Notes on the use of Gelift*, Chalk River National Laboratories, Canada

[Rad92] D.C. Radford, *Proceedings of Int. Conf. on Nuclear Structure at High Angular Momentum*, AECL-10613, Ottawa(1992)403.

[Rad87] D.C. Radford *et al.*, Nucl. Instr. Meth. **A 258**, (1987)111.

[RAG86] I. Ragnarsson and S. Aberg, Phys. Lett. **B 180**(1986)191.

[Rho80] M.J. Rhoades-Brown *et al.*, Phys. Rev. **C 21**, (1980)2417.

[Ril90] M. A. Riley *et al.*, Nucl. Phys. **A 512** (1990)178

[Sch92] M. Schramm *et al.*, Z. Phys. **A 341**, (1992)137.

[Sch93] M. Schramm *et al.*, Z. Phys. **A 344**, (1993)363.

[Sch97] M. Schramm *et al.*, Phys. Rev. **C 56**, (1997)1320.

[Ska93] J. Skalski *et al.*, Nucl. Phys. **A 612**, (1993)221

[Sat91] W. Satula *et al.*, Nucl. Phys. **A 529**, (1991)289.

[Sem92] P.B. Semmes *et al.*, Phys. Lett. **B 68**, (1992)460.

[Sie77] S.H. Sie, D. Ward, J.S. Geiger, R.L. Graham and H.R. Andrews, Nucl. Phys. A 291(1977)443.

[Sim98] M.W. Simon *et al.*, *Spectroscopy of Neutron Rich Nuclui sing a Charged Heavy Ion Detector (CHICO) plus Gammasphere, Proceedings of The International Conference on Fission and Properties of Neutron Rich Nuclei* , World Scientific Publishing (1998)

[Sol92] V. G. Soloviev ,*Theory of Atomic nuclei: Quasi particles and phonons*, (Institute of Physics, Bristol,1992)

[Spe83] R.H. Spear *et al.*, Phy. Lett. **B 128**, (1983)29.

[Str67] V.M. Strutinsky, Nucl. Phys. **A 95**(1967)420.

[Twi86] P.J. Twin, B.M. Nyako *et al.*, Phys. Rev Lett. **57**(1986)811.

[Vet98] K. Vetter *et al.*, Phy. Rev. **C 58**, (1998)2631.

[Wil96] A.N. Wilson *et al.*, Phys. Rev. **C 54**(1996)559.

[Wil94] P. Willsau *et al.*, Nucl. Phys. **A 574**(1994)560.

[Win68] K.B. Winterbon Atomic Energy of Canada Limited Report, AECL-3914(1968).

[Wol92] H.A. Wollersheim *et al.*, Z. Phys **A 341**, (1992)173.

[Yeh96] M. Yeh *et al.*, Phy. Rev. Lett. **76**, (1986)1208.

[Yeh98] M. Yeh *et al.*, Phy. Rev. **C 57**, (1998)2058.

[Zie85] J.F. Ziegler. J.P. Biersack and U. Littmark, *The Stopping Power and Range of Ions in Solids*, Pergamon Press, New York(1985).